



Technische Universität München
Fakultät für Chemie
Lehrstuhl für Technische Chemie II



**Bifunctional catalysis of metal and Brønsted acid sites for
hydrodeoxygenation of triglycerides and
dehydrogenation of light alkanes**

Moritz Wilhelm Schreiber

Vollständiger Abdruck der von der Fakultät für Chemie der Technischen Universität
München zur Erlangung des akademischen Grades eines

Doktors der Naturwissenschaften (Dr. rer. nat.)

genehmigten Dissertation.

Vorsitzender: Prof. Dr. Kai-Olaf Martin Hinrichsen
Prüfer der Dissertation: 1. Prof. Dr. Johannes August Lercher
2. Prof. Dr. Thomas Brück

Die Dissertation wurde am 14.12.2017 bei der Technischen Universität München
eingereicht und durch die Fakultät für Chemie am 19.07.2018 angenommen.

The fuel of the future is going to come from fruit, weeds, sawdust - almost anything. There's enough alcohol in a one year's yield of an acre of potatoes to drive the machinery necessary to cultivate the field for a hundred years.

Henry Ford (1925)

Wir können die Theorien an unserer Stelle sterben lassen. Wir können sie eliminieren, ohne jemanden zu verletzen, es sei denn in seinen Stolz.

Karl R. Popper (1982)

Acknowledgements

I thank Prof. Dr. Johannes A. Lercher for personal, philosophical and scientific guidance throughout the years. Providing freedom whenever possible, offering guidance in crucial moments and inspiring ambitious aims created a stimulating environment requiring me to develop my skills and the project to the best extend possible.

I thank the senior scientists with whom I could develop successful projects during my dissertation: Prof. Dr. Andreas Jentys, Dr. Eszter Baráth, Dr Ricardo Bermejo-Deval and Dr. Oliver Y. Gutiérrez-Tinoco. I am looking forward to continuing trust- and fruitful exchanges.

Discussing my work with experienced external scientists opened new perspectives resulting in a more comprehensive understanding: Prof. Dr. Mirek Derewinsky, Prof. Dr. Roel Prins, Prof. Dr. Harry Bitter and Dr. Gerhardt Pirngruber, whom I could meet again at the ICC 2016 in Beijing. I especially enjoyed and learned from the discussions developing over the time with Prof. Dr. Gary Haller.

Within the Algenflugkraft project, I would like to especially thank Prof. Dr. Thomas Brück (Professur Industrielle Biokatalyse) for excellent lead and organization of the project, his coworkers Dr. Daniel Garbe for smooth cooperation in setting up the project and Johannes Schmidt for scientific exchange. Furthermore, I want to thank all other coworkers in the Algenflugkraft project (LaBay74) and the funding agencies for fruitful discussions and successful cooperation.

I am grateful to all the staff members of TCII for technical and organizational support allowing the scientific staff to focus on research: Steffi Seibold, Ulrike Sanwald, Bettina Federmann, Martin Neukamm, Andreas Marx and Franz-Xaver Hecht.

I want to thank my students for their contributions over the last years, especially Daniella Rodriguez-Niño, Manuel Weber-Stockbauer and Martin Baumgärtl for our significant scientific collaborations. I am pleased that the latter two were not scared away but integrated as Ph.D. students into TCII.

I want to thank all my colleagues and friends at TCII for the excellent cooperation and atmosphere in our lab, especially Bo Peng, Edith Ball, Elisabeth Hanrieder, Felix Kirchberger, Francisco Gonzales-Peña, Guoju Yang, Jennifer Hein, Jeongnam Kim,

Kai Sanwald, Linus Schulz, Matthias Steib, Monica Markovits, Navneet Gupta, Peter Hintermeier, Sebastian Eckstein, Sebastian Foraita, Sonja Wyrzgol, Tobias Berto, Wanqiu Luo, Wenji Song, Yang Song, Yang Zhang, Yuanshuai Liu, Yu Luo.

Stanislav Kasakov, Marco Peroni, Takaaki Ikuno, Ricardo Bermejo-Deval, Gabriella Mancino, Leonie Kertess and Christian Görner brought life to work allowing to push the work-life balance to otherwise unstable conditions – let's keep it up.

I want to thank my parents, Aline and Hans-Christian for unconditionally supporting and encouraging me in finding and choosing my own way, always.

I am very happy that my next steps bring me closer to Charlotte, who had to endure the sum of a Master's Thesis and a Ph.D. thesis of me at TCII – I am looking forward to our future!

Abstract

Cooperation of metals and Brønsted acid sites for hydrodeoxygenation of triglycerides and dehydrogenation of light alkanes was studied. In C-O hydrogenolysis on Ni/H-ZSM-5, Brønsted acid sites are interacting with the carbonyl groups of the substrate, weakening the bond to cleave, thus, enhancing turnover frequencies over Ni. In light alkane dehydrogenation on Ga/H-ZSM-5, Ga⁺ and Brønsted acid sites act as highly active Lewis-Brønsted acid pairs, on which the C-H bond is heterolytically activated in a bifunctional mechanism. The synergy enhances the rate 300-fold.

Kurzzusammenfassung

Die Kooperation von Metall- und Brønsted-Säurezentren für die Hydrodeoxygenierung von Triglyceriden und die Dehydrierung von leichten Alkanen wurde untersucht. Die Spaltung der CO-Bindungen der funktionalisierten Moleküle an der Metalloberfläche wird durch gleichzeitige Wechselwirkung mit Brønsted-sauren OH Gruppen erleichtert, was zu höheren Reaktionsraten führt. Bei der Dehydrierung der leichten Alkane auf Ga/H-ZSM-5 agieren Ga^+ und Brønsted-Säurezentren als hoch aktive Lewis-Brønsted-Säurepaare, die die C-H Bindung heterolytisch über einen bifunktionellen Mechanismus aktivieren und die Reaktionsraten gegenüber Katalyse durch ein Zentrum auf das dreihundertfache erhöhen.

Table of contents

1.	Introduction	1
1.1	Catalytic conversion of microalgae oil to kerosene	1
1.2	Algenflugkraft project	2
1.3	Zeolites	3
1.3.1	Composition and structure	3
1.3.2	Hierarchical structures	4
1.3.3	Active sites in pure and Ga modified zeolites	5
1.4	Bifunctional catalysis	7
1.5	Dehydrogenation and cracking of light alkanes	7
1.5.1	Thermodynamics of light alkane dehydrogenation and cracking	7
1.5.2	Dehydrogenation and cracking of light alkanes over Ga modified zeolites	8
1.6	Deoxygenation of triglycerides	13
1.6.1	Thermodynamics of deoxygenation of triglycerides	13
1.6.2	Deoxygenation of triglycerides over supported Ni catalysts	13
1.7	Scope of the thesis	16
1.8	References	18
2	Hydrodeoxygenation of fatty acid esters catalyzed by Ni on nano-sized MFI type zeolites	22
2.1	Abstract	22
2.2	Introduction	23
2.3	Experimental	24
2.3.1	Synthesis of supports	24
2.3.2	Synthesis of Ni catalysts	25
2.3.3	Chemical and physicochemical characterization	26
2.3.4	Activity tests	27
2.4	Results and discussion	28

2.4.1	Characterization.....	28
2.4.2	Characterization of the catalysts.....	28
2.4.3	Catalytic activity and selectivity.....	32
2.4.4	Hydrodeoxygenation of methyl stearate.....	32
2.4.5	Hydrodeoxygenation of tristearate and microalgae oil.....	36
2.4.6	On the effects of mesoporosity and composition of the support on the hydrodeoxygenation reactions.....	37
2.5	Conclusions.....	41
2.6	Acknowledgements.....	41
2.7	References.....	43
2.8	Associated Content.....	45
2.8.1	Additional Information.....	45
2.8.2	Peer-Reviewed Publication.....	45
2.8.3	Clearance by the Publisher and Coauthors.....	45
2.8.4	Notes and Author Contributions.....	45
3	Ni-catalyzed C-O hydrogenolysis enhanced by cooperation with Brønsted acid sites on Ni/H-ZSM-5.....	47
3.1	Abstract.....	47
3.2	Introduction.....	48
3.3	Experimental section.....	48
3.3.1	Chemicals.....	48
3.3.2	Catalyst preparation.....	49
3.3.3	Catalyst characterization.....	50
3.3.4	Catalytic reactions.....	52
3.4	Results and discussion.....	53
3.4.1	Catalyst characterization.....	53
3.4.2	Reaction kinetics.....	55
3.5	Conclusion.....	65

3.6	Acknowledgements	65
3.7	Literature	66
3.8	Associated Content	68
3.8.1	Additional Information	68
3.8.2	Notes and Author Contributions	68
4	Lewis-Brønsted acid pairs in Ga/H-ZSM-5 to catalyze dehydrogenation of light alkanes	70
4.1	Abstract	70
4.2	Introduction.....	71
4.3	Experimental	72
4.3.1	Synthesis	72
4.3.2	Catalytic experiments.....	72
4.3.3	Characterization.....	74
4.4	Results and discussion.....	76
4.4.1	Influence of the Ga concentration on the reaction kinetics.....	76
4.4.2	Nature and concentration of active sites	79
4.4.3	Mechanism of propane dehydrogenation on Lewis-Brønsted acid pairs.....	82
4.4.4	DFT calculations	85
4.5	Conclusion.....	95
4.6	Acknowledgement	96
4.7	Literature	98
4.8	Associated Content	100
4.8.1	Additional Information	100
4.8.2	Notes and Author Contributions	100
	Conclusion.....	102
5	Supplementary information	105
5.1	Hydrodeoxygenation of fatty acid esters catalyzed by Ni on nano-sized MFI type zeolites	105

5.2	Ni-catalyzed C-O hydrogenolysis enhanced by the Brønsted acid sites of Ni/H-ZSM-5	113
5.2.1	Characterization.....	113
5.2.2	Reaction kinetics.....	122
5.3	Lewis Brønsted acid pairs in Ga/H-ZSM-5 for the dehydrogenation of light alkanes.....	126
6	List of publications.....	135
6.1	Publications in peer-reviewed journals	135
6.2	Oral presentations	135
6.3	Poster presentations.....	136

1. Introduction

1.1 Catalytic conversion of microalgae oil to kerosene

The search for sustainable energy sources replacing fossil fuels is one of the main challenges of our modern society¹. The transportation sector accounted for 28% of global final energy consumption in 2014 of which fossil fuels represented 91%². Especially the aviation sector, with a current growth rate of 5% per year, relies on an energy carrier with high energy density, providing simple storage as well as easy and fast fueling/handling. Hydrocarbon fuel is currently the only energy carrier satisfying all these requirements compared to other energy carriers (e.g. Battery, Hydrogen). In the context of the global intent to reduce CO₂ emissions¹, sustainable hydrocarbon fuels attract increasing interest³. To allow for an economically viable substitution of fossil by sustainable sources, it is desirable that the substituting fuel is a drop-in fuel, thus readily usable in existing combustion engines, fueling/storage infrastructure and the fuel distribution network. Such drop-in fuels can be obtained readily from e.g. microorganisms *via* fermentation with subsequent hydrogenation (e.g. farnesane), from cellulosic biomass *via* thermochemical pathways (e.g. gasification with subsequent Fischer-Tropsch process) and *via* phototrophic pathways from microalgae with subsequent catalytic deoxygenation. In this context, microalgae can be manipulated in order to accumulate oil (triglycerides), a natural molecule for energy storage. Fuel derived from microalgae is considered to be a third-generation biofuel – due to the high growth rates and oil contents of microalgae as well as being non-edible and independent of fresh water and arable land⁴. In comparison to terrestrial plants, microalgae show a 10 – 100 times higher biomass yield per acreage and can archive a 30 times higher oil content on a weight basis⁴.

1.2 Algenflugkraft project

The Algenflugkraft project pursued the concept of an integrated bio-refinery, which aimed at a closed cycle of production, harvest and catalytic conversion of microalgae biomass to aviation fuels, biogas and CO₂ binding construction materials. Within the concept of catalytic conversion of the microalgae, the microalgae are opened *via* cell wall cleavage facilitated by ionic liquids to allow separation into microalgae oil and the biomass residue rich in proteins and oxygenates. The microalgae oil (mainly triglycerides) is converted into diesel range alkanes and propane, originating from the glycerol backbone of the triglycerides, *via* hydrodeoxygenation over supported Ni catalysts. The obtained diesel range alkanes are hydrocracked into kerosene range alkanes and light alkanes over Pt/HY catalysts. The light alkanes obtained in both processes are undergoing aromatization over Ga modified H-ZSM-5 catalysts. In the process scheme, the required H₂ for the hydrodeoxygenation and the hydrocracking is supplied by the aromatization process and the aqueous phase reforming of the microalgae residue. The topics examined in this thesis are the hydrodeoxygenation of triglycerides and the aromatization of light alkanes.

1.3 Zeolites

1.3.1 Composition and structure

Naturally occurring zeolites are microporous aluminosilicates with tectosilicate (three-dimensional) frameworks with a $(\text{Si} + \text{Al})/\text{O}$ ratio of $1/2^5$. The development of synthetic zeolites allowed to obtain framework structures not naturally occurring and to substitute Si and Al by other elements (e.g. Fe, B, Ga, Ge)⁵. Zeolites are generally constituted by corner connected TO_4 tetrahedrons (Basic building units = BBU), where T is typically Si or Al⁶. The connection of two Al tetrahedrons *via* a common O is unstable and thus not observed, known as the Löwenstein rule. Therefore, the highest substitution of Si^{4+} by Al^{3+} is limited to Si/Al ratios of one and higher. The tetrahedrons are connected to form composite building units (CBU, e.g. rings, single chains or polyhedral building units), responsible for the topology of the zeolite⁶. Combinations of CBUs allow to constitute a large variety of different zeolite framework types, which are described by a three letter code (e.g. MFI)⁶. The building blocks of the MFI framework are displayed exemplary in Figure 1.

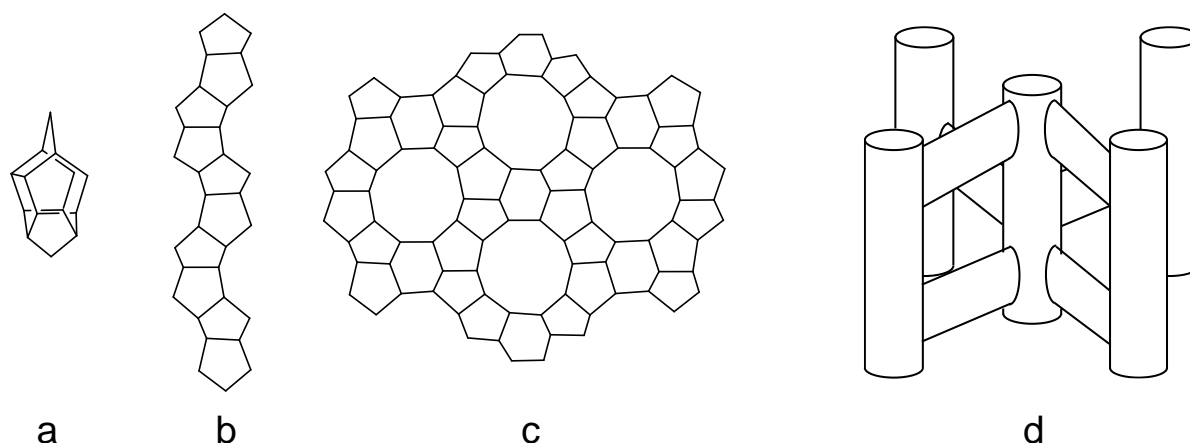


Figure 1. Building blocks of the MFI framework: Pentasil unit (a), chain of pentasil units (b), layer composed of pentasil units (c), Zigzag pore structure.

Dependent on the CBUs constituting the framework, the material can have different topologies (channels, cavities, cages) allowing diffusion of guest species in different dimensions (0, 1-, 2- or 3-dimensions)⁶. The effective width of channels, cavities and cages describes the accessibility of the pore system to guest species. Channels and cavities are typically constituted by 8-, 10-, and 12-membered rings (referring to the

quantity of tetrahedrons forming the ring). According to their ring size, zeolites are classified as small, medium and large pore zeolites, respectively. The associated geometrical constraint in zeolite pores is a keystone to the industrial use of zeolites. Reaction rates and selectivities can be influenced taking advantage of entropic constraints on transition states as well as limited diffusion of reactants or products in the channels and cavities. Frameworks, pore dimensionality, pore size classification as well as ring and pore sizes of industrially important zeolites are listed in Table 1.

Table 1. Framework code, pore dimensionality, pore size classification as well as ring and pore size⁷

Framework	Pore dimensionality	Pore size classification	Ring size	Pore size [Å]
MOR	1 dimensional	Large-pore	12-ring	6.5 × 7.0
			8-ring	2.6 × 5.7
FER	2-dimensional	Medium-pore	10-ring	4.2 × 5.4
			8-ring	3.5 × 4.8
LTA	3-dimensional	Small-pore	8-ring	4.1 × 4.1
CHA	3-dimensional	Small-pore	8-ring	3.8 × 3.8
MFI	3-dimensional	Medium-pore	10-ring	5.1 × 5.5
			10-ring	5.3 × 5.6
BEA	3-dimensional	Large-pore	12-ring	6.6 × 6.7
			12-ring	5.6 × 5.6
FAU	3-dimensional	Large-pore	12-ring	7.4 × 7.4

1.3.2 Hierarchical structures

In order to improve accessibility and molecular transport in zeolites, while maintaining the well-defined micropore structure and acid properties, a second poresystem (mesoporous or macroporous) can be implemented into the structure. Such materials with multiple levels of porosity are called hierarchical zeolites. If micropore diffusion-

limitations exist and therefore the effectiveness of a given catalysts or adsorbent is reduced, the introduction of a hierarchical pore system can effectively enhance the reaction rate, bypassing the diffusion limitations in the micropores by allowing parallel diffusion pathways in meso- or macropores⁸. In general, the introduction of a secondary pore system with different hierarchy can be archived via two different synthetic approaches: In the bottom-up method a secondary pore system is introduced during the synthesis of the material while the top-down approach relies on modifying the microporous material in a post treatment⁸. While introducing well defined pores in the materials, industrial application of bottom-up methods is limited by high cost of organic templates or processes (centrifugal filtration or multiple calcinations of material)⁸. In contrast to that, top-down methods are less expensive and more robust, therefore being more suitable for industrial application, although the introduction of additional pores is less selective and defined⁸. An example of a bottom-up method, used in this work, is the replacement of the structure directing agent in the synthesis of the material, which results in the formation of self-pillared zeolite nanosheets with mesopores of defined diameter between the nanosheets⁹. Examples of top-down methods are the post-treatment of zeolites with NaOH solution leading to desilication of the material or the industrially relevant steaming of zeolites resulting in dealumination⁸.

1.3.3 Active sites in pure and Ga modified zeolites

Isomorphous substitution of Si(IV)O_4 by Al(III)O_4 tetrahedra results in a negative charge on the trivalent Al. This negative charge is balanced by a monovalent cation (e.g. H^+ , NH_4^+ or metal ion). If the balancing species is H^+ , a Brønsted acid site is formed (BAS, Figure 2 a). Si^{4+} only coordinated by three O, as well as charge balancing metal cations act as Lewis acid sites (LAS, Figure 2 b and c, respectively). LAS and BAS in a material can differ in density (extensive property) and in strength (intensive property). The strength of Brønsted acid sites varies based on the type of the trivalent isomorphous substituent (e.g. $\text{Al} > \text{Ga}$ in H-ZSM-5¹⁰) and its concentration (for low Si/Al ratios BAS strength decreases). The influence of pore geometry is still under debate¹¹.

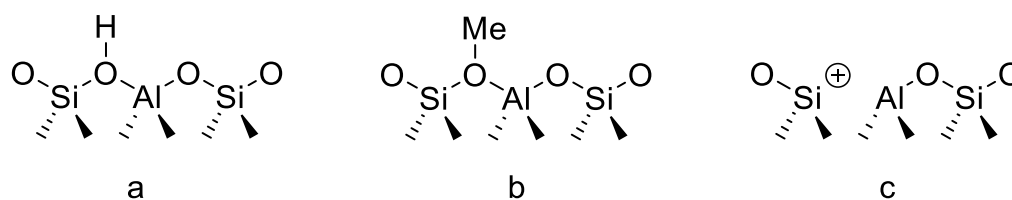


Figure 2. Graphical representation of Brønsted acid sites (a), Lewis acid sites related to metal cations (b) and related to coordinatively unsaturated Si (c)

Under reductive atmosphere and at high temperature, monovalent cationic Ga species can be exchanged with the protons of the Brønsted acid sites in the zeolite¹²⁻¹³. However, their characterization is challenging, as the reduced species readily oxidize in contact with water (e.g. in ambient air)¹³. Ga^+ , $[\text{GaH}_2]^+$, $[\text{GaO}]^+$ and $[\text{HGaOH}]^+$ have been proposed to be the exchanged species on Ga modified H-ZSM-5 materials¹²⁻¹⁷. Kwack et al. assumed the formation of initially $[\text{GaO}]^+$ and of Ga^+ under more severe reducing conditions based on two signals at around 450 °C and 630 °C during TPD of $\text{Ga}_2\text{O}_3/\text{H-ZSM-5}$ ¹⁴. Price et al. detected a weight loss corresponding to two water molecules per Ga_2O_3 in microbalance experiments on similar catalysts, therefore assuming the formation of Ga^+ ¹². Iglesia et al. observed a XANES Ga K-edge energy shift to lower energies under reducing conditions at high temperature, while the edge energy shifted to higher energies cooling down in H_2 . They interpreted this behavior as $[\text{HGaOH}]^+$ and $[\text{GaO}]^+$ being in equilibrium, with the equilibrium being on the side of $[\text{HGaOH}]^+$ at high and of $[\text{GaO}]^+$ at low temperatures. Hock et al. observed similar XANES Ga K-edge energy shifts on Ga modified zeolites¹⁷. By comparing them to Ga K-edge energies of organometallic Ga complexes with Ga being coordinated to up to four ligands *via* alkyl or ether bridges, they concluded, that the formation of $[\text{HGaOH}]^+$ or $[\text{GaO}]^+$ under reducing conditions at high temperatures can be excluded, while energy shifts previously attributed to a Ga^+ could also originate from $[\text{GaH}_2]^+$. These contradicting results evidence the still open debate and the requirement to combine different characterization methods to clarify the nature of the Ga species in Ga modified zeolites.

1.4 Bifunctional catalysis

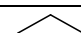
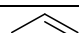
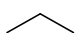

Bifunctional or cooperative catalysis describes a catalytic conversion by two functional groups, in which both functions are implicated in the rate-determining step, hence resulting in a higher reaction rate constant compared to the additive contributions of the two isolated groups (e.g. hydrogen activation over frustrated Lewis acid base pairs¹⁸)¹⁹. It is important to distinguish this from concerted catalysis, in which the different functions may catalyze separate steps in a sequence of reactions (e.g. (de-)hydrogenation function and Brønsted acid site in hydrocracking)¹⁹. The relevant state of the science for dehydrogenation and cracking of light alkanes and the deoxygenation of triglycerides is presented in the following chapters.

1.5 Dehydrogenation and cracking of light alkanes

1.5.1 Thermodynamics of light alkane dehydrogenation and cracking

Dehydrogenation and cracking of alkanes are endothermic reactions with a positive change of entropy (Table 2). In order to allow for reasonably high equilibrium conversions, dehydrogenation requires higher reaction temperatures compared to cracking (Figure 3). Hence, industrial dehydrogenation processes are carried out at higher temperatures compared to catalytic cracking processes (Fluid catalytic cracking 500 - 565 °C²⁰, Catalytic dehydrogenation 525 to 705 °C²¹). With increasing carbon chain length, the reaction enthalpy of both reactions is decreasing, therefore more energy is required for conversion of shorter alkanes on a mass basis. Lower partial pressures shift the equilibrium conversion to the side of the products for both reactions, as during reaction two molecules are formed out of one.

Table 2. Standard enthalpy and entropy of reaction for propane dehydrogenation and cracking.

Reaction		$\Delta_r H^\circ_{\text{gas}}$ [kJ·mol ⁻¹]	$\Delta_r S_{\text{gas}}$ [J (mol·K) ⁻¹]
Dehydrogenation	 \rightleftharpoons  + H ₂	125.1	127.8
Cracking	 \rightleftharpoons  + CH ₄	82.3	136.0

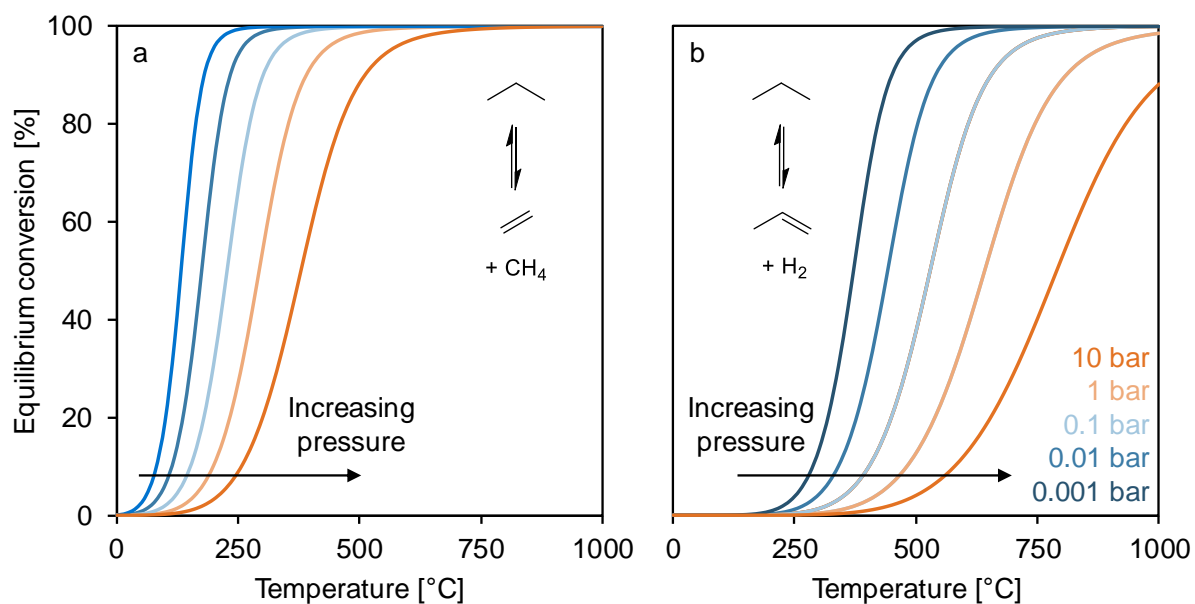


Figure 3. Equilibrium conversion of propane cracking (a) and cracking (b) as a function of temperature at a propane at different partial pressures.

1.5.2 Dehydrogenation and cracking of light alkanes over Ga modified zeolites

Dehydrogenation is catalyzed by Lewis and Brønsted acid sites, while cracking is only catalyzed by Brønsted acid sites. On Brønsted acid sites, both reactions pass through a carbonium ion in the transition state (Figure 4). C-H bonds (for dehydrogenation) or C-C bonds (for cracking) can be protonated by Brønsted acid sites forming 3-center-2-electron bonds as proposed by Haag and Dessau²² based on the work of Olah²³. This carbonium ion formation is believed to be the rate determining step of cracking, based on kinetic measurements and DFT calculations²⁴⁻²⁵. Most prominent experimental indications for this are the reaction order being unity, the presence of a kinetic isotope effect in alkane cracking for deuterated and undeuterated Brønsted acid sites and the dependency of the apparent activation enthalpy on the carbon chain length²⁴, which is going to be discussed in more detail.

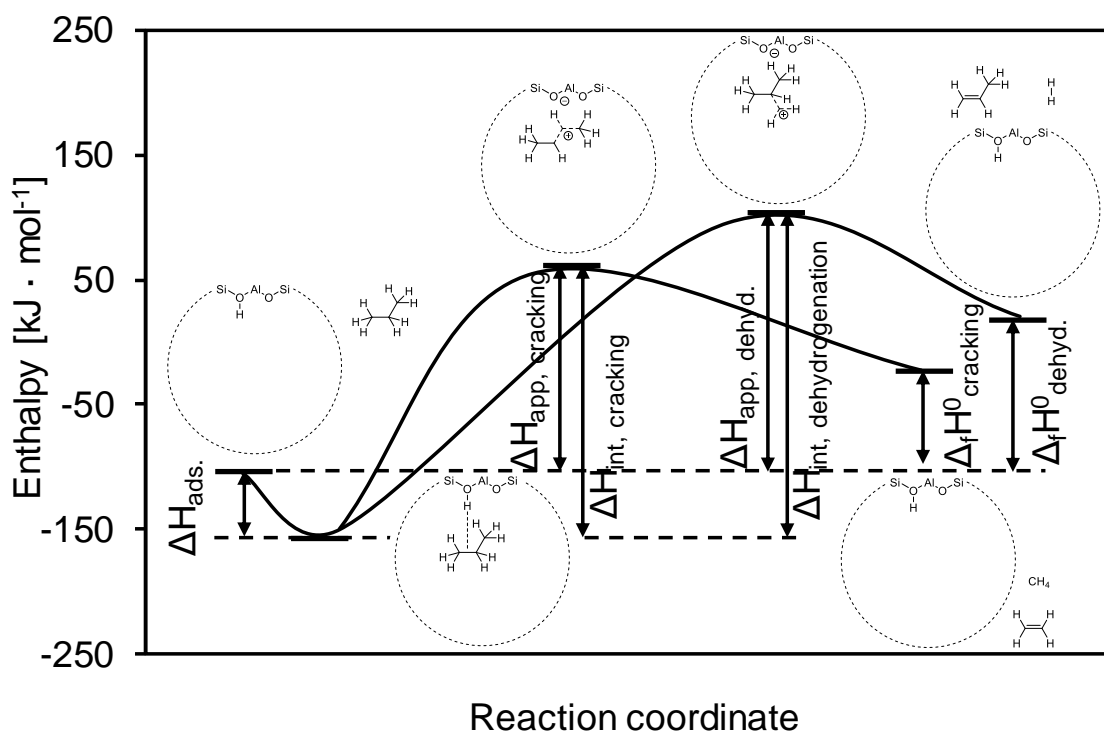


Figure 4. Enthalpy diagram for protolytic cracking and dehydrogenation based partly on ²⁴ and ²⁶.

The intrinsic enthalpy of activation was found to be independent of carbon chain length and position of the C-C bond²⁴. Prior to protonation, alkanes are adsorbed on Brønsted acid sites. Adsorption enthalpies are increasing concomitantly with carbon chain length by an amount of approximately $12 \text{ kJ} \cdot \text{mol}^{-1}$ per CH_2 segment²⁴. The energy liberated in adsorption reduces the energy needed to overcome the activation barrier for the formation of the carbonium ion. This is reflected in the decrease of apparent activation by the adsorption enthalpy of the respective hydrocarbon²⁴. This is the reason for the observed exponential increase of cracking rates of alkanes with increasing carbon chain length (Figure 5)²⁴. Even though it is believed today, that for dehydrogenation the rate-determining step is also the carbonium ion formation, based on a reaction order of unity and DFT calculations^{25, 27}, no kinetic isotope effect for alkane dehydrogenation was found over deuterated and undeuterated Brønsted acid sites²⁸. Generally, C-H bond compared to C-C bond protonation is more difficult, reflected in activation enthalpy being higher by approximately $40 \text{ kJ} \cdot \text{mol}^{-1}$ ²⁹.

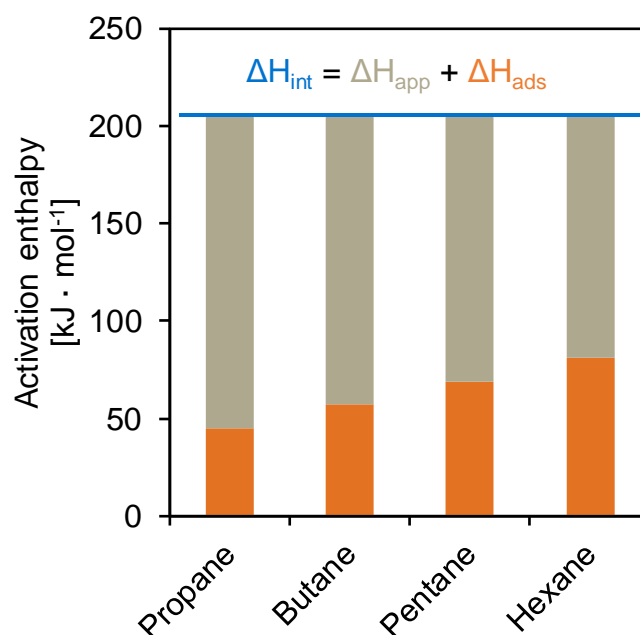


Figure 5. Graphic representation of relation of adsorption enthalpy as well as apparent and intrinsic activation enthalpy based on ²⁴ and ²⁶.

It was shown that Ga modified zeolites exhibit significantly higher dehydrogenation to the detriment of cracking rates compared to pure zeolites^{14-15, 30-31}. Synergistic interactions between Ga species and Brønsted acid sites are described, which cannot be explained by additive contributions of Ga and Brønsted acid sites only^{14-15, 30-31}. Several hypotheses were made on the nature of the interaction between Ga species and Brønsted acid sites. The proposals can be separated into two types. In the first type, dehydrogenation is taking place *via* formation of carbonium ion on Brønsted acid sites with the Ga species facilitating conversion^{15, 31}. Whereas in the second type of proposals, Ga species abstract a hydride from the alkane under formation of a carbenium ion. Here, the role of the Brønsted acid site is to present the proton for recombination with the hydride forming molecular H₂^{14, 30}. In the following, the four most important mechanistic proposals are presented.

In the mechanism proposed by Meriaudeau et al.³⁰ propane is adsorbed on Ga₂O₃ as a hydride and an alkoxy species (Figure 6). In a second step the alkoxy group exchanges with the proton of the Brønsted acid site. This allows for recombination of the hydride and the proton to molecular H₂. In the last step the alkene desorbs.

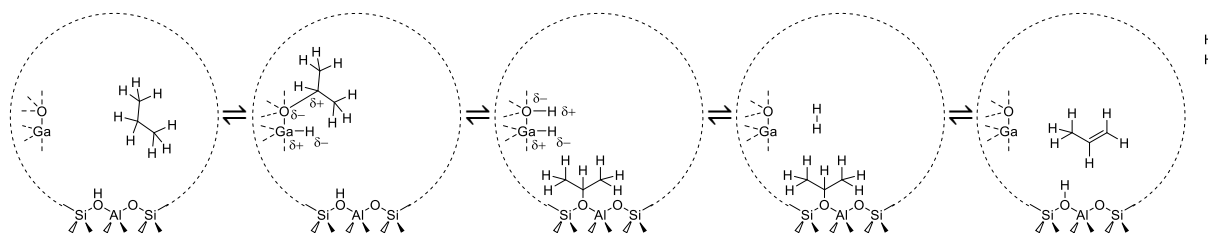


Figure 6. Reaction mechanism of propane dehydrogenation as proposed by Meriaudeau et al.³⁰

The mechanism proposed by Sachtler et al.¹⁴ (Figure 7) proceeds also with an abstraction of a hydride from the alkane, however, by Ga^+ . The stabilization of the formed carbenium ion is not explained. In a next step the hydride is directly recombining with the Brønsted acid proton. Finally, the carbenium ion is reconstituting the Brønsted acid site under formation of the olefin.

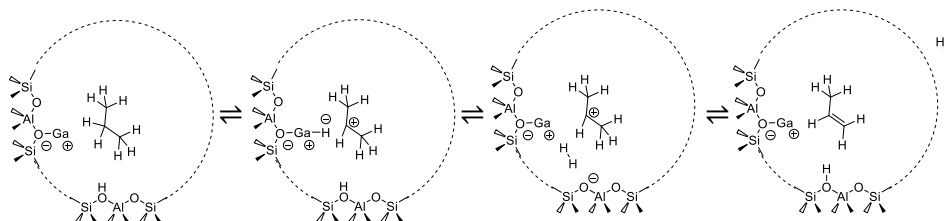


Figure 7. Reaction mechanism of propane dehydrogenation as proposed by Sachtler et al.¹⁴

Iglesia et al.¹⁵ proposed the formation of a carbonium ion on a Brønsted acid site in a first step. The role of $[\text{GaO}]^+$ being to facilitate the recombinative desorption of molecular hydrogen.

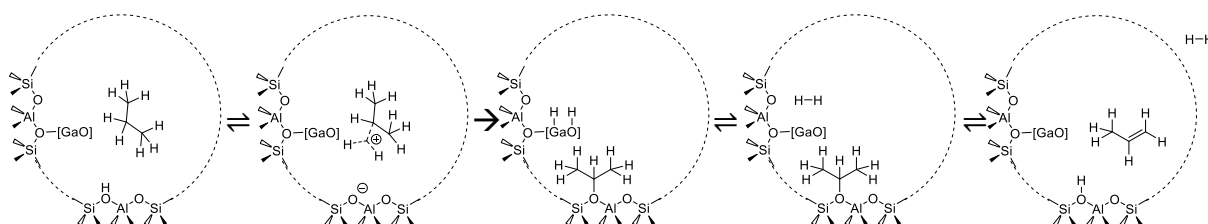


Figure 8. Reaction mechanism of propane dehydrogenation as proposed by Iglesia et al.¹⁵

Hutchings et al.³¹ proposed that the role of Ga_2O_3 would be to polarize C-H bonds, which makes protonation by a Brønsted acid sites forming a carbenium ion easier (Figure 9). Prior studies found that Lewis acid sites in zeolite channels can indeed polarize C-H bonds³²⁻³⁴.

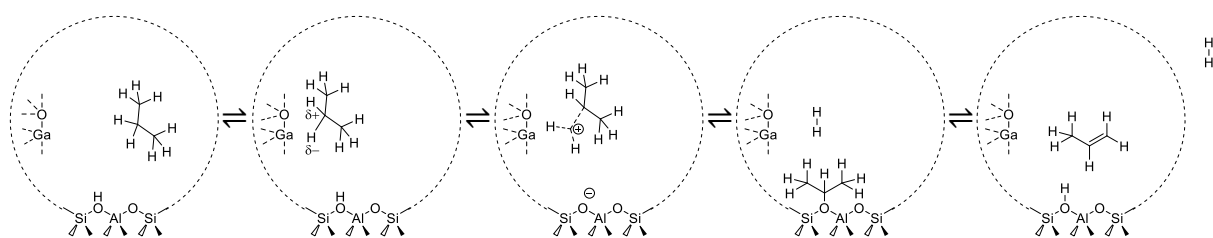


Figure 9. Reaction mechanism of propane dehydrogenation as proposed by Hutchings et al. ³¹.

The significant differences in the proposals underline the need for a comprehensive analysis of the reaction mechanism of alkane dehydrogenation over Ga species and Brønsted acid sites, in order to gain a deeper understanding on the synergistic interaction over these sites.

1.6 Deoxygenation of triglycerides

1.6.1 Thermodynamics of deoxygenation of triglycerides

Triglycerides can be converted to alkanes *via* three general pathways: Hydrodeoxygenation, decarbonylation and decarboxylation (Table 3). The H₂ consumption is decreasing in that order, with a low H₂ consumption of e.g. decarboxylation being conceptually cost and energy efficient. However, this is counterbalanced by the loss of carbon atoms of the reactant as CO or CO₂ reducing the carbon mass efficiency of the process. All pathways are exothermic and nearly complete equilibrium conversions are archived at temperatures above 473 K.

Table 3. Thermodynamics of different pathways of deoxygenation of triglycerides.

Reaction type	Equation	$\Delta_r H^\circ$ [kJ · mol ⁻¹]	$\Delta_r S$ [J · (mol · K) ⁻¹]	$\Delta_r G^\circ_{513}$ [kJ · mol ⁻¹]
Hydrodeoxygenation	$C_{57}H_{110}O_6 + 12 H_2 \rightarrow C_3H_8 + 3 C_{18}H_{38} + 6 H_2O$	-991.7	-323.5	-825.8
Decarbonylation	$C_{57}H_{110}O_6 + 6 H_2 \rightarrow C_3H_8 + 3 C_{17}H_{36} + 3 CO + 3 H_2O$	-388.2	710.7	-752.8
Decarboxylation	$C_{57}H_{110}O_6 + 3 H_2 \rightarrow C_3H_8 + 3 C_{17}H_{36} + 3 CO_2$	-379.8	941.3	-862.6

1.6.2 Deoxygenation of triglycerides over supported Ni catalysts

Different types of catalysts, e.g. reduced metals or industrial hydrotreating catalysts (sulfided transition metal catalysts like NiMo, CoMo) are active for the deoxygenation of triglycerides. However, transition metal catalysts contaminate the product stream and deactivate due to removal of sulfur from the surface *via* a reverse Mars-van Krevelen mechanism³⁵. Both noble and base metal catalysts showed to be active, however, the latter attracted significant interest, due to lower concerns on material stability and cost³⁶. Despite the thermodynamic feasibility of hydrogen free deoxygenation, sulfided transition metal catalysts are inactive in the absence of H₂, while noble and base metal catalyst are significantly less active and readily deactivate due to coke formation in a H₂-free atmosphere³⁷. Comparing Pt, Pd and Ni supported on ZrO₂, Ni showed reaction rates comparable to the noble metals for the conversion

of palmitic acid, a model compound for triglycerides³⁸. Because of its activity, stability and low costs²⁻⁶, Ni is one of the most promising metals for deoxygenation catalysts. In view of reactions pathways, decarbonylation and decarboxylation are typically catalyzed by metals, whereas hydrodeoxygenation readily proceeds if metal and Brønsted acid sites are present *via* dehydration of the alcohol intermediate (formed over the metal) over the Brønsted acid sites^{37, 39}. This makes Ni supported on zeolites a suitable catalyst choice, if deoxygenation without carbon loss is desired. The proposed reaction mechanism over bifunctional Ni supported zeolite catalysts in literature is shown in Figure 10.

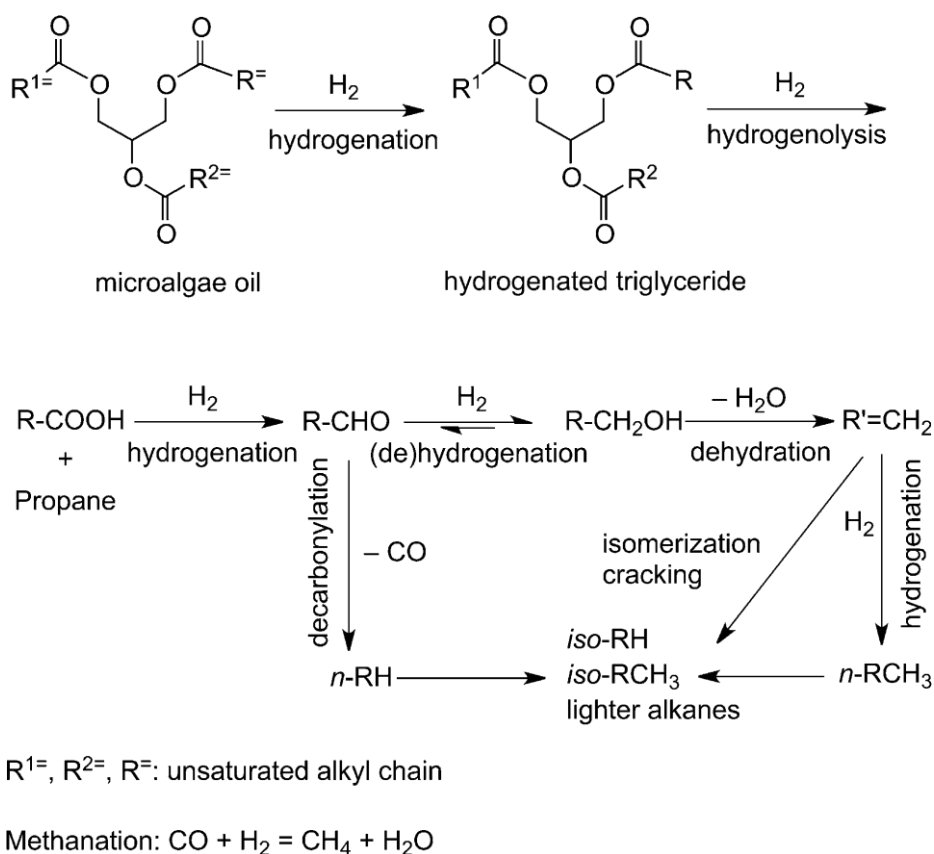


Figure 10. Proposed reaction mechanism of microalgae oil conversion over bifunctional Ni/zeolite catalysts³⁹.

While microporosity in zeolites can result in rate enhancement and shape selectivity, it can also cause pore diffusion limitations and restricted access of substrates to active sites within the micropores. This problem is more aggravating for large and bulky molecules (e.g. triglycerides). Metals supported on hierarchical zeolites, with a complementary system of meso- or macropores, may thus allow for a better accessibility to active sites and for limiting pore diffusion limitations inside the

micropores. Therefore, they have been speculated to allow for higher activities in contrast to metals supported on zeolites with conventional structure⁹.

Next to effects based on their potential pore geometry and accessibility to active sites, the support can influence the intrinsic activity of metals. This effect has been reported for noble metals for reactions like hydrogenation⁴⁰, C-C hydrogenolysis⁴¹, ring enlargement⁴², and isomerization⁴³. In contrast to that, this effect has only been recently observed for C-O hydrogenolysis over base metals, but has not been rationalized. On noble metals, several models were proposed in order to rationalize the effect of the support on metal catalyzed reactions, which are going to be tested for the case of Ni: Brønsted acid sites in vicinity to Ni particles could change certain bond strengths due to its interaction with the reactant facilitating its conversion on the Ni particle. Brønsted acid sites could increase the coverage of reactants on the catalyst surface concomitantly increasing the rates of conversion⁴⁴. Highly active sites based on the interplay of a very small Ni particle and one or more Brønsted acid sites inside the micropore channels of the zeolite could be formed, facilitating the supply of the Ni particle with hydrogen analogue to a recently proposed mechanism in homogeneous catalysis/organometallic chemistry⁴⁵. Brønsted acid sites could decrease the electron density of adjacent Ni particles resulting in different substrate-metal interactions leading to a higher intrinsic Ni activity⁴⁶. As zeolite supported Ni catalysts represent highly active hydrodeoxygenation catalysts, a better understanding of the synergetic effect between support and metal is desirable.

1.7 Scope of the thesis

Hydrodeoxygenation of triglycerides over Ni supported on MFI type zeolites and dehydrogenation of light alkanes over Ga modified H-ZSM-5 are covered within the scope of converting microalgae oil to hydrocarbons in the kerosene range.

In the first part, the hydrodeoxygenation of triglycerides and related model fatty acid alkyl esters (tristearate, methyl stearate) over Ni supported on MFI type zeolites is studied. The accessibility of triglycerides to metal sites and the diffusion of reaction intermediates within micropores of the zeolite is potentially restricted. Supports possessing a hierarchical pore system (containing micro-, meso- and macropores) have been speculated to allow a better accessibility compared to materials with conventional morphology. To explore this potential advantage, Ni supported on MFI type zeolites with well-defined conventional and hierarchical structure will be synthesized and compared in the deoxygenation of triglycerides and related model compounds (Chapter 2). Comparing aluminosilicate (H-ZSM-5) with pure silicate (Silicalite 1) MFI type supports within this study, an increase in intrinsic Ni activity for the initial C-O hydrogenolysis, the rate-determining step of fatty acid alkyl ester conversion, were observed. Such effects were reported in literature and studied intensively for supported noble metal catalysts for reactions other than C-O hydrogenolysis. As zeolite supported Ni materials are promising active, stable and cheap hydrodeoxygenation catalysts, it is envisaged to correlate the intrinsic Ni activity quantitatively with the zeolite Brønsted acidity (Chapter 3). In conjunction with this, an unprecedented study of apparent transition state enthalpy and entropy will be conducted with the aim of elucidating the origin of the enhanced intrinsic Ni activity by Brønsted acid sites.

In the second part, the dehydrogenation of light alkanes over Ga modified H-ZSM-5, being the rate-determining step of light alkane aromatization over industrial catalysts, will be studied (Chapter 4). A synergistic interaction between Lewis acidic Ga species and Brønsted acid sites is described in literature, as catalysts containing both species exhibit a high rate of propane dehydrogenation, which cannot be explained only by additive contributions of Ga and Brønsted acid sites. However, the nature and concentrations of active sites present on Ga exchanged zeolite catalysts and the mechanism of dehydrogenation are still under debate. Therefore, the nature and concentration of active sites of Ga modified H-ZSM-5 catalysts with different Ga/Al ratios

will be determined *via* IR spectroscopy of adsorbed pyridine (py-IR), *in operando* X-ray absorption spectroscopy (XAS) and pulsed temperature programmed reduction (TPD). Having established the stoichiometry and nature of active sites responsible for the synergetic interaction, the mechanism of dehydrogenation over these sites will be elucidated based on kinetic studies and DFT calculations.

1.8 References

1. *Framework Convention on Climate Change: Report of the Conference of the Parties on its twenty-first session, held in Paris from 30 November to 13 December 2015, Part one: Proceedings*; United Nations: 2016.
2. *Key world energy statistics*; International Energy Agency: Paris, 2016.
3. *Technology Roadmap - Biofuels for Transport*; International Energy Agency: Paris, France, 2011.
4. Zhao, C.; Bruck, T.; Lercher, J. A., Catalytic deoxygenation of microalgae oil to green hydrocarbons. *Green Chemistry* **2013**, *15* (7), 1720-1739.
5. Chemical Nomenclature and Formulation of Compositions of Synthetic and Natural Zeolites. In *Pure and Applied Chemistry*, 1979; Vol. 51, p 1091.
6. McCusker, L. B.; Liebau, F.; Engelhardt, G., Nomenclature of structural and compositional characteristics of ordered microporous and mesoporous materials with inorganic hosts: (IUPAC recommendations 2001). *Microporous and Mesoporous Materials* **2003**, *58* (1), 3-13.
7. Baerlocher, C.; McCusker, L. B. *Database of Zeolite Structures*.
8. Perez-Ramirez, J.; Christensen, C. H.; Egeblad, K.; Christensen, C. H.; Groen, J. C., Hierarchical zeolites: enhanced utilisation of microporous crystals in catalysis by advances in materials design. *Chemical Society Reviews* **2008**, *37* (11), 2530-2542.
9. Zhang, X.; Liu, D.; Xu, D.; Asahina, S.; Cychosz, K. A.; Agrawal, K. V.; Al Wahedi, Y.; Bhan, A.; Al Hashimi, S.; Terasaki, O.; Thommes, M.; Tsapatsis, M., Synthesis of Self-Pillared Zeolite Nanosheets by Repetitive Branching. *Science* **2012**, *336* (6089), 1684-1687.
10. Mirsojew, I.; Ernst, S.; Weitkamp, J.; Knözinger, H., Characterization of acid properties of [Al]- and [Ga]-HZSM-5 zeolites by low temperature Fourier transform infrared spectroscopy of adsorbed carbon monoxide. *Catalysis Letters* **1994**, *24* (3), 235-248.
11. Jones, A. J.; Iglesia, E., The Strength of Brønsted Acid Sites in Microporous Aluminosilicates. *ACS Catalysis* **2015**, *5* (10), 5741-5755.
12. Price, G. L.; Kanazirev, V., Ga₂O₃/HZSM-5 propane aromatization catalysts: Formation of active centers via solid-state reaction. *Journal of Catalysis* **1990**, *126* (1), 267-278.
13. Meitzner, G. D.; Iglesia, E.; Baumgartner, J. E.; Huang, E. S., The Chemical State of Gallium in Working Alkane Dehydrocyclodimerization Catalysts. In situ Gallium K-Edge X-Ray Absorption Spectroscopy. *Journal of Catalysis* **1993**, *140* (1), 209-225.
14. Kwak, B. S.; Sachtler, W. M. H., Effect of Ga/Proton Balance in Ga/HZSM-5 Catalysts on C₃ Conversion to Aromatics. *Journal of Catalysis* **1994**, *145* (2), 456-463.
15. Biscardi, J. A.; Iglesia, E., Structure and function of metal cations in light alkane reactions catalyzed by modified H-ZSM5. *Catalysis Today* **1996**, *31* (3), 207-231.
16. Gonzales, N. O.; Chakraborty, A. K.; Bell, A. T., A density functional theory study of hydrogen recombination and hydrogen-deuterium exchange on Ga/H-ZSM-5. *Topics in Catalysis* **1999**, *9* (3), 207-213.
17. Getsoian, A.; Ujjal Das, U.; Camacho-Bunquin, J.; Zhang, G.; Gallagher, J. R.; Hu, B.; Cheah, S.; Schaidle, J. A.; Ruddy, D. A.; Hensley, J. E.; Krause, T. R.; Curtiss, L. A.; Miller, J. T.; Hock, A. S., Organometallic model complexes elucidate the active gallium species in alkane dehydrogenation catalysts based on ligand effects in Ga K-edge XANES. *Catalysis Science & Technology* **2016**, *6* (16), 6339-6353.
18. Stephan, D. W.; Erker, G., Frustrated Lewis Pairs: Metal-free Hydrogen Activation and More. *Angewandte Chemie International Edition* **2010**, *49* (1), 46-76.

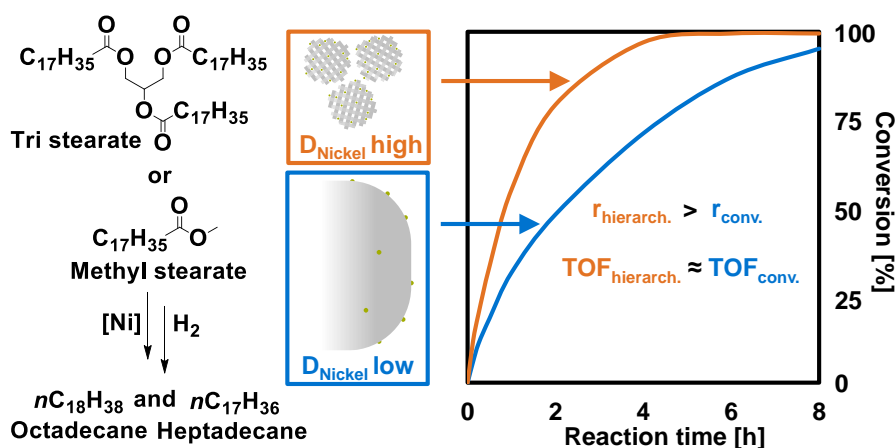
19. McNaught, A. D.; Wilkinson, A. *IUPAC. Compendium of Chemical Terminology, 2nd ed. (the "Gold Book")*; 1997.
20. Sadeghbeigi, R., *Fluid catalytic cracking Handbook*. Third edition ed.; Elsevier: 2012.
21. Sattler, J. J. H. B.; Ruiz-Martinez, J.; Santillan-Jimenez, E.; Weckhuysen, B. M., Catalytic Dehydrogenation of Light Alkanes on Metals and Metal Oxides. *Chemical Reviews* **2014**, *114* (20), 10613-10653.
22. Haag, W. O.; Dessau, R. M. In *Duality of Mechanism in Acid Catalyzed Paraffin Cracking*, Eighth International Congress on Catalysis, 1984; pp 305-315.
23. Kotrel, S.; Knözinger, H.; Gates, B. C., The Haag–Dessau mechanism of protolytic cracking of alkanes. *Microporous and Mesoporous Materials* **2000**, *35–36*, 11-20.
24. Narbeshuber, T. F.; Vinek, H.; Lercher, J. A., Monomolecular Conversion of Light Alkanes over H-ZSM-5. *Journal of Catalysis* **1995**, *157* (2), 388-395.
25. Van Speybroeck, V.; Hemelsoet, K.; Joos, L.; Waroquier, M.; Bell, R. G.; Catlow, C. R. A., Advances in theory and their application within the field of zeolite chemistry. *Chemical Society Reviews* **2015**, *44* (20), 7044-7111.
26. Gounder, R.; Iglesia, E., Catalytic Consequences of Spatial Constraints and Acid Site Location for Monomolecular Alkane Activation on Zeolites. *Journal of the American Chemical Society* **2009**, *131* (5), 1958-1971.
27. Gounder, R.; Iglesia, E., Catalytic hydrogenation of alkenes on acidic zeolites: Mechanistic connections to monomolecular alkane dehydrogenation reactions. *Journal of Catalysis* **2011**, *277* (1), 36-45.
28. Narbeshuber, T. F.; Brait, A.; Seshan, K.; Lercher, J. A., Dehydrogenation of Light Alkanes over Zeolites. *Journal of Catalysis* **1997**, *172* (1), 127-136.
29. Gounder, R.; Iglesia, E., The Roles of Entropy and Enthalpy in Stabilizing Ion-Pairs at Transition States in Zeolite Acid Catalysis. *Accounts of Chemical Research* **2012**, *45* (2), 229-238.
30. Meriaudeau, P.; Naccache, C., The role of Ga₂O₃ and proton acidity on the dehydrogenating activity of Ga₂O₃-HZSM-5 catalysts: evidence of a bifunctional mechanism. *Journal of Molecular Catalysis* **1990**, *59* (3), L31-L36.
31. Buckles, G.; Hutchings, G. J.; Williams, C. D., Aromatization of propane over Ga/H-ZSM-5: An explanation of the synergy observed between Ga³⁺ and H⁺. *Catalysis Letters* **1991**, *11* (1), 89-93.
32. Schüßler, F.; Schallmoser, S.; Shi, H.; Haller, G. L.; Ember, E.; Lercher, J. A., Enhancement of Dehydrogenation and Hydride Transfer by La³⁺ Cations in Zeolites during Acid Catalyzed Alkane Reactions. *ACS Catalysis* **2014**, *4* (6), 1743-1752.
33. Sievers, C.; Onda, A.; Olindo, R.; Lercher, J. A., Adsorption and Polarization of Branched Alkanes on H–LaX. *The Journal of Physical Chemistry C* **2007**, *111* (14), 5454-5464.
34. Kazansky, V. B.; Pidko, E. A., Intensities of IR Stretching Bands as a Criterion of Polarization and Initial Chemical Activation of Adsorbed Molecules in Acid Catalysis. Ethane Adsorption and Dehydrogenation by Zinc Ions in ZnZSM-5 Zeolite. *The Journal of Physical Chemistry B* **2005**, *109* (6), 2103-2108.
35. Laurent, E.; Delmon, B., Influence of water in the deactivation of a sulfided NiMo_y-Al₂O₃ catalyst during hydrodeoxygenation. *Journal of Catalysis* **1994**, *146* (1), 281-291.
36. De, S.; Zhang, J.; Luque, R.; Yan, N., Ni-based bimetallic heterogeneous catalysts for energy and environmental applications. *Energy & Environmental Science* **2016**, *9* (11), 3314-3347.

37. Gosselink, R. W.; Hollak, S. A. W.; Chang, S.-W.; van Haveren, J.; de Jong, K. P.; Bitter, J. H.; van Es, D. S., Reaction Pathways for the Deoxygenation of Vegetable Oils and Related Model Compounds. *ChemSusChem* **2013**, *6* (9), 1576-1594.
38. Peng, B.; Zhao, C.; Kasakov, S.; Foraita, S.; Lercher, J. A., Manipulating Catalytic Pathways: Deoxygenation of Palmitic Acid on Multifunctional Catalysts. *Chemistry – A European Journal* **2013**, *19* (15), 4732-4741.
39. Peng, B.; Yao, Y.; Zhao, C.; Lercher, J. A., Towards Quantitative Conversion of Microalgae Oil to Diesel-Range Alkanes with Bifunctional Catalysts. *Angew. Chem. Int. Ed.* **2012**, *51* (9), 2072-2075.
40. de Mallmann, A.; Barthomeuf, D., *J. Chim. Phys. Phys.-Chim. Biol.* **1990**, *87*, 535.
41. Zhang, Z.; Wong, T. T.; Sachtler, W. M. H., The effect of Ca²⁺ and Mg²⁺ ions on the formation of electron-deficient palladium-proton adducts in zeolite Y. *Journal of Catalysis* **1991**, *128* (1), 13-22.
42. Dossi, C.; Psaro, R.; Ugo, R.; Zhang, Z. C.; Sachtler, W. M. H., Non-acidic Pd/Y Zeolite Catalysts from Organopalladium Precursors: Preparation and Catalytic Activity in MCP Reforming. *Journal of Catalysis* **1994**, *149* (1), 92-99.
43. Menacherry, P. V.; Haller, G. L., Electronic effects and effects of particle morphology in n-hexane conversion over zeolite-supported platinum catalysts. *Journal of Catalysis* **1998**, *177* (2), 175-188.
44. Yu, Y.; Fonfé, B.; Jentys, A.; Haller, G. L.; Rob van Veen, J. A.; Gutiérrez, O. Y.; Lercher, J. A., Bimetallic Pt–Pd/silica–alumina hydrotreating catalysts. Part II: Structure–activity correlations in the hydrogenation of tetralin in the presence of dibenzothiophene and quinoline. *Journal of Catalysis* **2012**, *292*, 13-25.
45. Song, W.; Liu, Y.; Barath, E.; Zhao, C.; Lercher, J. A., Synergistic effects of Ni and acid sites for hydrogenation and C-O bond cleavage of substituted phenols. *Green Chemistry* **2015**, *17* (2), 1204-1218.
46. Homeyer, S. T.; Karpiński, Z.; Sachtler, W. M. H., Effect of zeolite protons on palladium-catalyzed hydrocarbon reactions. *Journal of Catalysis* **1990**, *123* (1), 60-73.

2 Hydrodeoxygenation of fatty acid esters catalyzed by Ni on nano-sized MFI type zeolites

2.1 Abstract

The impact of support morphology and composition on the intrinsic activity of Ni supported on MFI-type zeolite was explored in the hydrodeoxygenation of methyl stearate, tristearate, and algae oil (mixture of triglycerides). The nano-sized structure of the support (self-pillared nanosheets) is beneficial for the activity of the catalysts. Higher Ni dispersion and concomitant higher reaction rates were obtained on nano-structured supports than on zeolite with conventional morphology. Rates normalized to accessible Ni atoms (TOF), however, varied little with support morphology. Acidity of the support increases the rate of Ni-catalyzed C-O hydrogenolysis per surface metal site.



2.2 Introduction

The conversion of biomass derived oils and fatty acids into transportation fuels is a promising route towards synthesis of renewable energy carriers. Thus, the development of chemical technologies for the conversion of, e.g., mixtures of lipids or phenolic compounds (derived from vegetable/microalgae oils, or pyrolysis oils, respectively), into third generation biofuels has received large interest. Research efforts focus on describing the conversion of complex mixtures of oxygenates to fuel components and on the development of novel stable catalysts.

Active catalysts for the transformation of biomass-derived oils must contain metal and acid functionalities, which lead to efficient deoxygenation through sequences of hydrogenolysis, hydrogenation, and dehydration^{1, 2}. Deoxygenation of fatty acids proceeds *via* hydrodeoxygenation (HDO), whereby oxygen is removed by consecutive steps of hydrogenolysis and hydrogenation, or *via* decarboxylation/decarbonylation (DCO), which does not consume hydrogen but reduces the carbon number of the product. HDO and DCO are typically catalyzed by metals, whereas full oxygen removal readily proceeds on acid sites *via* dehydration. The DCO/HDO selectivity, which controls the tradeoff between hydrogen consumption and carbon losses, usually favors HDO over DCO for deoxygenation of fatty acids.³

Ni supported on zeolites is one of the most promising systems for deoxygenation, because of its activity, stability and versatility²⁻⁶. Metal content, particle size of the metal and the acidity of the zeolite can be adjusted using a wide variety of methods.

Whereas the microporosity of zeolites (close to the dimensions of the molecules to be converted) leads to rate enhancement and shape selectivity, it is also associated with potential diffusion limitation and restricted access of substrates to active sites. These problems are more aggravating as the size and complexity of molecules increases.

In order to mitigate the drawbacks of microporosity, while keeping the advantageous structure and well defined acid properties, the crystalline domains have been reduced to nanometric size increasing the fraction of mesopores within the zeolite crystals (hierarchical zeolites)^{7, 8}. Metals supported on such zeolites have been speculated to be more accessible than metals in the pores of conventional zeolites⁹.

To explore this potential advantage, we have prepared Ni catalysts on supports with well-defined zeolite domain sizes and pore systems. That is, MFI type zeolites (silicate

and aluminosilicate) with conventional morphology and house of cards organized nanosheets. The Ni loading was kept constant (deposited by deposition-precipitation). The influence of physicochemical properties on the catalytic activity for the deoxygenation of methyl stearate, tristearate, and microalgae oil is explored. A smaller domain size of the zeolite is indeed found to be beneficial for catalytic activity.

2.3 Experimental

2.3.1 Synthesis of supports

The aluminosilicate MFI type zeolite with a Si/Al ratio of 90 (H-ZSM-5) was synthesized by adding tetraethyl orthosilicate (130 mmol), sodium aluminate (1.44 mmol), and tetrapropylammonium hydroxide (26 mmol) to deionized water (1425 mmol). In the synthesis of silicate MFI type zeolite (Silicalite 1) sodium aluminate was not added to the solution. Aging of the mixtures took place under stirring at room temperature overnight. The aged solutions were transferred into Teflon-lined stainless-steel autoclaves and treated at 443 K for 72 h in a rotating oven with a speed of 30 rpm. After cooling, the resulting suspensions were centrifuged and washed with deionized water. The recovered solids were dried at 343 K overnight and treated in flowing synthetic air ($100 \text{ ml}\cdot\text{min}^{-1}$) at 823 K (heating rate of $2\text{K}\cdot\text{min}^{-1}$) for 8 hours. Subsequently, the powders were stirred in deionized water overnight at 343 K. For the ion exchange, the materials were suspended in 90 mL of 1 M ammonium nitrate solutions and stirred for 5 h at 343 K. The liquid was separated by centrifugation. This step was repeated three times. After drying at 343 K overnight, the materials were finally treated at 823 K (heating rate of $10 \text{ K}\cdot\text{min}^{-1}$) for 5 h under a flow of synthetic air ($100 \text{ ml}\cdot\text{min}^{-1}$).

Nano-structured self-pillared aluminosilicate zeolite nanosheets with MFI framework (n-H-ZSM-5) and the silicate counterpart (n-Silicalite 1) were prepared according to Ref.⁸. For the zeolite material synthesis (Si/Al = 90), tetraethyl orthosilicate (50 mmol) was added dropwise to a 40 vol. % solution of tetra-n-butylphosphonium hydroxide (168 mmol) while stirring. To this solution, 9.3 g distilled water and aluminium isopropoxide (1 mmol) was added. The mixture was aged for 12 hours with stirring at room temperature. The solution was transferred to a Teflon-lined stainless steel autoclave and treated for 40 hours at 388 K in a rotating oven at 20 rpm. The product was cooled and washed with distilled water until the pH of the washing solution was

lower than 9. The final product was dried for 12 hours at 343 K and treated in flowing synthetic air ($100 \text{ mL}\cdot\text{min}^{-1}$) at 823 K (heating rate of $1 \text{ K}\cdot\text{min}^{-1}$).

The synthesis of the self-pillared silicalite nanosheets was performed adding tetraethyl orthosilicate (170 mmol) to a 40 vol. % solution of tetra-n-butylphosphonium hydroxide (51 mmol) dropwise while stirring. Distilled water was added and the mixture was stirred for 12 hours at room temperature and transferred to a Teflon-lined stainless steel autoclave and heated for 40 hours at 388 K with stirring. The product was cooled and washed with distilled water until the pH of the washing solution was lower than 9. The final product was dried for 12 hours at 343 K and treated in flowing air ($100 \text{ mL}\cdot\text{min}^{-1}$) at 823 K (heating rate of $1 \text{ K}\cdot\text{min}^{-1}$) for 12 hours. The materials were stirred in a suspension of distilled water for 12 h at 343 K. The proton forms of the materials were obtained by mixing the solids with 1 M ($80 \text{ g}\cdot\text{L}^{-1}$) solutions of ammonium nitrate. This suspension was heated at 343 K while stirring for 5 hours and the solid was recovered by centrifugation. This process was repeated three times. The final product was dried at 343 K for 12 hours and treated in flowing air ($100 \text{ mL}\cdot\text{min}^{-1}$) at 673 K (heating rate of $1 \text{ K}\cdot\text{min}^{-1}$) for 4 hours.

2.3.2 Synthesis of Ni catalysts

Ni was incorporated *via* the deposition-precipitation method ¹⁰. The procedure consisted in preparing a solution of nickel nitrate (35 mmol) in 250 mL of deionized water. An aliquot of 40 mL of this solution was used for dissolving urea (105 mmol) and the remaining volume (210 ml) was mixed with a sample of solid support. The suspension was refluxed at 363 K. When the temperature of the suspension reached 343 K, the solution of nickel nitrate and urea was added dropwise. After 43 min at 363 K, the suspension was cooled to room temperature, filtered and the solid was washed with deionized water at 333 K. After drying at 343 K for 24 h, the catalyst precursor was subsequently treated in flowing synthetic air ($100 \text{ mL}\cdot\text{min}^{-1}$) at 673 K (heating rate of $1 \text{ K}\cdot\text{min}^{-1}$) for 4 h and in hydrogen ($100 \text{ mL}\cdot\text{min}^{-1}$) at 733 K (heating rate of $2 \text{ K}\cdot\text{min}^{-1}$) for 4 h.

2.3.3 Chemical and physicochemical characterization

Elemental analysis of all materials was performed *via* atomic adsorption spectroscopy with an Unicam M Series Flame-AAS instrument equipped with an FS 95 auto-sampler and a GF 95 graphite furnace. Powder X-ray diffraction patterns were recorded with a Philips X'Pert Pro system ($\lambda\text{CuK}\alpha = 0.154056$ nm, 40 kV/40 mA) with a step size of 0.017° and a scan speed of 0.3 s per step. Transmission electron micrographs were recorded with a JEOL JEM-2011 TEM instrument with a maximum acceleration of 120 kV. Scanning electron microscopy measurements were performed on a JEOL JSM 7500F SEM. Shape, primary particle size and morphology of the materials were determined from TEM and SEM images. Particle size determination was done based on the evaluation of at least 300 particles. Nitrogen physisorption was carried out at 77 K on a PMI automated sorptometer after outgassing the samples under vacuum at 523 K for 2 h. The BET isotherm was used to evaluate the apparent specific surface area over a relative pressure range of 0.01-0.1 p/p_0 . The micro- and mesopore volumes were evaluated by using non-porous hydroxylated silica as the reference adsorbent ¹¹. The macro-pore volume was calculated by subtracting micro- and mesopore volumes from the total pore volume determined at $p/p_0 = 0.95$. The pore size distribution of the zeolites was evaluated by the DFT method (cylindrical pore, NLDFT equilibrium model). Particle size of the supports was determined from TEM and SEM images.

The concentration of chemisorbed H_2 on Ni was determined with a Sorptomatic 1990 instrument. Samples were treated in a flow of H_2 at 723 K for 1 h and then evacuated at the same temperature for 1 h before measurements. Hydrogen adsorption was conducted at 307 K in a pressure range of 0.5–13.2 kPa with an equilibration time of 5 min. After completing the first isotherm, the sample was evacuated to 10^{-4} kPa and a second isotherm was measured. The second isotherm (physisorption) was subtracted from the first one. The amount of chemisorbed hydrogen was determined by extrapolating the linear part of the difference isotherm ($P > 6.5$ kPa) to zero pressure. The concentrations of chemisorbed H_2 were calculated assuming an H/Ni stoichiometry of 1.

Infrared spectroscopy of adsorbed pyridine and 2,6-di-tert-butyl-pyridine (2,6-DTBPY) as probe molecules was used to determine the total concentration and location of Brønsted and Lewis acid sites ^{12, 13}. The instrument used for the experiments was a Thermo Nicolet 5700 FT-IR spectrometer with a resolution of 4 cm^{-1} . All samples were

pressed into self-supporting wafers (density $\sim 0.01 \text{ g}\cdot\text{cm}^{-3}$) and activated under vacuum ($p < 10^{-7} \text{ kPa}$) for 1 h at 723 K (heating rate of $10 \text{ K}\cdot\text{min}^{-1}$). The activated materials were exposed to pyridine or 2,6-DTBPY at 0.01 kPa and 423 K for 0.5 h and evacuated for 1 h to desorb weakly bound molecules. The bands at $\sim 1545 \text{ cm}^{-1}$ and $\sim 1450 \text{ cm}^{-1}$ were integrated to determine the total concentration of Brønsted and Lewis acid sites, respectively. The samples were subsequently heated to 723 K ($10 \text{ K}\cdot\text{min}^{-1}$) for 0.5 h in vacuum to determine the concentration of strong Brønsted and Lewis acid sites. The concentration of Brønsted acid sites interacting with 2,6-DTBPY was calculated by integrating the N-H⁺ stretching vibration band at 3367 cm^{-1} ¹³. All spectra were collected at 423 K. The acid site concentrations reported were normalized to the weight of the sample.

2.3.4 Activity tests

The experiments were performed in a 45890HP Parr vessel. Preliminary experiments employing varying particle sizes and stirring rates discarded the presence of diffusion artefacts. All reactions were conducted at a hydrogen pressure of 40 bar with 84.7 mg (5 mmol) of eicosane as an internal standard and 45 g of dodecane as solvent. 89.5 mg (5 mM) methyl stearate, or tristearate (1.66 mM), or 89.5 mg microalgae oil (the composition of microalgae oil is given in Table S1) were used as reactants. Samples of 30 mg of the catalysts were reduced as described before and immediately employed in the reaction. Catalyst stability was tested using Ni/n-H-ZSM-5 in the conversion of microalgae oil in four consecutive runs. After each run, new reactant solution was introduced into the reactor. This was performed under H₂ flow in order to avoid exposure of the catalyst to air. Prior to the reaction, the reactor was filled with 15 bar hydrogen and purged three times. As soon as the temperature reached 553 K, the pressure inside the reactor was set to 40 bar with hydrogen. Aliquots of the liquid phase were periodically extracted from the reactor and analyzed offline by a gas chromatograph (GC, Agilent Technologies 7890B GC) connected to a flame ionization detector (FID) and a mass spectrometer (MS, Agilent Technologies 5977A). The GC was equipped with a HP-5 capillary column. Quantification was done based on the internal standard and an external calibration of the GC-FID signal of each compound. The molar carbon balance was always higher than 97%. The gas phase was analyzed offline with an Agilent 7890B gas chromatograph with a FID. The GC was equipped with molsieve 13x, DB-1, and Hayesep Q columns.

Reaction orders of methyl stearate and triglyceride conversions were determined to be unity using the integrated rate law. First-order rate constants were calculated taking into account the complete concentration profiles. The R^2 value of the regression line was typically above 0.98.

2.4 Results and discussion

2.4.1 Characterization

Four parent supports and four Ni catalysts were obtained by the procedures described above. In the following the supports are labeled as H-ZSM-5 (aluminosilicate MFI type zeolite with conventional porosity), Silicalite 1 (silicate MFI type zeolite with conventional porosity), n-H-ZSM-5 (aluminosilicate zeolite with MFI framework and self-pillared nanosheet structure), and n-Silicalite 1 (silicate zeolite with MFI framework and self-pillared nanosheet structure). The corresponding catalysts are denoted as Ni/H-ZSM-5, Ni/Silicalite 1, Ni/n-H-ZSM-5, and Ni/n-Silicalite 1.

2.4.2 Characterization of the catalysts

Representative TEM images of the catalysts are shown in Figure 1. In the materials with conventional morphology (Ni/H-ZSM-5 and Ni/Silicalite 1), the particles of the support have projected rectangular shapes of about 200 x 360 nm. SEM images (Figure S1 in the supporting information) of the support confirmed this shape. The small agglomerates observed at the perimeters of the supports in TEM images are identified as Ni particles. In contrast, the supports with nano-sized structure (Ni/n-H-ZSM-5 and Ni/n-Silicalite 1) consist of round rough particles with diameters of about 100 nm. These particles are agglomerates of orthogonally linked microporous nanosheets with height of 8 nm and lengths of 20 – 100 nm. The Ni particles are observed as small dark dots within the crystalline domains and on the outer surface of the support particle. The morphologies of H-ZSM-5 and Silicalite 1 were nearly identical within the conventional or nano-structured series. The morphologies shown in Figure 1 for the nano-structured materials (Ni/n-H-ZSM-5) allow to assign the broad distribution of mesopores detected by N_2 -physisorption (*vide infra*) to cavities between the nano-sized crystals and to inter-crystalline voids between the particles. Moreover, the Ni particles observed in Figure 1 evidence the large differences of Ni particle sizes between the series with conventional and nano-structured morphology.

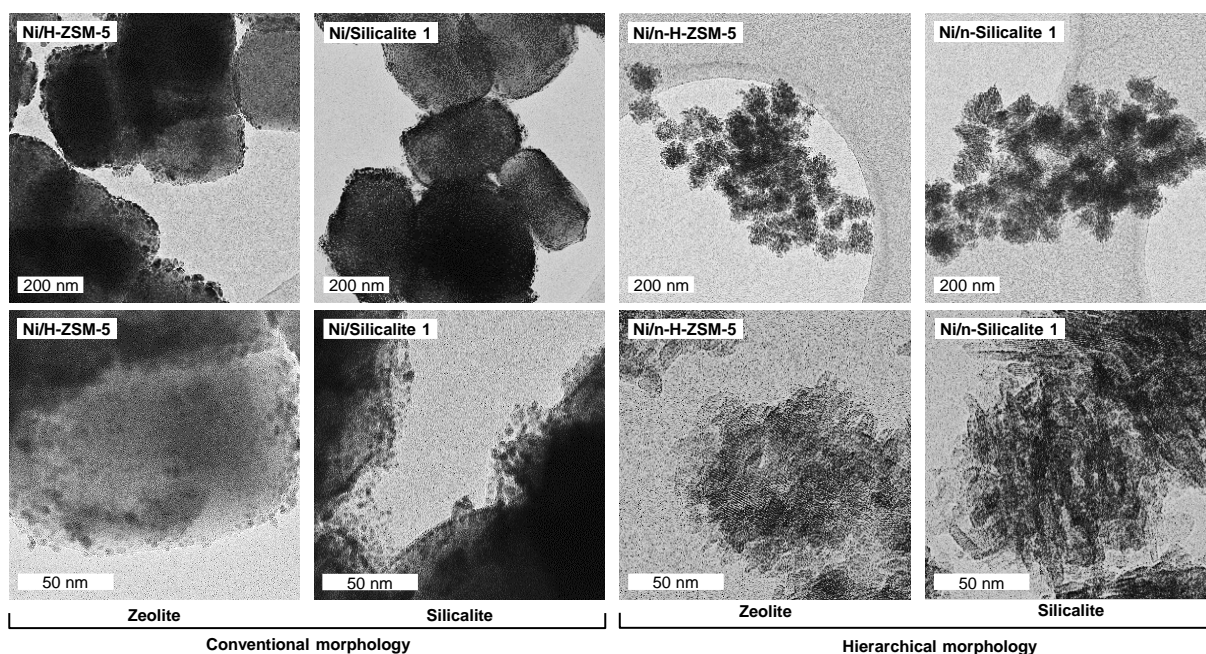


Figure 1. Representative micrographs of Ni supported on (n)-H-ZSM-5 and (n)-Silicalite 1 materials. Note the cross-linking between crystalline sheets for the nanosheet materials (n-H-ZSM-5 and n-Silicalite 1), which produces mesoporosity. The dark dots in all images are nickel particles.

The X-ray patterns of the catalysts (Figure S2 and Figure S3 in supporting information) show the characteristic main reflections at $2\theta = 8.3^\circ, 9.2^\circ, 23.5^\circ, 24.3^\circ,$ and 24.8° of MFI framework zeolites¹⁴. The patterns of the nanosheet materials (Ni/n-H-ZSM-5 and Ni/n-Silicalite 1) have peaks at the same positions although broader. This indicates that the same crystallographic phase is present in all materials although with very different crystal size. The broader XRD reflections of the n-H-ZSM-5 materials are caused by the small crystalline domains⁸. The X-ray diffractograms of the parent supports show also that the MFI framework was not affected by the Ni deposition. The X-ray diffractograms of the catalysts showed, moreover, reflections at $2\theta = 44.5^\circ,$ and $52.8^\circ,$ assigned to the (111) and (200) planes of Ni (FCC).

The micropore and mesopore volumes (V_{micro} , and V_{meso} , respectively) of the catalysts with conventional and nano-structured structure differed greatly (Table 1). The nanosheet materials (Ni/n-H-ZSM-5 and Ni/n-Silicalite 1) had mesopore volumes, which were one order of magnitude higher than those of conventional counterparts (Ni/H-ZSM-5 and Ni/Silicalite 1). The micropore volumes of the nanosheet materials were, in contrast, 2.5 times smaller than those of the materials with conventional

morphology. Deposition of Ni led to a decrease of the micropore volume of nanosheet materials by a factor of 10 (Table 1). This indicates that Ni particles either selectively fill or block a large fraction of micropores of the nano-structured materials. The Si/Al ratios of the aluminosilicate materials were comparable (92 and 108 for H-ZSM-5 and n-H-ZSM-5, respectively).

The N₂ physisorption isotherms and pore size distributions of the materials hardly changed upon Ni deposition (Figure 2, and Figure S5). The series of materials with conventional morphology shows type I isotherms, typical for microporous materials, whereas the series with nano-structured morphology exhibits type IV isotherms with hysteresis loops at relative pressures above 0.6, indicative of mesoporous systems. Figure 2 shows the homogeneous distribution of micropores in the series with conventional morphology and the large contribution of mesopores (with diameters mainly below 150 Å) for the series with nano-structured morphology.

Table 1. Ni content (Ni), accessible Ni atoms (accessible Ni), Si/Al ratio (Si/Al), total pore volume (V_{total}), micropore volume (V_{micro}), mesopore volume (V_{meso}), average mesopore diameter (\varnothing_M), and Ni particle diameter (\varnothing_{Ni}) of supports and Ni catalysts.

Material	Ni [wt.%]	\varnothing_{Ni}^a [nm]	Accessible Ni ^a [$\mu\text{mol g}^{-1}$]	Si/Al	V_{total} [$\text{cm}^3 \text{g}^{-1}$]	V_{micro} [$\text{cm}^3 \text{g}^{-1}$]	V_{meso} [$\text{cm}^3 \text{g}^{-1}$]	\varnothing_M [nm]
H-ZSM-5	-	-	-	92	0.21	0.14	0.07	-
Silicalite 1	-	-	-	-	0.18	0.13	0.09	-
n-H-ZSM-5	-	-	-	108	0.95	0.055	0.90	20
n-Silicalite 1	-	-	-	-	0.84	0.06	0.78	20
Ni/H-ZSM-5	9.7	12.9	128	92	0.22	0.15	0.07	-
Ni/Silicalite 1	10.1	8.4	207	-	0.24	0.13	0.11	-
Ni/n-H-ZSM-5	9.3	4.5	349	108	0.80	0.004	0.79	20
Ni/n-Silicalite 1	9.8	4.7	370	-	0.76	0.006	0.75	20

^a Determined based on H₂ chemisorption and elemental analysis.

Quantification of the acid sites at the external surface of the zeolite was performed *via* adsorption of 2,6-di-*tert*-butyl-pyridine (2,6-DTBPY). The difference spectrum, i.e., the spectrum of the zeolite subtracted from the spectrum recorded after 2,6-DTBPY adsorption (Figure S4 in supporting information) showed that a fraction of terminal SiOH groups (3745 cm^{-1}) and Brønsted acid sites (3610 cm^{-1}) interacted with 2,6-DTBPY, as the intensity of both bands decreased. New bands appeared at 3370 cm^{-1} and 1616 cm^{-1} , which are assigned to the N-H⁺ vibration of protonated 2,6-DTBPY and to one of its C=C ring vibrations, respectively ¹³.

The acidities of the zeolites, as determined by IR spectroscopy of adsorbed pyridine and 2,6-DTBPY are summarized in Table 2. The total concentration of acid sites was comparable for both materials, i.e., $45\text{-}52\text{ }\mu\text{mol}\cdot\text{g}^{-1}$, and $153\text{-}173\text{ }\mu\text{mol}\cdot\text{g}^{-1}$ for H-ZSM-5, and n-H-ZSM-5, respectively. However, most of the acid sites on n-H-ZSM-5 were strong, whereas 50 % of LAS and 33 % of BAS in H-ZSM-5 were weak. Comparisons of the adsorption of pyridine and 2,6-DTBPY indicated that only 10 % of BAS ($17\text{ }\mu\text{mol}\cdot\text{g}^{-1}$) were accessible for 2,6-DTBPY in H-ZSM-5, whereas 43 % of the BAS ($66\text{ }\mu\text{mol}\cdot\text{g}^{-1}$) were accessible in n-H-ZSM-5.

The Ni catalysts contained Ni loadings of around 10 wt. %. The dispersion of the metal was assessed by XRD, TEM and H₂ chemisorption (Table S2 of the supporting information). Although there are variations for the dispersions of small Ni particles, the trends are identical within the results derived from a specific technique. The average particle sizes of Ni particles were smaller on nanosheet materials than on materials with conventional morphology, whereas Ni particles have very similar sizes within the series ($d(\text{Ni}/\text{H-ZSM-5}) \approx d(\text{Ni}/\text{Silicalite 1}) < d(\text{Ni}/\text{n-H-ZSM-5}) \approx d(\text{Ni}/\text{n-Silicalite 1})$). Small metal particles may escape from detection in XRD and TEM measurements. The former technique is limited to particles with crystalline domains large enough to produce coherent reflection, while the latter is limited by the resolution of the instrument and size of the metal particles. H₂ chemisorption, in contrast, titrates the surface atoms of the metal particles independently of their size. Therefore, the results obtained by H₂ chemisorption were used for calculation of intrinsic activities (Table 1). The concentrations of accessible Ni atoms varied by a factor of 3 between H-ZSM-5 and n-H-ZSM-5, i.e., $128\text{ }\mu\text{mol}\cdot\text{g}^{-1}$ and $349\text{ }\mu\text{mol}\cdot\text{g}^{-1}$, respectively.

2.4.3 Catalytic activity and selectivity

Catalytic activity and selectivity of Ni catalysts (pure (n)-H-ZSM-5 or (n)-Silicalite 1 are not active) for HDO of methyl stearate, tristearate, and microalgae oil were investigated. The kinetic results are compiled in Figures 3, 4, and S4, and in Tables 3 and 4.

2.4.4 Hydrodeoxygenation of methyl stearate

The specific activity (per mass of catalyst) increased in the presence of aluminosilicates and was always higher for the hierarchic material, i.e., Ni/Silicalite 1 < Ni/n-Silicalite 1 < Ni/H-ZSM-5 < Ni/n-H-ZSM-5 (Table 3). Thus, the mesoporosity improved the reaction rates twofold (e.g., $k = 0.36 \text{ h}^{-1}$ on Ni/Silicalite 1, compared to $k = 0.75 \text{ h}^{-1}$ on Ni/n-Silicalite 1), while the use of aluminosilicate instead of silicate based zeolites enhanced the rate by a factor of 3 (e.g., $k = 0.36 \text{ h}^{-1}$ on Ni/Silicalite 1, compared to $k = 1.16 \text{ h}^{-1}$ on Ni/H-ZSM-5). The rate of conversion on Ni/n-H-ZSM-5 was faster than on Ni/H-ZSM-5 by a factor of 4. The activity of Ni supported on nano-structured zeolite (Ni/n-H-ZSM-5), however, was one order of magnitude higher than Ni supported on microporous silicate (Ni/Silicalite 1). That is, the combination of using a zeolite and mesoporosity had a synergistic effect on the activity of the supported metal.

Table 2. Concentrations of acid sites of the conventional and the nano-structured material.

Material	Total acid sites ^a		Strong acid sites ^b		Weak acid sites ^c		Accessible BAS ^d [$\mu\text{mol}\cdot\text{g}^{-1}$]	Inaccessible BAS ^e [$\mu\text{mol}\cdot\text{g}^{-1}$]
	[$\mu\text{mol}\cdot\text{g}^{-1}$]		[$\mu\text{mol}\cdot\text{g}^{-1}$]		[$\mu\text{mol}\cdot\text{g}^{-1}$]			
	LAS	BAS	LAS	BAS	LAS	BAS		
H-ZSM-5	46	173	24	115	22	58	17	156
n-H-ZSM-5	52	153	50	152	1	1	66	87

^a After adsorption of pyridine at 423 K and outgassing for 1 h under vacuum. ^b After subsequently heating the samples of ^a to 723 K for 0.5 h under vacuum. ^c Difference between total concentration of Brønsted/Lewis acid sites and concentration of strong Brønsted/Lewis acid sites. ^d Defined as percentage of 2,6-DTBPY interacting with total Brønsted acid sites. ^e Difference between total concentration of Brønsted acid sites (both strong and weak) and concentration of Brønsted acid sites accessible for 2,6-DTBPY.

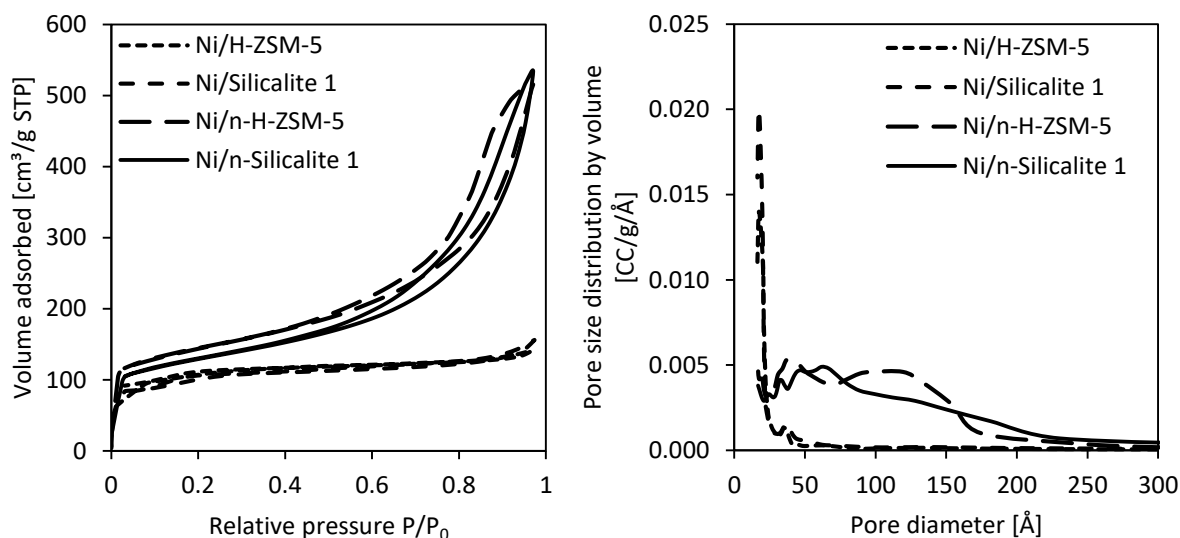


Figure 2. N_2 -physisorption isotherms and pore size distributions of Ni catalysts.

The analysis of the intrinsic activity shows a different picture. The variation of TOFs follows the same trend as that of specific rates ($\text{Ni/Silicalite 1} \leq \text{Ni/n-Silicalite 1} \ll \text{Ni/H-ZSM-5} \leq \text{Ni/n-H-ZSM-5}$). Within the experimental error ($\pm 10\%$), however, TOF on the silicalite based catalysts (Ni/Silicalite 1 and Ni/n-Silicalite 1) are the same ($\sim 20 \text{ h}^{-1}$), whereas for the zeolite based catalysts the activity of Ni/n-H-ZSM-5 is higher than that of Ni/H-ZSM-5 only by 30%. In a word, a nano-structured pore system has little effect on the activity of Ni supported on silicalite and a modest one on the activity of Ni on zeolites. Supporting the Ni particles on aluminosilicate zeolites (H-ZSM-5 or n-H-ZSM-5), on the other hand, increases the intrinsic activity of Ni by a factor of ~ 5 compared to supporting the metal on the corresponding silicate zeolites (Silicalite 1 or n-Silicalite 1).

Figure 3 shows the evolution over time of the concentration of methyl stearate and the products. Stearic acid, stearyl stearate, and octadecanol are intermediate products, having concentrations that pass through maxima; whereas octadecane and heptadecane are final products. These observations allow us to propose the reaction network shown in Figure 5 in agreement with previous reports⁴. Stearic acid is produced by a hydrogenolytic C-O cleavage of methyl stearate or triglyceride, which produces methane or propane as by-products (only alkanes detected in the gas phase). Hydrolysis of methyl stearate to methanol and stearic acid was excluded, as methanol was not detected in the gas and liquid phases while conversion over pure zeolite (which could have catalyzed hydrolysis *via* Brønsted acid sites) was not

observed. A second hydrogenolysis step converts the acid to the highly reactive aldehyde intermediate (stearic aldehyde, not observed in this work), which undergoes decarbonylation to heptadecane, or hydrogenation to octadecanol. Direct decarboxylation of stearic acid, observed over Pt and Pd³, is excluded on Ni catalysts because stearic acid was not converted under N₂ atmosphere. Dehydration of octadecanol (yielding octadecene), and consecutive hydrogenation leads to octadecane as a final product. In parallel to the described steps, esterification of stearic acid and octadecanol yields stearyl stearate only on aluminosilicate-based catalysts (Ni/H-ZSM-5 and Ni/n-H-ZSM-5), when stearic acid is present in relatively high concentrations.

Table 3. First order reaction rate constant, initial rate and turn-over frequency for the hydrodeoxygenation of methyl stearate.

Catalyst	Reaction rate constant k^a [h ⁻¹]	Initial reaction rate r_0^b [mmol·(h·g _{cat}) ⁻¹]	Turnover frequency ^c [mol _{reactant} ·(mol _{accessible Ni} ·h) ⁻¹]
Ni/H-ZSM-5	1.16	12.0	94
Ni/Silicalite 1	0.36	4.0	19
Ni/n-H-ZSM-5	4.42	44.0	126
Ni/n-Silicalite 1	0.75	8.0	22

^a Calculated via the integrated rate law taking into account the concentration profile during the entire reaction time. ^b Calculated at zero reaction time as the product of the rate constant and initial concentration. ^c Determined by normalizing the initial rates with the concentration of surface Ni atoms.

Stearic acid was not observed on silicate based catalysts (Ni/Silicalite 1 and Ni/n-Silicalite 1), which implies that the hydrogenolysis of the Csp²-O bond of the acid is faster than that of the Csp³-O bond of the methyl stearate. Furthermore, octadecane is not observed and very low concentrations of octadecanol are formed. This is due to the absence of Brønsted acid sites on silicalite, which hinder the dehydration of octadecanol. As a consequence, only the decarbonylation pathway towards heptadecane is available to convert the octadecanal-octadecanol pair, which likely reaches equilibrium even at low reaction times.

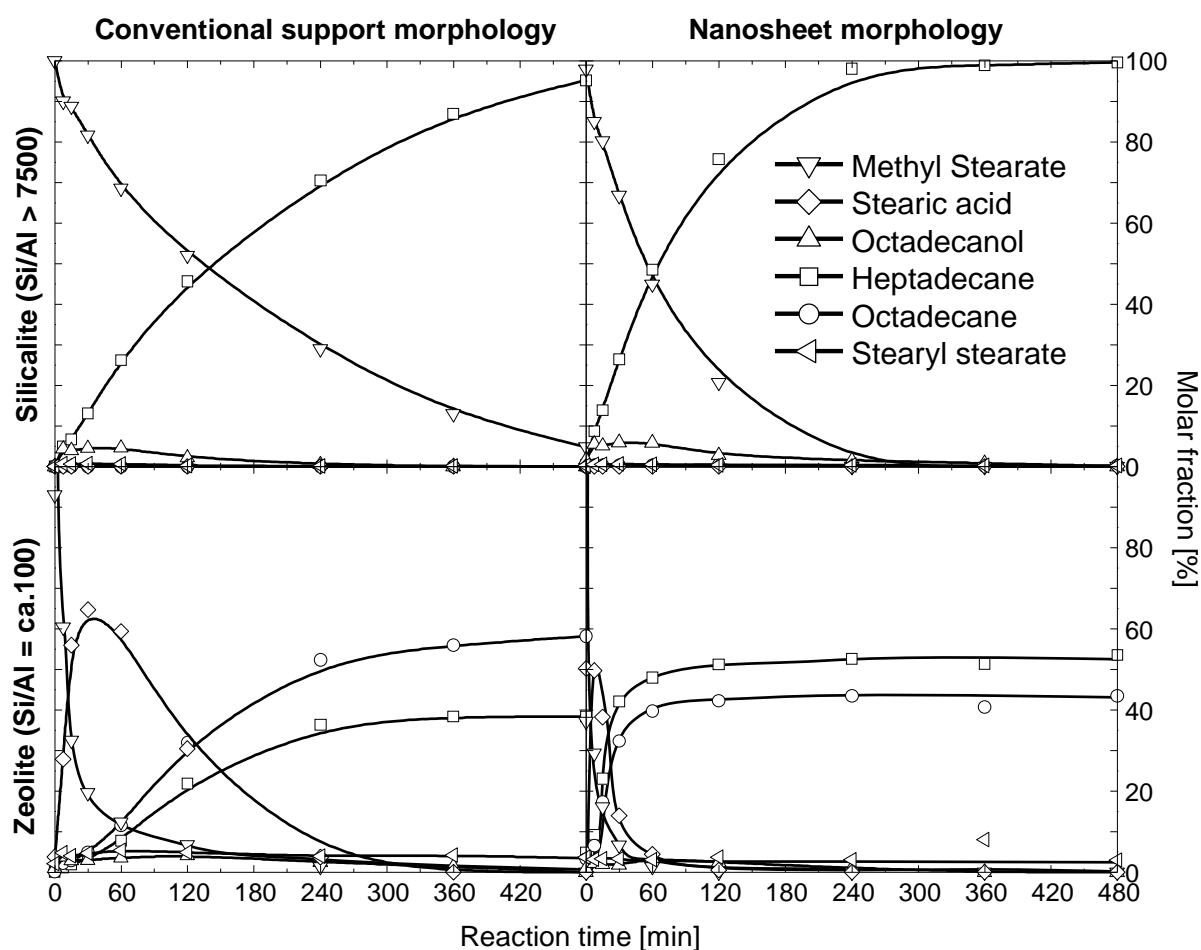


Figure 3. Evolution of the concentrations of methyl stearate and reaction products over time on the catalysts with different morphology and acidity. Reaction carried out with methyl stearate as reactant (5 mmolar in dodecane) at 40 bar H_2 and 553 K.

In contrast to Ni supported on silicates, stearic acid was observed on aluminosilicate based zeolites (Ni/H-ZSM-5 and Ni/n-H-ZSM-5), which indicates that the Csp^3-O hydrogenolysis of the methyl stearate is faster than that of the Csp^2-O bond of the acid. As the aluminosilicate catalysts are much more active than the silicalite counterparts, we conclude that supporting Ni on zeolite enhances the Csp^3-O cleavage to a larger extent than the Csp^2-O cleavage. The most distinctive feature of Ni on zeolites is that octadecane is the main final product, which indicates that the dehydration of octadecanol, followed by hydrogenation of the octadecene intermediate is faster than the decarbonylation of octadecanal.

2.4.5 Hydrodeoxygenation of tristearate and microalgae oil

While the sequence of catalytic activities for tristearate and microalgae oil, normalized to mass of catalyst, was the same than that observed for methyl stearate, i.e., Ni/Silicalite 1 < Ni/n-Silicalite 1 < Ni/H-ZSM-5 < Ni/n-H-ZSM-5 (Table 4), it should be noted that the reactivity of methyl stearate was lower than that of tristearate or microalgae oil. We hypothesize that this is caused by a higher heat of adsorption of the latter, directly influencing the measured rates, as the reaction order was determined to be one. Considering the performance of Ni/Silicalite 1 as the reference, catalysts with nano-structured supports were approximately three times more active. Similar observations were made for the conversion of microalgae oil. The use of zeolite instead of silicalite as a support enhanced the rate by a factor of five (e.g., $k = 0.4 \text{ h}^{-1}$ on Ni/Silicalite 1, compared to $k = 2 \text{ h}^{-1}$ on Ni/H-ZSM-5). The conversion rates on Ni/n-H-ZSM-5 were higher than on Ni/H-ZSM-5, and Ni/Silicalite 1 by factors of 4 and 20, respectively. Thus, the use of zeolite and hierarchical pore systems have positive effects on the activity of the catalysts for the conversion of the three feeds.

Despite of different morphologies (conventional or nano-structured), TOFs are comparable on materials with the same composition (aluminosilicate or silicate) following the trend Ni/Silicalite 1 \leq Ni/n-Silicalite 1 \ll Ni/H-ZSM-5 \leq Ni/n-H-ZSM-5. Thus, the hierarchic materials stabilize smaller Ni particles and the higher reaction rates per mass of catalyst on Ni supported on nano-structured materials are due to better metal dispersion. In contrast, the use of zeolite instead of silicalite as a support enhances the TOF by an order of magnitude (e.g., TOF=17 h^{-1} on Ni/Silicalite 1, compared to 158 h^{-1} on Ni/H-ZSM-5).

The products of tristearate conversion in the liquid phase were identical to the products observed for methyl stearate conversion, i.e., stearic acid, stearyl stearate, octadecanol, octadecane and heptadecane. This indicates direct Csp³-O hydrogenolysis of the ester bond of glycerol and stearic acid. The product distributions, including the evolution of products over time, for the HDO of tristearate and microalgae oil are similar (Figure 4 and Figure S6). On the catalysts based on aluminosilicate zeolite with conventional morphology, the conversion of triglyceride yielded more octadecane than the conversion of methyl stearate. We attribute this to competitive adsorption of methyl stearate on Brønsted acid sites, which reduces the rate of octadecanol conversion to octadecane. In contrast, the triglycerides are too bulky to

access the micropore system of the zeolite, where most of the acid sites are located. Thus, dehydration of the alcohol on Brønsted acid sites occurs rapidly in the presence of triglycerides, resulting in higher selectivity to octadecane than in the presence of methyl stearate. Besides this, the evolution of reactant and products and their dependence on catalyst composition is the same as that described for methyl stearate. Thus, the nature of the reactants (methyl stearate, tristearate, or a mixture of triglyceride) mainly influences the overall rates, whereas the selectivities are affected to a lower extent. A general reaction network is shown in Figure 5.

During recycling experiments, the reaction rate of triglyceride conversion on Ni/n-H-ZSM-5 stayed constant within the measuring error (Figure S7). Changes in the reaction order were not detected, i.e., a first order behavior was observed in all runs. Hence, deactivation does not take place under the reaction conditions explored. In line with the catalytic stability, the X-ray diffractograms of the spent catalysts were almost identical to those of the fresh catalysts (Figure S8 and S9). This indicates, that the support and Ni particles are structurally stable under the conditions applied in this study.

2.4.6 On the effects of mesoporosity and composition of the support on the hydrodeoxygenation reactions

Nickel catalyzes the initial hydrogenolytic steps of the reaction network. The Brønsted acid sites, on the other hand, catalyze the conversion of the intermediately formed alcohol via dehydration or esterification. This is an important role, because the selectivity of the final products depends to a large extent on the ability of the catalyst to dehydrate the alcohol. If this functionality is missing, then equilibrium between the alcohol and octadecanal favors carbon loss, because Ni is very active for decarbonylation of the latter ¹⁵.

The question arises as to how the presence of mesoporosity influences the performance of the catalysts. The results here demonstrate that nano-structured systems lead to more active catalysts than large crystal MFI type zeolites in line with results obtained for catalysts supported on BEA ¹⁶. The main cause for the higher activities is the higher dispersion of Ni of the nano-structured materials. Note that the concentration of exposed Ni atoms is up to a factor of 3 higher on the nanostructured materials than on the typical morphologies. This is likely due to the high specific surface

area accessible to deposit Ni particles in the nano-structured supports compared to the conventional counterparts.

The morphology of the support showed only a modest positive effect on the intrinsic metal activity i.e., the ratios of the TOFs observed on nano-structured catalysts divided by the TOFs observed on conventional catalysts are all above 1 but below 2. Therefore, there are not large differences in the concentration of Ni sites available for methyl stearate, tristearate, and triglycerides on the catalysts. Consequently, as the examined triglycerides are too bulky to enter the micropore system of MFI type zeolites, the majority of the active Ni has to be located on the outer surface of the supports.

The dimensions of support and nickel particles in different catalysts as well as the triglyceride are schematically compared in Figure 6. The figure shows the higher Ni dispersion on the nano-structured materials.

Table 4. First order reaction rate constant, initial rate and turn-over frequency for the hydrodeoxygenation of tristearate, and microalgae oil^a.

Catalyst	Reaction rate constant [h ⁻¹]		Initial reaction rate r_0 [mmol·(h·g _{cat}) ⁻¹]		Turnover frequency [mol _{reactant} ·(mol _{accessible Ni} ·h) ⁻¹]	
	Tristearate	Microalgae oil	Tristearate	Microalgae oil	Tristearate	Microalgae oil
Ni/ H-ZSM-5	2.0	2.6	20.2	25.8	158	201
Ni/ Silicalite 1	0.4	0.3	3.5	3.1	17	15
Ni/n-H- ZSM-5	8.4	8.0	84.0	80.4	241	230
Ni/n- Silicalite 1	1.1	0.9	10.7	8.9	29	24

^a The parameters corresponding to tristearate and microalgae oil were calculated based on the product formation with first order kinetics. ^b Calculated by dependence of conversion on reaction time with first order kinetics. ^c Calculated at zero reaction time. ^d Determined by normalizing the initial rates with the concentration of surface Ni atoms (supporting information).

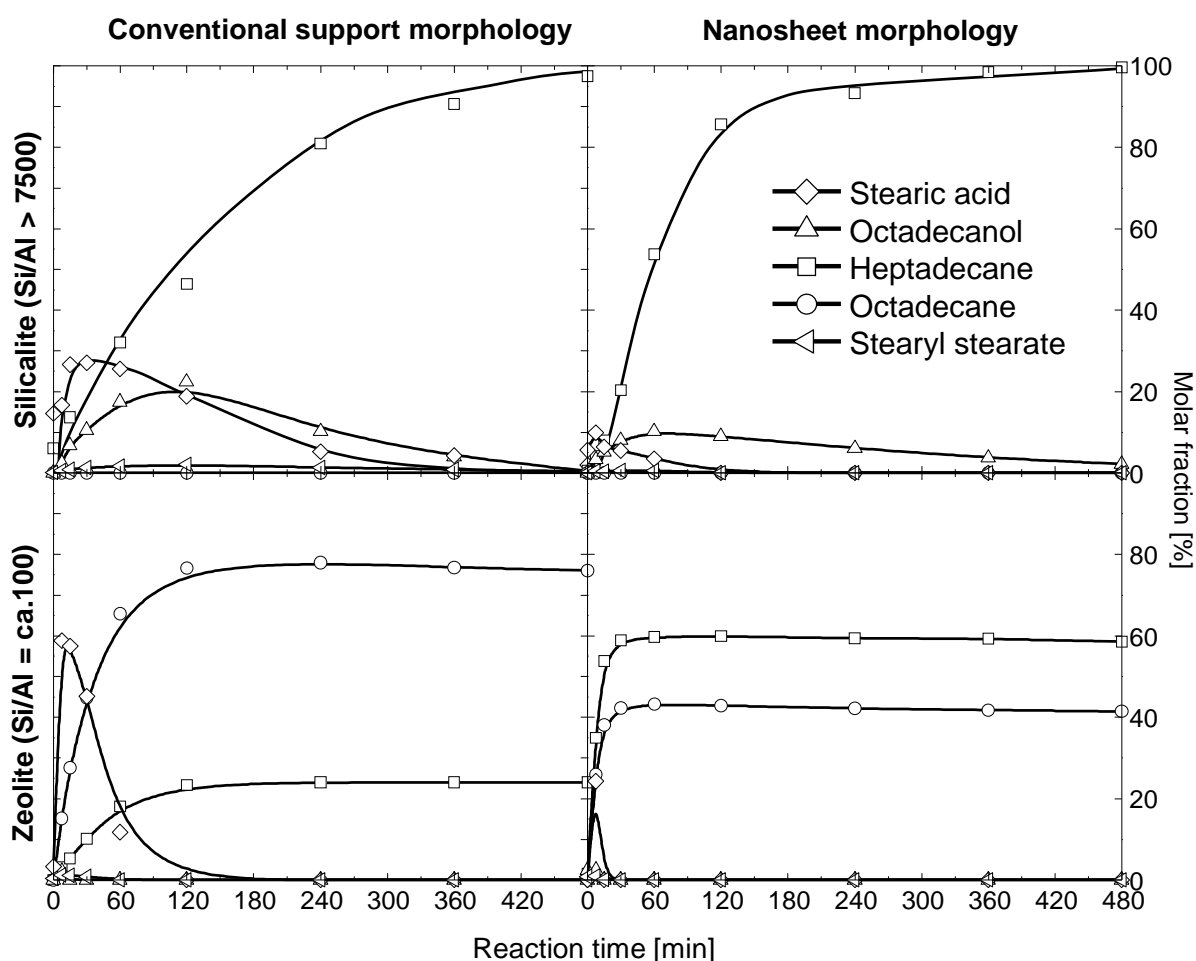


Figure 4. Evolution of the concentrations of reaction products of tristearate conversion over time on the catalysts with different morphology and acidity. Reaction carried out with tristearate as reactant (1.66 mmolar in dodecane) at 40 bar H_2 and 553 K.

The main factor increasing the intrinsic activity of the catalyst is the composition. We attribute this promoter effect to acidity as it is the only property intrinsically changing with composition. This metal-support effect is known for hydrogenation^{17, 18, 25}, C-C hydrogenolysis^{19, 25}, ring enlargement^{20, 25}, and isomerization^{21, 25}. Effects of acid sites on C-O cleavage, however, have been reported only recently²²⁻²⁴. Many explanations have been put forward for this effect, e.g., decreased electron density at the metal due to withdrawing toward acid sites¹⁹, and interactions of metal sites and protons from the BAS²⁶. All theories invoke increasing polarization of the metal sites. Our results suggest that this polarization originates from a direct interaction between Brønsted acid sites with Ni particles, as a significant Brønsted acid site concentration was found on the outer surface/pore mouths of both aluminosilicate based catalysts.

However, it is not in the scope of this work to test this proposal. Further studies are being carried out.

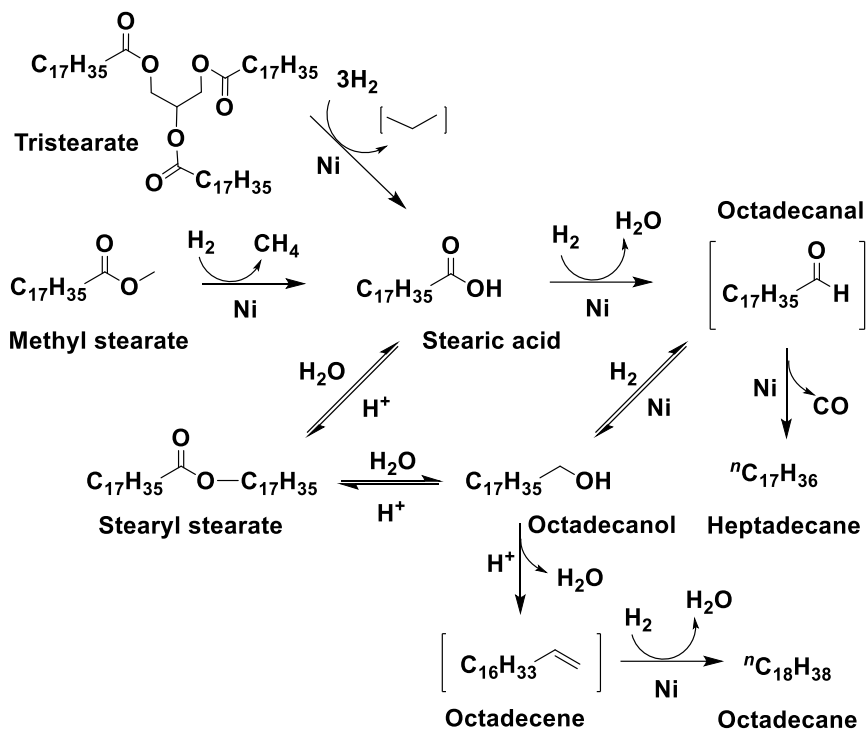


Figure 5. Reaction network for the hydrodeoxygenation of tristearate and methyl stearate. "Ni" and "H⁺" denote steps catalyzed by metal and acid sites. Compounds in brackets were not observed in this study.

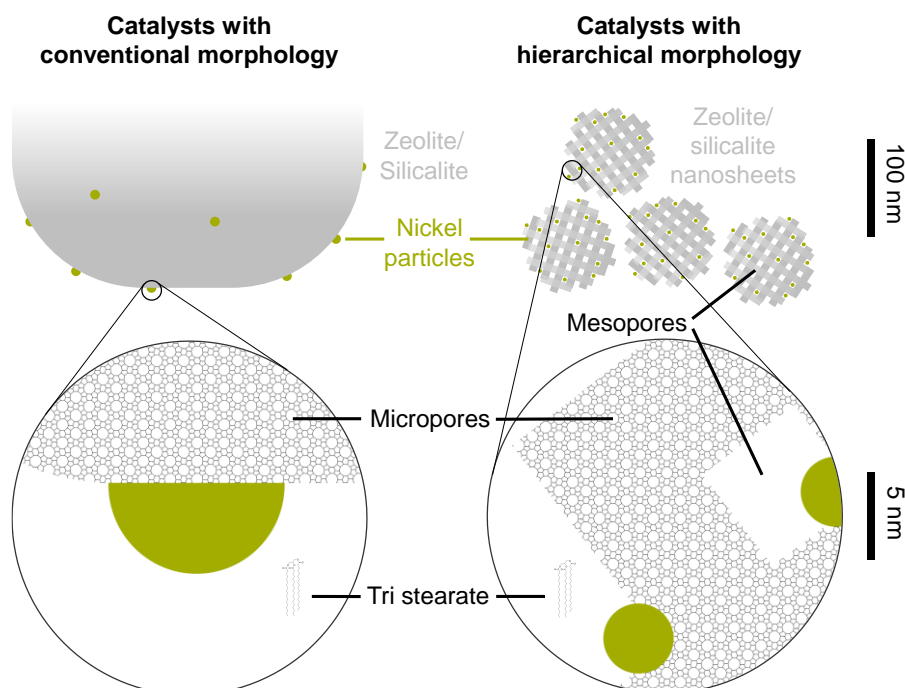


Figure 6. Graphical representation of catalysts with conventional and nano-structured morphology.

2.5 Conclusions

Ni catalysts supported on hierarchical materials, i.e., self-pillared nanosheets, are more active in deoxygenation of methyl stearate, tristearate, and algae oil than the counterparts with conventional structure. The high Ni activity attained on the hierarchical materials are due to outstanding metal dispersion as rates normalized to accessible Ni (TOF) on catalysts with hierarchical and conventional structure are comparable. TOFs of methyl stearate and triglyceride conversion, being independent of support morphology, indicate that the majority of Ni particles are located on the outer surface of the supports (triglycerides are too bulky to access the micropore system of MFI type zeolites).

Interestingly, the acidity of the support has a strong positive influence on the intrinsic activity of Ni. Therefore, the most active catalyst relies on the highest Ni dispersion in the presence of nano-sized crystallites as well as on the highest concentration of acid sites.

Overall, self-pillared zeolite nanosheets have an important potential as catalytic supports for bulky reactants that do not access the microporous system. This is because its small particle sizes and hierarchical support morphology increase the concentration of accessible acid sites by factors of 3-4 and provide a one order of magnitude higher mesopore volume for metal deposition compared to conventional zeolite supports.

2.6 Acknowledgements

The authors thank Roel Prins and Gary L. Haller for the critical discussion of the manuscript. We are also grateful to Andreas Ehrmaier, Marco Peroni, and Marianne Hanzlik for TEM measurements, Martin Neukamm for AAS measurements and Xaver Hecht for chemisorption and physisorption measurements. Financial support for M. W. S. in the framework of the AlgenFlugKraft project (LaBay74) of the Bavarian Ministry of Economic Affairs and Media, Energy and Technology (Bayerisches Staatsministerium für Wirtschaft und Medien, Energie und Technologie) and of the Bavarian State Ministry of Education, Science and the Arts (Bayerisches Staatsministerium für Bildung und Kultus, Wissenschaft und Kunst) is highly appreciated.

2.7 References

1. J. C. Serrano-Ruiz, R. M. West and J. A. Dumesic, *Annu. Rev. Chem. Biomol. Eng.*, 2010, **1**, 79.
2. C. Zhao, T. Brück and J. A. Lercher, *Green Chem.*, 2013, **15**, 1720.
3. R. W. Gosselink, S. A. W. Hollak, S.-W. Chang, J. van Haveren, K. P. de Jong, J. H. Bitter and D. S. van Es, *ChemSusChem*, 2013, **6**, 1576.
4. B. Peng, Y. Yao, C. Zhao and J. A. Lercher, *Angew. Chem. Int. Edit.*, 2012, **124**, 2114.
5. H. Zuo, Q. Liu, T. Wang, L. Ma, Q. Zhang and Q. Zhang, *Energy Fuels*, 2012, **26**, 3747.
6. M. Snáre, I. Kubičková, P. Mäki-Arvela, K. Eränen and D. Y. Murzin, *Ind. Eng. Chem. Res.*, 2006, **45**, pp. 5708–5715.
7. J. Pérez-Ramírez, C. H. Christensen, K. Egeblad, C. H. Christensen and J. C. Groen, *Chem. Soc. Rev.*, 2008, **37**, 2530.
8. X. Zhang, D. Liu, D. Xu, S. Asahina, K. A. Cychosz, K. V. Agrawal, Y. Al Wahedi, A. Bhan, S. Al Hashimi, O. Terasaki, M. Thommes and M. Tsapatsis, *Science*, 2012, **336**, 1684.
9. C. Perego and A. Bosetti, *Microporous Mesoporous Mater.*, 2011, **144**, 28.
10. R. Nares, J. Ramírez, A. Gutiérrez-Alejandre, C. Louis and T. Klimova, *J. Phys. Chem. B*, 2002, **106**, 13287.
11. S. J. Gregg, *Adsorption Surface Area and Porosity*, 1982, Second Edition, New York: Academic Press Inc.
12. J. Cejka, H. van Bekkum, A. Corma and F. Schueth, *Introduction to Zeolite molecular sieves*, 2007, Third Edition, Amsterdam: Elsevier Science.
13. A. Corma, V. Fornes, L. Forni, F. Marquez, J. Martinez-Triguero and D. Moscotti, *J. Catal.*, 1998, **179**, 451.
14. M. M. J. Treacy and J. B. Higgins, *Collection of Simulated XRD Powder Patterns for Zeolites*, 2007, Fifth Revised Edition, Amsterdam, Elsevier Science.
15. B. Peng, C. Zhao, S. Kasakov, S. Foraita and J. A. Lercher, *Chem. Eur. J.*, 2013, **15**, 4732.
16. B. Ma, C. Zhao, *Green Chem.*, 2015, **17**, 1692.
17. O. Y. Gutiérrez, Y. Yu, R. Kolvenbach, G. L. Haller and J. A. Lercher, *Catal. Sci. Technol.*, 2013, **3**, 2365.
18. A. de Mallmann and D. Barthomeuf, *J. Chim. Phys. Phys.-Chim. Biol.*, 1990, **87**, 535.
19. Z. Zhang, T. T. Wong and W. M. H. Sachtler, *J. Catal.*, 1991, **128**, 13.
20. T. J. McCarthy, G. D. Lei and W. M. H. Sachtler, *J. Catal.*, 1996, **159**, 90.
21. P. V. Menacherry and G. L. Haller, *J. Catal.*, 1998, **177**, 175.
22. L. Chen, J. Fu, L. Yang, Z. Chen, Z. Yuan and P. Lv, *ChemCatChem*, 2014, **6**, 3482.
23. H. Zuo, Q. Liu, T. Wang, L. Ma, Q. Zhang and Q. Zhang, *Energy Fuels*, 2012, **26**, 3747.
24. W. Song, Y. Liu, E. Baráth, C. Zhao and J. A. Lercher, *Green Chem.*, 2015, **17**, 1204.

25. A. Yu Stakheev and L. M. Kustov, *Appl. Catal. A. Gen.*, 1999, **188**, 3.

26. W.M.H. Sachtler and A.Yu. Stakheev, *Catal. Today*, 1992, **12**, 283.

2.8 Associated Content

2.8.1 Additional Information

See supporting information.

2.8.2 Peer-Reviewed Publication

This chapter is based on the following article:

Moritz W. Schreiber, Daniella Rodriguez-Niño, Oliver Y. Gutiérrez and Johannes A. Lercher, Hydrodeoxygenation of fatty acid esters catalyzed by Ni on nano-sized MFI type zeolites, *Catal. Sci. Technol.*, 2016,6, 7976-7984

2.8.3 Clearance by the Publisher and Coauthors

Reproduced by permission of The Royal Society of Chemistry.

The article can be found on the website of the Royal Society of Chemistry under the following URL:

<http://pubs.rsc.org/en/Content/ArticleLanding/2016/CY/c6cy01598k#!divAbstract>

All coauthors agreed on reproduction of the article in this thesis.

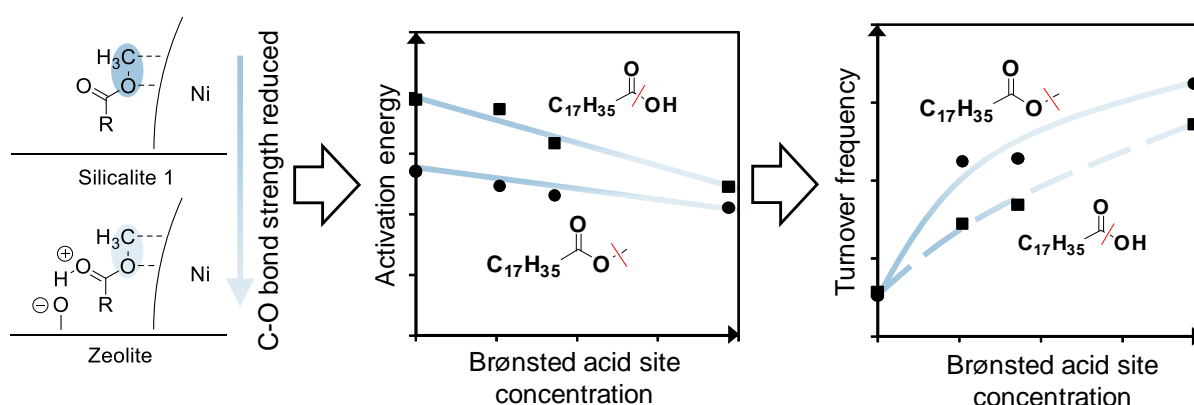
2.8.4 Notes and Author Contributions

Moritz W. Schreiber planned, performed and evaluated synthesis, characterization and kinetic experiments. Daniella Rodriguez-Niño performed and evaluated synthesis, characterization and kinetic experiments within a Master's Thesis. Moritz W. Schreiber drafted the manuscript. Oliver Y. Gutiérrez and Johannes A. Lercher revised the manuscript.

3 Ni-catalyzed C-O hydrogenolysis enhanced by cooperation with Brønsted acid sites on Ni/H-ZSM-5

3.1 Abstract

Rates of methyl stearate and stearic acid conversion on supported Ni catalysts increase in parallel with the concentration of Brønsted acid sites of MFI supports. Thus, the intrinsic rates of C-O hydrogenolysis on Ni are enhanced by Brønsted acid sites. This effect is attributed to the participation of Brønsted acid sites in the reaction, lowering the apparent transition state enthalpy (compensated by increasingly negative apparent transition state entropy). The barrier for the C-O bond cleavage in stearic acid is higher than in methyl stearate, which parallels the corresponding C-O bond dissociation energies. The decrease in reaction barrier is substrate dependent. That is, the rate determining step shifts from the C-O hydrogenolysis of methyl stearate to that of stearic acid in the presence of Brønsted acid sites. Ni works cooperatively with Brønsted acid sites in proximity, i.e., Brønsted acid sites interact with the carbonyl group of the substrate, decreasing the strength of the C-O bond and facilitating its hydrogenolysis on Ni.



3.2 Introduction

Triglycerides can be upgraded by catalytic hydrodeoxygenation (HDO) to alkanes that can be used as drop-in fuels¹. The conversion occurs in a cascade of reactions (hydrogenation, C-O hydrogenolysis, decarbonylation, and dehydration), which require metal and acid sites acting concertedly. As the focus of catalyst development shifts from noble metals to base metals, due to concerns on material stability and cost², Ni supported on zeolites has been found an effective bifunctional catalyst for HDO of bio-oils of diverse origin³⁻⁴. Beyond the role of catalyzing dehydration steps, the acid sites of the zeolite increase the intrinsic activity of the metal for C-O hydrogenolysis in fatty acid esters on Ni supported on H-ZSM-5 and BETA⁵⁻⁶. Such effect of acid supports on the intrinsic activity of metals has been reported for noble metals⁷ for hydrogenation⁸, C-C hydrogenolysis⁹, ring enlargement¹⁰, and isomerization¹¹. In aqueous phase, the TOF for hydrogenolysis of phenolic monomers increased parallel to acid site concentration of Ni/H-ZSM-5¹². This highlights the importance of understanding synergistic effects between metal and acid sites in bifunctional catalysts.

Hence, this work focuses on understanding the enhancing effect of Brønsted acid sites on the intrinsic activity of Ni. We report the characterization of Ni catalysts supported on MFI zeolites with varying concentration of Brønsted acid sites and their catalytic activity for the C-O hydrogenolysis steps in the conversions of triglycerides to alkanes. Lewis acid site concentrations of the supports were minimized. Methyl stearate was chosen as a model compound for this study, because of its structural similarity to triglycerides i.e., both molecules contain an ester functionality, comparable carbon chain length, and similar conversion pathways over supported Ni catalysts under H₂ atmosphere^{3, 13}. We explored the variation in apparent transition state enthalpy and entropy elucidating the origin of the enhancement of intrinsic Ni activity by Brønsted acid sites, suggesting that this correlation originates from the participation of the acid sites in the hydrogen addition reactions.

3.3 Experimental section

3.3.1 Chemicals

All chemicals were purchased from commercial sources and used without further purification. Ammonium hexafluorosilicate (Alfa Aesar, 99.999 %), ammonium nitrate (Sigma-Aldrich, ≥ 99.0 %), dodecane (Sigma-Aldrich, ≥ 99.0 %), eicosane (Aldrich, 99

%), methyl stearate (Alfa Aesar, 99.0%), Ni nitrate hexahydrate (Alfa Aesar, 99.9985 %), sodium aluminate (Riedel de Hään), tetraethyl orthosilicate (Aldrich, 98 %), tetrapropylammonium hydroxide solution (Sigma-Aldrich, 1.0 M in deionized water), urea (Sigma-Aldrich, ≥ 99.0 %).

All gases were obtained from commercial sources and used without further purification. N₂ (Westfalen, > 99.999 %), synthetic air (Westfalen, > 99.999 %), H₂ (Westfalen, > 99.999 %) and Ar (Westfalen, > 99.996 %).

3.3.2 Catalyst preparation

3.3.2.1 Zeolite synthesis

Four MFI materials including three zeolites with varying Si/Al ratio and one silicalite-1 material were synthesized via the hydrothermal synthesis described in the supporting information. The ion exchange was carried out by suspending the wet powder in 90 mL 1 M ammonium nitrate solution and stirring the suspension overnight at 343 K. Subsequently, the liquid phase was separated by centrifugation and discarded. The ion exchange was repeated three times. The obtained materials were dried overnight at 343 K.

Following the synthesis, the zeolites were treated with ammonium hexafluorosilicate in order to minimize the concentration of extra-framework aluminum. Samples (4 g) of H-ZSM-5 90, H-ZSM-5 150, H-ZSM-5 200 and silicalite 1 were suspended in 29 mL, 17 mL, 13 mL and 13 mL, respectively, of a 1 M ammonium hexafluorosilicate solution and stirred vigorously at 353 K for 5 h. Subsequently, the solids were separated by centrifugation and washed six times with 40 mL deionized water. The materials were treated in a flow of synthetic air (100 mL/min) at 823 K (heating rate 10 K/min) for 5 h.

3.3.2.2 Deposition precipitation of Ni

All supports were loaded with Ni *via* the deposition-precipitation method¹⁴. In a typical synthesis a Ni nitrate solution was prepared by dissolving 10.18 g (35 mmol) Ni nitrate hexahydrate in 250 ml of deionized water. The solution was divided in two volumes of 210 mL and 40 mL. The larger volume was transferred into a magnetically stirred 500 mL three neck flask containing 1.9 g of the support. The flask was connected to a reflux

condenser and a thermometer. This suspension was heated to 343 K. In the second volume of the Ni nitrate solution, 6.3 g (105 mmol) urea was dissolved and the resulting solution was added drop wise to the suspension in the three-necked flask. The resulting suspension was further heated to 363 K, kept at this temperature for 40 min and quenched to room temperature. The suspension was vacuum filtered, washed three times with deionized water and dried overnight at 343 K. The obtained green powders were treated at 673 K (heating rate 1 K/min) for 4 h in a flow of synthetic air (100 mL/min) and reduced at 733 K (heating rate 1 K/min) for 5 h in a hydrogen flow (100 mL/min).

3.3.3 Catalyst characterization

3.3.3.1 Atomic Absorption Spectroscopy (AAS)

Atomic absorption spectroscopy was carried out on a *UNICAM 939 AA-Spectrometer* equipped with a GF 95 graphite furnace. The samples were dissolved in a solution of hydrofluoric acid (48 %) and nitro-hydrochloric acid at 383 K before the measurement.

3.3.3.2 N₂ physisorption

The surface area, pore volume and distribution of pore sizes were determined by N₂ adsorption/desorption isotherms at 77 K. The measurements were carried out in a *Thermo Finnigan Sorptomatic 1990 Series*. Prior to adsorption, the samples were evacuated at 473 K for 2 h at 10⁻³ mbar. The total pore volume was calculated based on the Gurvich-rule¹⁵. The mesopore volume was determined by the BJH method¹⁶. The micropore volume was determined by the t-Plot method established by *Lippens and de Boer*¹⁷

3.3.3.3 X-Ray diffraction (XRD)

Powder X-ray diffraction patterns were collected with a *PANalytical X'Pert Pro PW 3040/60* instrument ($\lambda\text{CuK}\alpha = 0.154$ nm, 45 kV/40 mA). The diffractograms were recorded from $2\theta = 5^\circ$ to 70° with a step size of 0.017 °/min and a scan time of 1 h.

3.3.3.4 Transmission electron microscopy (TEM) and scanning electron microscopy (SEM)

The transmission electron microscopy (TEM) measurements were performed with a TEM-instrument (*JEOL JEM-2011*) at 120 kV. The average particle size and its standard deviation as well as the dispersion of the Ni particles was calculated based on the Ni particle size distribution of at least 300 Ni particles measured in more than five regions of the sample. The surface, shape and the porosity of the catalyst were visualized scanning electron microscopy (SEM) via scanning electron microscopy carried out in a *JEOL 500 SEM* microscope.

3.3.3.5 FTIR-spectroscopy of adsorbed pyridine and 2,6-di-*tert*-butylpyridine (DTBP)

The IR measurements were carried out on a *Thermo Nicolet 5700* FTIR spectrometer with a resolution of 4 cm^{-1} averaging 124 scans in a total measuring time of 65 s. The self-supporting wafers were reduced in a flow of $10\text{ mL} \cdot \text{min}^{-1}$ H_2 for 1 h at 723 K with a heating rate of $10\text{ K} \cdot \text{min}^{-1}$ and subsequently outgassed at 10^{-6} mbar for one hour. The concentrations of weak and strong Lewis and Brønsted acid sites were determined as described in the following. After reduction, the samples were exposed to 0.1 mbar pyridine at 423 K for 30 min and outgassed for 1 h to remove the gaseous and physisorbed pyridine. For determination of the strong acid sites, the sample was heated at 723 K (heating rate of $10\text{ K} \cdot \text{min}^{-1}$) for 0.5 h in order to remove weakly chemisorbed pyridine. The concentrations of Brønsted and Lewis acid sites (BAS and LAS, respectively) were derived from the integral of the signals at 1546 cm^{-1} , respectively, normalized to the weight of the wafer. The molar extinction coefficients applied were 4.32 and $3.26\text{ }\mu\text{mol} \cdot \text{cm}^{-2}$ for Brønsted acid and Lewis acid sites, respectively. The accessibility of Brønsted acid sites was determined using 2,6-di-*tert*-butylpyridine instead of pyridine as probe molecule¹⁸. The procedure was similar to the one described for pyridine. The fraction of Brønsted acid sites accessible for 2,6-di-*tert*-butylpyridine was calculated from the decrease of the O-H stretching vibration band of the Brønsted acid sites at 3616 cm^{-1} .

3.3.3.6 Hydrogen chemisorption

H₂ chemisorption measurements were carried out with a *Thermo Scientific Surfer* Sorptiometer. Before the measurement, the sample was reduced in a flow of H₂ for 1 h at 723 K and evacuated 1 h at 573 K. A first adsorption isotherm was measured at 298 K from 0 to 533 mbar. After desorption of physisorbed H₂ for 20 min at 298 K and 10⁻³ mbar, another adsorption isotherm was measured at 298 K from 0 to 533 mbar in order to quantify physisorbed H₂. Subtraction of the second from the first isotherm yielded the isotherm of chemisorbed H₂. The concentration of adsorbed H₂ was calculated based on the metal content (measured *via* AAS) and the y-axis intercept of the extrapolated linear high-pressure part of the H₂ chemisorption isotherm.

3.3.4 Catalytic reactions

The experiments were conducted in a Parr 45890HP autoclave. All reactions were conducted at a H₂ pressure of 40 bar with 84.7 mg (5mmol) of eicosane as an internal standard and 45 g of dodecane as solvent. As reactant 671.6 mg (37.5 mmol) methyl stearate or 640.1 mg (37.5 mmol) stearic acid were used. Samples of 30 mg of the catalysts were reduced in H₂ at 7323 K for 4 h prior to the reaction.

The reactor was filled three times with 15 bar H₂ and subsequently flushed to ensure a pure H₂ atmosphere. The temperature was set to the desired value and stirring was started with a rate of 700 rpm. Control experiments showed the absence of transport artefacts at this stirring rate. As soon as the desired temperature was reached, the pressure of the reactor was set to 40 bar with H₂. Aliquots were periodically extracted and analyzed offline with a gas chromatograph (GC, Agilent Technologies 7890B GC) connected to a flame ionization detector (FID) and a mass spectrometer (MS, Agilent Technologies 5977A). The GC was equipped with a HP-5 capillary column. Quantification was done based on the internal standard and an external calibration of the GC-FID signal of each compound. The carbon balance was always better than 97%.

Reaction rate constants were calculated based on methyl stearate or stearic acid conversion according to the integrated rate law assuming a first order reaction. The R² values of the regression lines were typically above 0.98.

3.4 Results and discussion

3.4.1 Catalyst characterization

Ni catalysts supported on MFI type zeolites with varying Brønsted acid site concentration, i.e., one silicalite and three H-ZSM-5 materials were denominated as Ni/silicalite 1, Ni/H-ZSM-5 250, Ni/H-ZSM-5 180, and Ni/H-ZSM-5 100 according to their Si/Al ratio (Table S1). The characterization of the parent zeolites and materials treated with AHFS is reported in the supporting information. The X-ray diffractograms showed the characteristic pattern of the MFI framework (Figure S3). The reflections were sharp and narrow, indicating a highly crystalline material. This is in line with the uniform, well-defined and medium-sized crystallites observed by scanning electron microscopy (Figure S2). Primary zeolite particles had a platelet shape with a diameter of 340 ± 20 nm and a height of 160 ± 15 nm. Varying the Si/Al ratio did not impact the morphology of the zeolite crystals.

The concentration of Brønsted acid sites ranged from 2 - 97 $\mu\text{mol} \cdot \text{g}^{-1}$ as determined by IR spectroscopy of adsorbed pyridine (Table 1). These concentrations were lower than those of the parent materials (Table S4), which cannot be accounted for by the reduction of the exposed support surface upon deposition of Ni particles. We speculate that some Brønsted acid sites were consumed during the deposition precipitation of Ni due to the heterocondensation of hydroxyl groups and Ni(II) hydroxo-aqua complexes forming a Ni phyllosilicate¹⁹. The dealumination occurring during the deposition of Ni was also associated with decreasing acid site concentration. The concentrations of Lewis acid sites of the catalysts were in the range of 5 - 16 $\mu\text{mol} \cdot \text{g}^{-1}$ (Table 1)

The accessibility of Brønsted acid sites in the pore mouths of supports and the corresponding catalysts was determined by IR spectroscopy of adsorbed 2,6-di-*tert*-butylpyridine (DTBP). Only Brønsted acid sites at the pore mouths of the zeolite are able to adsorb DTBP, because its kinetic diameter (0.7 nm) is significantly larger than the diameter of micropores of the MFI framework (0.56 nm respectively)²⁰. The percentage of Brønsted acid sites of the supports accessible to DTBP was around 10 %. This value is in good agreement with observations for H-ZSM-5 catalysts with comparable crystal size²¹. After Ni loading, the fraction of accessible Brønsted acid sites decreased with increasing Brønsted acid site concentration (up to 12%, 5.9% and 2.5 % for Ni/H-ZSM-5 250, Ni/H-ZSM-5 180 and Ni/H-ZSM-5 100, respectively).

Table 1. Ni content, Ni crystal size/dispersion, and acid properties of the catalysts.

Sample	Ni ^a [wt%]	d Ni ^b [nm]	Dispersion ^b [%]	Si/Al ^a	Acid site concentration ^c [μmol · g ⁻¹]		Accessible BAS concentration ^d	
					LAS	BAS	[μmol · g ⁻¹]	[%]
Ni/H-ZSM-5 100	7.76	11.4	8.89	102	16	113	2.5	2.5
Ni/H-ZSM-5 180	7.83	12.7	7.95	180	13	55	2.5	5.9
Ni/H-ZSM-5 250	7.78	13.4	7.57	250	6	44	3.0	12
Ni/silicalite 1	7.92	8.08	12.5	-	5	0	-	-

3.4.1.1 Ni particles

The concentrations of Ni were around 7.8 wt% on all catalysts (Table 1). The X-ray diffractograms showed diffractions of Ni(0) crystals at 44.50° and 51.86°, which corresponds to the (111) and the (200) planes, respectively (Figure S 4). Based on the full width at half maximum of the (111) reflection the average particle size of the Ni particles was calculated *via* the Scherrer equation to be in between 6.1 and 9.2 nm (Table S3).

The size distribution of Ni particles was symmetric and narrow for all catalysts (Figure S5). The averaged particle size of Ni determined by H₂ chemisorption, TEM, and XRD followed the same trend: d (Ni/silicalite 1) < d (Ni/H-ZSM-5 100) < d (Ni/H-ZSM-5 180) < d (Ni/H-ZSM-5 250) (Table 1, Table S4). As the Ni particle size determined by all methods were significantly larger (above 10 nm) than the micropore size of the MFI framework of the support (0.56 nm), we conclude that most of Ni particles were located on the outer surface of the zeolite particles.

3.4.2 Reaction kinetics

3.4.2.1 Effect of Brønsted acid sites on the intrinsic Ni activity for methyl stearate C-O hydrogenolysis

The rates of methyl stearate conversion to stearic acid increased with increasing Brønsted acid site concentration (Figure 1). Control experiments showed that the zeolites alone were not active for this reaction. Thus, the first C-O bond cleavage is concluded to be a Ni-catalyzed step. Higher conversion rates were attributed to increasing intrinsic activity (turn over frequencies, TOF) of metal particles with increasing Brønsted acid site concentration of the support.

Reaction rates increased by about a factor of 4 (2.2 to $8.5 \text{ mmol}_{\text{Methylstearate}} \cdot (\text{h} \cdot \text{g}_{\text{Catalyst}})^{-1}$) in parallel to an increase of Brønsted acid site concentration from 0 to $113 \mu\text{mol} \cdot \text{g}_{\text{Catalyst}}^{-1}$ (Ni/silicalite 1 and Ni/H-ZSM-5 100). The TOFs increased by a factor of about 6 (from 13 to $81 \text{ mol}_{\text{Methylstearate}} \cdot (\text{mol}_{\text{accessible Ni}} \cdot \text{h})^{-1}$), as the Ni particles on Ni/silicalite 1 compared to Ni/H-ZSM-5 100 catalysts were smaller. This is comparable to the six fold increase of the TOF of phenol hydrodeoxygenation over Ni/H-ZSM-5 compared to Ni/SiO₂¹². For comparison, TOF for the C-C hydrogenolysis of *neo*-pentane increased by one order of magnitude on Pd/HY with a Si/Al of 2 compared to Pd/SiO₂ without Brønsted acid site²².

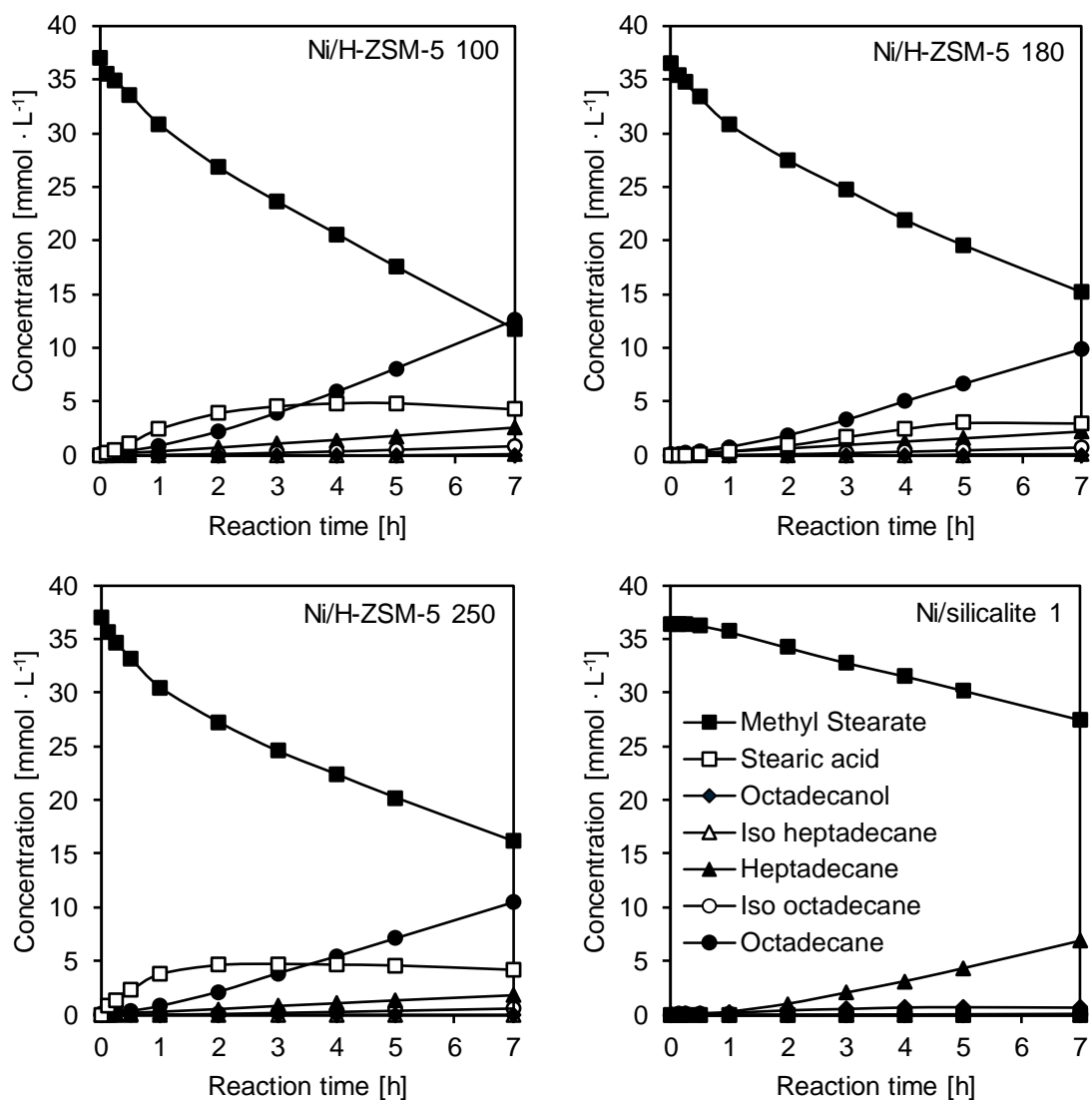


Figure 1. Concentration of methyl stearate, reactions intermediates and products as a function of reaction time for the catalysts with different silica to alumina ratios at 523 K.

Table 2. Rates and TOFs of methyl stearate conversion to stearic acid for catalysts with varying Brønsted acid site concentration.

Sample	Initial rate [mmol _{Methylstearate} · (h · g _{Catalyst}) ⁻¹] ^a	Concentration of accessible Ni atoms [μmol _{accessible Ni} · g _{Catalyst} ⁻¹] ^b	TOF [mol _{Methylstearate} · (mol _{accessible Ni} · h) ⁻¹]
Ni/H-ZSM-5 100	8.5	105	81
Ni/H-ZSM-5 180	6.0	106	57
Ni/H-ZSM-5 250	5.7	100	56
Ni/silicalite-1	2.2	169	13

^a Kinetic results obtained at 523 K, 40 bar H₂.

^b Determined *via* AAS and H₂ chemisorption.

3.4.2.2 Influence of Brønsted acid site concentration on the rate determining step of conversion of methyl stearate to alkanes

Remarkably, a change of the rate-determining step from the conversion of methyl stearate on the silicalite based catalyst (without Brønsted acid sites) to the conversion of stearic acid on the zeolite-based catalysts (containing Brønsted acid sites) was observed.

The intermediate stearic acid accumulated in significant concentrations during the conversion of methyl stearate on Ni supported on acidic zeolites. In contrast, stearic acid was not detected on Ni/silicalite. This implies, in the reaction network of methyl stearate conversion (Figure 2), that the C-O bond cleavage of the ether bond of the methyl stearate (r_1) is faster than that of the hydroxyl group of the carboxylic acid the (r_2) on Brønsted acidic catalysts in contrast to the conversion of methyl stearate ($r_1 < r_2$) on catalyst lacking Brønsted acidity. The observed product distribution at longer reaction times is similar to those previously reported³⁻⁴. The selectivity shifts from *n*-heptadecane to *n*-octadecane with increasing Brønsted acid site concentration (100 % selectivity to *n*-heptadecane on Ni/silicalite and 85 % octadecane and 15 % heptadecane selectivity on Ni/H-ZSM-5 100), as dehydration of the intermediate octadecanol, leading to octadecane is catalyzed by Brønsted acid sites only. In parallel, a small fraction of *n*-alkanes was isomerized on Brønsted acid sites (selectivity of 0.8 % to *iso*-heptadecane and 4.6 % to *iso*-octadecane over Ni/H-ZSM-5 100 after 7 h reaction at 523 K).

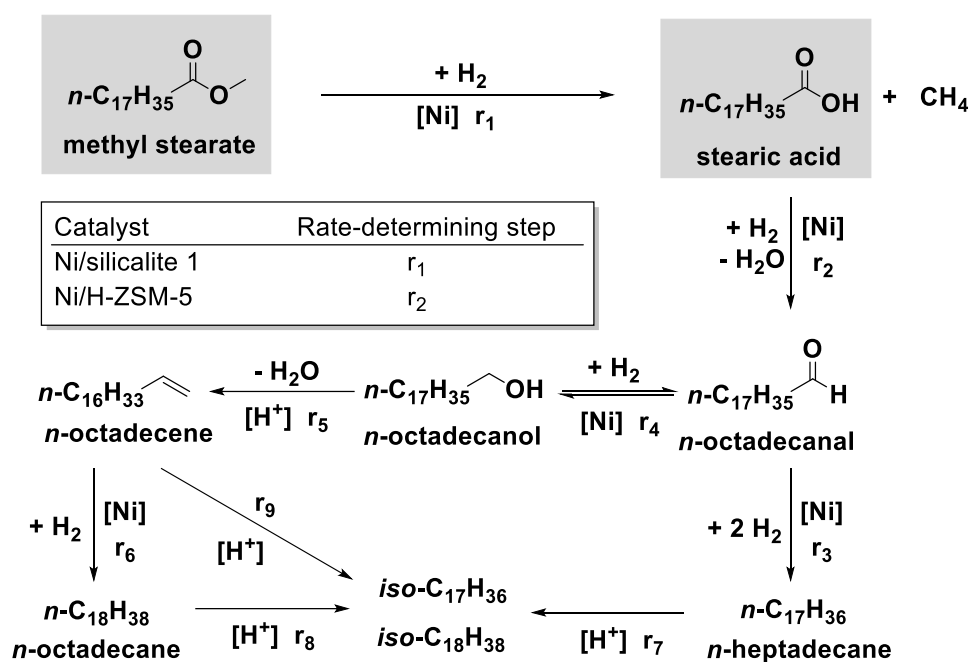


Figure 2. Reaction network for methyl stearate conversion.

Kinetic experiments of the C-O hydrogenolysis of stearic acid showed higher TOFs proportional to the increase of Brønsted acid site concentrations (Figure 3, Table 3). The increase of reaction rates of stearic acid conversion was less pronounced than for methyl stearate, showing that the synergy of Ni and Brønsted acid sites depends on the substrate (Figure 4). Thus, the shift of the rate-determining step from methyl stearate conversion (r_1) to stearic acid conversion (r_2) on Brønsted acidic catalysts is attributed to the stronger enhancement of r_1 rather than of r_2 .

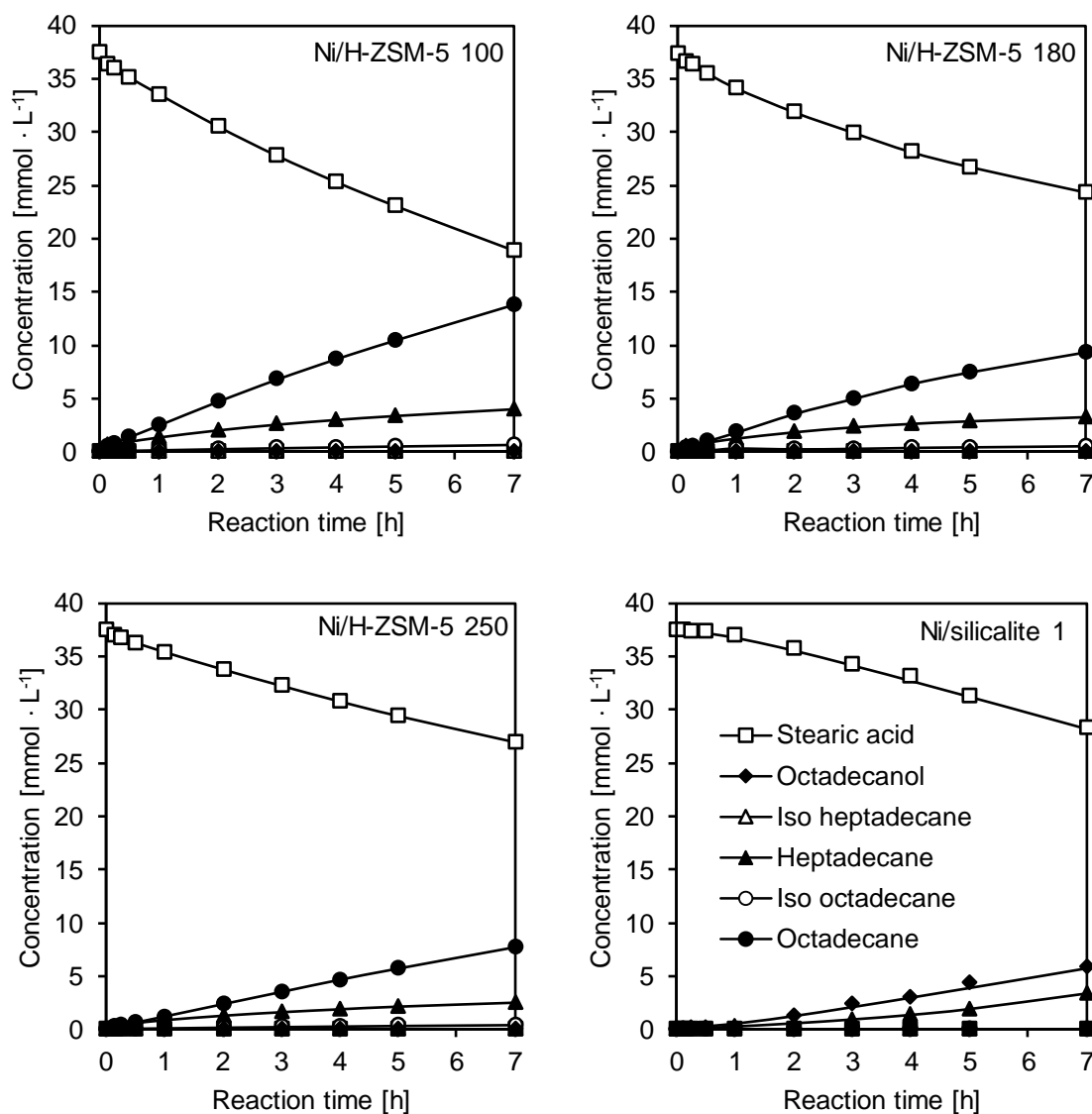


Figure 3. Concentration of stearic acid, reactions intermediates and products as a function of reaction time on catalysts with varying Si/Al ratio at 523 K.

Table 3. Reaction rates and TOFs of stearic acid conversion.

Sample	Initial rate [mmol _{Stearic acid} · (h · g _{Catalyst}) ⁻¹] ^a	Concentration of accessible Ni atoms [μmol _{accessible Ni} · g _{Catalyst} ⁻¹] ^b	Turn over frequency [mol _{Stearic acid} · (mol _{accessible Ni} · h) ⁻¹]
Ni/H-ZSM-5 100	7.1	105	68
Ni/H-ZSM-5 180	4.5	106	42
Ni/H-ZSM-5 250	3.6	100	36
Ni/silicalite-1	2.4	169	14

^a Kinetic results obtained at 523 K, 40 bar H₂.

^b Determined via AAS and H₂ chemisorption.

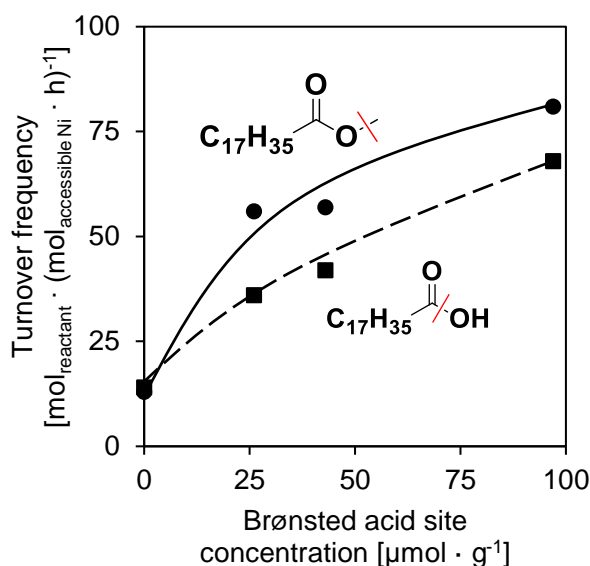


Figure 4. Turn over frequencies for methyl stearate and stearic acid conversion in dependence of the Brønsted acid site concentration of the support at 523 K.

3.4.2.3 Difference in activation energy of methyl stearate and stearic acid

Activation energies for stearic acid hydrogenolysis were higher than those of methyl stearate on all catalysts, which reflects the difference in bond dissociation energy of the bonds cleaved. That is, the bond dissociation energy (BDE) of the R₁C(O)-OH bond in fatty acids is higher than in alkyl esters R₁C(O)O-R₂ (BDE = 461.5 kJ · mol⁻¹ for CH₃C(O)-OH, BDE = 462.3 kJ · mol⁻¹ for CH₃CH₂C(O)-OH and BDE = 354 kJ · mol⁻¹ for CH₃CH₂C(O)-OCH₂CH₃²³). The apparent activation energy of methyl stearate on Ni/silicalite was 139 kJ · mol⁻¹. This is higher than the apparent activation energy of 107 kJ · mol⁻¹ reported on Pt/γ-Al₂O₃ (573 – 623 K, 6.9 bar, H₂, methyl stearate

dissolved in tetradecane²⁴). For the conversion of stearic acid over Ni/silicalite 1, the apparent activation energy of 198 kJ · mol⁻¹ is also higher than the apparent activation energy of 175 kJ · mol⁻¹ determined on 15 wt% Ni/γ-Al₂O₃ (533 – 563 K, 13 – 14.5 bar H₂ in n-dodecane)²⁵.

3.4.2.4 Influence of Brønsted acid sites on activation enthalpies and entropies of C-O hydrogenolysis of methyl stearate and stearic acid

The apparent activation energies decreased with increasing Brønsted acid site concentration of the catalysts from 139 kJ · mol⁻¹ to 109 kJ · mol⁻¹ for methyl stearate and from 198 kJ · mol⁻¹ to 127 kJ · mol⁻¹ for stearic acid (Figures S8 and 9). Interestingly, a stronger dependence on the concentration of Brønsted acid sites was observed for the apparent activation energy of the C-O hydrogenolysis of stearic acid than of methyl stearate (Figure 5). A similar correlation between reaction rates and Brønsted acidity was reported for the C-C hydrogenolysis of *neo*-pentane on supported Pd²². There, the effect was explained by Pd-protons adducts, which decrease the electron density of Pd resulting in highly active sites. In analogy, the electron density of the Ni particles of the catalysts studied are hypothesized to decrease with increasing concentration of Brønsted acid sites in the vicinity. However, XANES measurements did not show measurable shifts of the Ni K-edge energy nor a change in the intensity of the white line with varying Brønsted acid site concentrations of the support (Figure S7). Therefore, we conclude that a significant change in electron density of Ni particles was not induced by the presence of Brønsted acid sites²⁶.

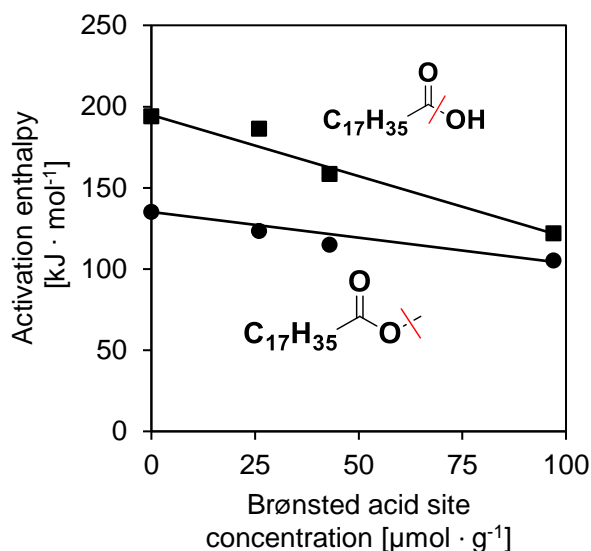


Figure 5. Apparent activation enthalpy as a function of the Brønsted acid site concentration of Ni catalysts supported on silicalite-1 and H-ZSM-5.

Table 4. Apparent activation energies, enthalpies and entropies for methyl stearate and stearic acid conversion over the catalysts with varying Brønsted acid site concentration.

Sample	Methyl stearate			Stearic acid		
	$E_{A, \text{app}}$ [$\text{kJ} \cdot \text{mol}^{-1}$]	$\Delta H_{\text{app}}^\ddagger$ [$\text{kJ} \cdot \text{mol}^{-1}$]	$\Delta S_{\text{app}}^\ddagger$ [$\text{J} \cdot (\text{mol} \cdot \text{K})^{-1}$]	$E_{A, \text{app}}$ [$\text{kJ} \cdot \text{mol}^{-1}$]	$\Delta H_{\text{app}}^\ddagger$ [$\text{kJ} \cdot \text{mol}^{-1}$]	$\Delta S_{\text{app}}^\ddagger$ [$\text{J} \cdot (\text{mol} \cdot \text{K})^{-1}$]
Ni/H-ZSM-5 100	109 ± 9	105 ± 9	-148 ± 18	127 ± 12	122 ± 12	-114 ± 28
Ni/H-ZSM-5 180	119 ± 12	115 ± 12	-132 ± 19	164 ± 5	159 ± 5	-47 ± 12
Ni/H-ZSM-5 250	128 ± 9	124 ± 9	-115 ± 16	189 ± 12	186 ± 12	4.79 ± 23
Ni/silicalite-1	139 ± 13	135 ± 13	-96.8 ± 24	198 ± 11	194 ± 11	12.3 ± 13

Brønsted acid sites at the perimeter of the metal particles have been concluded to increase hydrogenation rates by aiding the adsorption of hydrocarbons²⁷. That is, reaction rates increase with coverage of hydrocarbons on metal sites in the vicinity of Brønsted acid sites. However, the five-fold and six-fold increases in rates observed for

stearic acid and methyl stearate, respectively, would require equivalent increases in coverage. We regard those coverage increases as not likely for Ni particles with such little fraction of metal atoms at the interface with the support. That is, the concentration of surface Ni atoms is more than one order of magnitude higher than the concentration of Ni atoms at interface with the support. For instance, for a Ni particle with a diameter of 10 nm, the ratio of surface to interface atoms is 22 (calculations described in the SI).

We showed in a previous work that the reaction occurs outside the micropores of the support, as a similar increases in TOF for increasing Brønsted acid site concentration were observed for reactants that cannot access the micropores of similar catalysts³. We hypothesize, therefore, that Brønsted acid sites located at pore mouths in vicinity to metal particles facilitate catalysis for the C-O hydrogenolysis. In this scenario, the apparent activation enthalpies and entropies result from contributions of C-O hydrogenolysis over unpromoted Ni sites and over the Ni sites interacting with Brønsted sites. Therefore, with increasing Brønsted acid site concentration, the contribution of this second kind of sites to the measured TOF increases.

This postulate implies that the promoted Ni sites exist only at the support-metal interface. The low concentration of such sites must be compensated by a direct involvement in the reaction mechanism of C-O hydrogenolysis.

For the Brønsted acid sites to impact the enthalpy and entropy of the transition state they must interact with the polar moiety of the reactant, facilitating its conversion on the Ni particle. For methyl stearate and stearic acid weakening of the C-O bond is plausible upon protonation of the carbonyl group oxygen as shown in Figure 6. Methyl stearate is more readily protonated than stearic acid due to the proton affinities of methyl esters being higher (e.g., 830.2 kJ · mol⁻¹ for methyl propanoate) compared to carboxylic acids (e.g., 797.2 kJ · mol⁻¹ for propanoic acid)²⁸. For comparison, proton affinities of alcohols are comparable (e.g., 789.2 kJ · mol⁻¹ for butanol). As alcohol dehydration *via* acid-catalyzed protonation was observed under the applied conditions (octadecanol to octadecane *via* the readily hydrogenated intermediate octadecene), it is highly likely that protonated species of methyl stearate and stearic acid exist under the studied reaction conditions.

Hence, we propose that in the mechanism for C-O hydrogenolysis (Figure 6) the reactant is adsorbed on metal sites via the C and O of the C-O bond to be cleaved.

Protonation of the carbonyl O atom (and the concomitant positive charge) by a Brønsted acid site weakens the adsorbed C-O bond due to electron withdrawal and polarizes the bond. This facilitates the hydrogenolysis step upon nucleophilic addition of H adsorbed on the metal to the electrophilic C atom. This is reflected in the decreasing transition state enthalpy observed with increasing concentration of Brønsted acid sites. There is a compensation effect, i.e., the change in apparent transition state entropy becomes more negative as the enthalpy increases, which is rationalized by tighter transition states, when interacting with Brønsted acid sites (the degrees of freedom are reduced). After the C-O cleavage, stearic acid and methane are desorbed (in the case of methyl stearate as the reactant). The mechanism corresponding to the hydrogenolysis of stearic acid is presented in Figure S10.

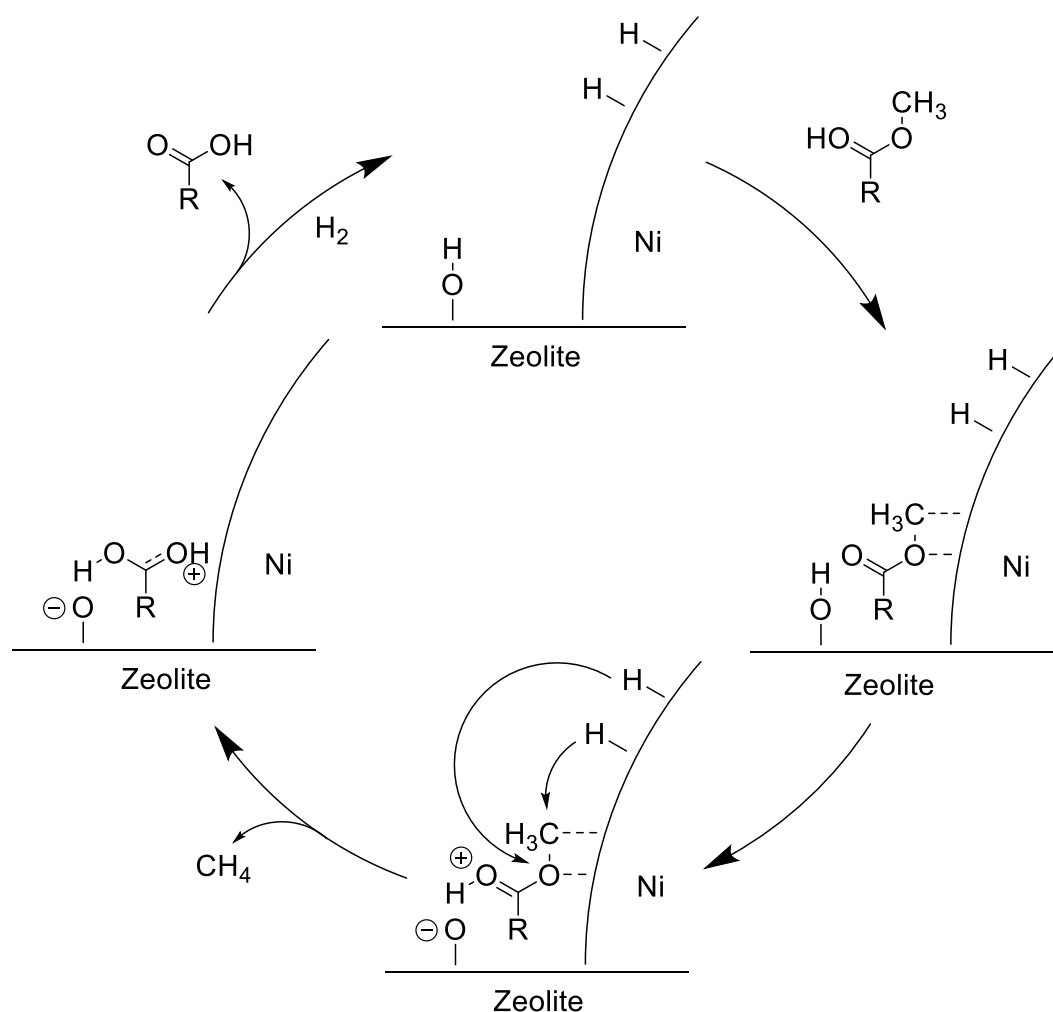


Figure 6. Proposed reaction mechanism for the C-O hydrogenolysis of methyl stearate over Ni facilitated by the protonation of the substrate by a Brønsted acid site.

3.5 Conclusion

The TOFs of C-O hydrogenolysis of methyl stearate and stearic acid on Ni increase proportionally to the concentration of Brønsted acid sites of the MFI supports. This is manifested by a decrease in the apparent enthalpy of the transition state on Ni sites close to Brønsted acid sites. The activation enthalpies for C-O hydrogenolysis of methyl stearate ($n\text{-C}_{17}\text{H}_{35}\text{C}(\text{O})\text{O-CH}_3$) are lower than those of stearic acid ($n\text{-C}_{17}\text{H}_{35}\text{C}(\text{O})\text{-OH}$), which reflects the difference in the corresponding bond energies. Thus, the TOFs increase to a larger extent with Brønsted acid site concentration for methyl stearate than for stearic acid. As the conversion takes place on Ni particles outside the micropores of the support and the electronic density of the metal does not depend on the support, it is concluded that the C-O hydrogenolysis is accelerated on highly active metal sites at the interface with the support. Ni and Brønsted acid sites are hypothesized to act cooperatively, i.e., Brønsted acid sites protonate the basic oxygen of the carbonyl group, decreasing the strength of the C-O bond. This facilitates its Ni catalyzed C-O bond cleavage due to the concomitant reduction of the enthalpy of the transition state.

3.6 Acknowledgements

The authors thank Andreas Ehrmaier, Marco Peroni, and Marianne Hanzlik for TEM measurements, Martin Neukamm for AAS and SEM measurements and Xaver Hecht for chemisorption and physisorption measurements. Financial support for M.W.S. in the framework of the AlgenFlugKraft project (FKZ LaBay74) of the Bavarian Ministry of Economic Affairs and Media, Energy and Technology (“Bayerisches Staatsministerium für Wirtschaft und Medien, Energie und Technologie”) and of the Bavarian State Ministry of Education, Science and the Arts (“Bayerisches Staatsministerium für Bildung und Kultus, Wissenschaft und Kunst”) is highly appreciated. The XANES experiments were performed at CLAES beamline at ALBA Synchrotron with the collaboration of ALBA staff. J.A.L. and O.Y.G. acknowledge support for their contribution by the U.S. Department of Energy (DOE), Office of Science, Office of Basic Energy Sciences, Division of Chemical Sciences, Geosciences and Biosciences.

3.7 Literature

1. Zhao, C.; Bruck, T.; Lercher, J. A., Catalytic deoxygenation of microalgae oil to green hydrocarbons. *Green Chemistry* **2013**, *15* (7), 1720-1739.
2. De, S.; Zhang, J.; Luque, R.; Yan, N., Ni-based bimetallic heterogeneous catalysts for energy and environmental applications. *Energy & Environmental Science* **2016**, *9* (11), 3314-3347.
3. Schreiber, M. W.; Rodriguez-Nino, D.; Gutierrez, O. Y.; Lercher, J. A., Hydrodeoxygenation of fatty acid esters catalyzed by Ni on nano-sized MFI type zeolites. *Catalysis Science & Technology* **2016**, *6* (22), 7976-7984.
4. Peng, B.; Yao, Y.; Zhao, C.; Lercher, J. A., Towards Quantitative Conversion of Microalgae Oil to Diesel-Range Alkanes with Bifunctional Catalysts. *Angew. Chem. Int. Ed.* **2012**, *51* (9), 2072-2075.
5. Zuo, H.; Liu, Q.; Wang, T.; Ma, L.; Zhang, Q.; Zhang, Q., Hydrodeoxygenation of Methyl Palmitate over Supported Ni Catalysts for Diesel-like Fuel Production. *Energy & Fuels* **2012**, *26* (6), 3747-3755.
6. Chen, L.; Fu, J.; Yang, L.; Chen, Z.; Yuan, Z.; Lv, P., Catalytic Hydrotreatment of Fatty Acid Methyl Esters to Diesel-like Alkanes Over H β Zeolite-supported Nickel Catalysts. *ChemCatChem* **2014**, *6* (12), 3482-3492.
7. Larsen, G.; Haller, G. L., Metal-support effects in Pt/L-zeolite catalysts. *Catalysis Letters* **1989**, *3* (1), 103-110.
8. de Mallmann, A.; Barthomeuf, D., *J. Chim. Phys. Phys.-Chim. Biol.* **1990**, *87*, 535.
9. Zhang, Z.; Wong, T. T.; Sachtler, W. M. H., The effect of Ca²⁺ and Mg²⁺ ions on the formation of electron-deficient palladium-proton adducts in zeolite Y. *Journal of Catalysis* **1991**, *128* (1), 13-22.
10. Dossi, C.; Psaro, R.; Ugo, R.; Zhang, Z. C.; Sachtler, W. M. H., Non-acidic Pd/Y Zeolite Catalysts from Organopalladium Precursors: Preparation and Catalytic Activity in MCP Reforming. *Journal of Catalysis* **1994**, *149* (1), 92-99.
11. Menacherry, P. V.; Haller, G. L., Electronic effects and effects of particle morphology in n-hexane conversion over zeolite-supported platinum catalysts. *Journal of Catalysis* **1998**, *177* (2), 175-188.
12. Song, W.; Liu, Y.; Barath, E.; Zhao, C.; Lercher, J. A., Synergistic effects of Ni and acid sites for hydrogenation and C-O bond cleavage of substituted phenols. *Green Chemistry* **2015**, *17* (2), 1204-1218.
13. Gosselink, R. W.; Hollak, S. A. W.; Chang, S.-W.; van Haveren, J.; de Jong, K. P.; Bitter, J. H.; van Es, D. S., Reaction Pathways for the Deoxygenation of Vegetable Oils and Related Model Compounds. *ChemSusChem* **2013**, *6* (9), 1576-1594.
14. Nares, R.; Ramírez, J.; Gutiérrez-Alejandre, A.; Louis, C.; Klimova, T., *J. Phys. Chem. B* **2002**, *106* (51), 13287-13293.
15. Gurvich, L. J., *Phys Chem Russ* **1915** (47), 805.
16. Barrett, E. P.; Joyner, L. G.; Halenda, P. P., *J. Am. Chem. Soc.* **1951**, (73), 373-380.
17. Lippens, B. C.; de Boer, J. H., *J. Catal.* **1965**, *4* (319).
18. Corma, A.; Fornes, V.; Forni, L.; Marquez, F.; Martinez-Triguero, J.; Moscotti, D., *J. Catal.* **1998**, *179*, 451-458.
19. Burattin, P.; Che, M.; Louis, C., *J. Phys. Chem. B* **1998**, *102*, 2722.
20. Cejka, J.; van Bekkum, H.; Corma, A.; Schueth, F., *Introduction to Zeolite Molecular Sieves*. Elsevier: Amsterdam, 2007.
21. Zhang, X.; Liu, D.; Xu, D.; Asahina, S.; Cychosz, K. A.; Agrawal, K. V.; Al Wahedi, Y.; Bhan, A.; Al Hashimi, S.; Terasaki, O.; Thommes, M.; Tsapatsis, M.,

Synthesis of self-pillared zeolite nanosheets by repetitive branching. *Science* **2012**, 336 (6089), 1684-7.

22. Homeyer, S. T.; Karpiński, Z.; Sachtler, W. M. H., Effect of zeolite protons on palladium-catalyzed hydrocarbon reactions. *Journal of Catalysis* **1990**, 123 (1), 60-73.

23. Luo, Y.-R., *Handbook of Bond Dissociation Energies in Organic Compounds*. CRC Press: 2003.

24. Chiappero, P. T. D., M.; Iobban, L. L.; Resasco, D. E., *Catal. Lett.* 2009, p 9.

25. Kumar, P.; Yenumala, S. R.; Maity, S. K.; Shee, D., *Appl. Catal. A: General* 2014, p 28.

26. Ichikuni, N.; Iwasawa, Y., In situ d electron density of Pt particles on supports by XANES. *Catalysis Letters* **1993**, 20 (1), 87-95.

27. Yu, Y.; Fonfé, B.; Jentys, A.; Haller, G. L.; Rob van Veen, J. A.; Gutiérrez, O. Y.; Lercher, J. A., Bimetallic Pt–Pd/silica–alumina hydrotreating catalysts. Part II: Structure–activity correlations in the hydrogenation of tetralin in the presence of dibenzothiophene and quinoline. *Journal of Catalysis* **2012**, 292, 13-25.

28. Hunter, E. P.; Lias, S. G., Evaluated Gas Phase Basicities and Proton Affinities of Molecules: An Update. *J. Phys. Chem. Ref. Data* **1998**, 3 (27), 413 - 656.

3.8 Associated Content

3.8.1 Additional Information

See supporting information.

3.8.2 Notes and Author Contributions

Moritz W. Schreiber planned, performed and evaluated synthesis, characterization and kinetic experiments. Results were discussed with Oliver Y. Gutiérrez and Johannes A. Lercher. Moritz W. Schreiber drafted the manuscript. Oliver Y. Gutiérrez, Eszter Bárath and Johannes A. Lercher revised the manuscript.

4 Lewis-Brønsted acid pairs in Ga/H-ZSM-5 to catalyze dehydrogenation of light alkanes

4.1 Abstract

The active sites for propane dehydrogenation in Ga/H-ZSM-5 with moderate concentrations of tetrahedral aluminum in the lattice were identified to be Lewis-Brønsted acid pairs. With increasing availability, Ga⁺ and Brønsted acid site concentrations changed inversely, as protons of Brønsted acid sites were exchanged with Ga⁺. At a Ga/Al ratio of 0.5, the rate of propane dehydrogenation was two orders of magnitude higher than with the parent HZSM-5, highlighting the extraordinary properties of the Lewis-Brønsted acid pairs. Density functional theory calculations relate the high activity to a bifunctional mechanism that helps catalyzing a heterolytic activation of the propane C-H bond.

4.2 Introduction

The increasing availability of propane from shale gas together with the worldwide increase in propene demand has spurred interest in on-purpose production of propene *via* dehydrogenation.¹ While being catalyzed with higher energy of activation compared to monomolecular cracking,²⁻³ dehydrogenation is also catalyzed by Brønsted acids via hydronium ions²⁻⁶ as well as by Lewis acid sites, such as Ga, Zn, La. Especially, the combination of Brønsted and Lewis acids in the zeolite micropore channels was observed to be active for propane dehydrogenation.⁷⁻⁹ Gallium modified H-ZSM-5 has been used commercially for the aromatization of light alkanes¹⁰. However, the nature of active sites in these Ga exchanged zeolites catalysts and the mechanism of dehydrogenation is still discussed controversially.^{7, 9, 11-16} While the present contribution will not address comprehensively the aspects to resolve all open points, a homotopic catalyst with unprecedented activity for dehydrogenation is reported.

Under reductive atmosphere and high temperature, monovalent Ga⁺ cations can be formed and exchanged for the protons of zeolite Brønsted acid sites.¹¹⁻¹² However, besides Ga⁺, other cations such as [GaH₂]⁺, [GaO]⁺, [HGaOH]⁺ as well as Ga₂O₃ appear to exist as active sites for propane dehydrogenation.^{7, 9, 11-14} A synergistic interaction between Lewis acidic Ga species and Brønsted acid SiOHAl sites has been indirectly reported, as catalysts containing both exhibit a rate of propane dehydrogenation, which is higher than the additive contributions of Ga and Brønsted acid sites.^{7, 9, 15-16} The atomistic nature of these sites has not been unequivocally resolved.

In principle, two mechanisms have been proposed for the dehydrogenation of propane on Ga and H-ZSM-5. According to the first mechanism, alkanes are dehydrogenated *via* carbonium ion intermediates or transition states at the Brønsted acid sites and the Lewis acidic Ga species facilitates the recombinative desorption of H₂.⁹ Alternatively, the alkane C-H bond has been proposed to be polarized on Ga₂O₃, facilitating the formation of carbonium ions on Brønsted acid sites.¹⁶ According to the other mechanism, the dehydrogenation proceeds *via* an initial abstraction of a hydride by a Ga cation⁷ or by Ga₂O₃¹⁵ generating transiently a carbenium ion. The abstracted H⁻ and H⁺ of the Brønsted acid site recombine, forming H₂ and an alkoxy group.

In order to resolve these discrepancies, the synergy of Lewis-Brønsted acid pairs in a series of well-defined GaH-ZSM-5 zeolite was examined for the dehydrogenation of

propane and butane. The nature and concentration of the active site were determined *in situ via* X-ray absorption spectroscopy (XANES), temperature programmed reduction (TPR) and infrared (IR) spectroscopy of adsorbed pyridine. The nature and stoichiometry of the sites required for the synergetic interaction of Ga and Brønsted acid sites was elucidated and a mechanism for the dehydrogenation is proposed, supported by physicochemical characterization, kinetic experiments and DFT (Density functional theory) calculations.

4.3 Experimental

4.3.1 Synthesis

NH₄-ZSM-5 provided by Clariant (MFI-100 EX 1716.00 H1-C) with a Si/Al = 50 was suspended in an aqueous solution of ammonium hexafluorosilicate (AHFS, 4-fold excess with respect to the Al content of the sample) and heated to 353 K under vigorous stirring for 5 h. Subsequently the zeolite was washed six times with hot (353 K), deionized water. This procedure was repeated three times. Afterwards, the zeolite was dried at 373 K and converted into the protonic form by calcination in a stream of synthetic air (100 mL/min, 5h, 10 K/min). Silica (Aerosil 200, Evonik) was used as non-acidic support for comparison. The AHFS treated zeolite was loaded with Ga *via* incipient wetness impregnation by an aqueous Ga(NO₃)₃ solution (Ga(NO₃)₃, Sigma, Aldrich, purity < 99%). After drying under static conditions (10 h, 373 K), the catalysts were calcined in a stream of synthetic air (100 mL/min, 4h, 873 K, 2 K/min). The samples are denoted as H-ZSM-5, Ga₂O₃/SiO₂ and X/Y Ga/Al Ga/H-ZSM-5 according to their Ga/Al ratio.

4.3.2 Catalytic experiments

Catalytic reactions were performed in a fixed bed plug flow reactor, consisting of a quartz glass coated stainless steel reactor. The catalyst bed typically contained 4 mg of catalyst with a particle size range of 160 - 280 μm diluted in 200 mg silicon carbide in order to ensure isothermal reaction conditions. Before the reaction, the pre-calcined catalysts were reduced in H₂ (50 mL/min, 1h, 873 K, 15 K/min). Subsequently, the samples were purged with N₂ (15 mL/min, 10 min) at 823 K and the reactions were carried out at 1 bar total pressure with N₂ as an inert diluent. The apparent activation enthalpies and entropies were determined in the temperature range of 783 K - 823 K

for propane and in the range of 763 K – 803 K for butane with a hydrocarbon partial pressure of 8.75 mbar and a total flow rate of 100 mL · min⁻¹. Determination of reaction orders were carried out at hydrocarbon partial pressures ranging from 0.25 – 45 mbar at 783 K and a total flow rate of 100 mL · min⁻¹. An Agilent 6890 Series GC-FID system equipped with an *Agilent Technologies HP - PLOT/Q* column (30m x 0.320mm) and a FID was used for product analysis. The mass balance was better than 99 % in all experiments.

Reaction rate constants were determined under differential conversions ($x < 3.2$ %). The overall reaction rates were determined based on the fraction of converted reactants (propane or n-butane). Cracking and dehydrogenation rates were determined for propane from the yields using methane and ethane for cracking and propene for dehydrogenation. For n-butane methane and propene, ethane and ethane were used to determine the rates for cracking and cis-2-butene, trans-2-butene, 1-butene and iso-butene for the rate of dehydrogenation. Bimolecular and secondary reactions were avoided by studying the system at low conversion levels. This was confirmed by the formation of equimolar ratios (1.0 ± 0.1) of cracking products (C_2H_4/CH_4 for C_3H_8 and C_3H_6/CH_4 for C_4H_{10}), while products heavier than the reactants were absent. Deactivation was below 5 % during catalytic experiments. All reaction rates and rate constants were normalized to the mass of catalyst. Site specific turnover frequencies were calculated based on catalysts containing only one type of site by normalizing the reaction rate constant to the concentration of the respective active site. Apparent activation enthalpies and entropies were calculated based on the Eyring Polanyi equation:

$$k = \frac{k_B \cdot T}{h} \cdot e^{-\frac{\Delta G^{\ddagger}}{R \cdot T}}$$

with the reaction rate constant k normalized per site and to one bar taking into account the respective reaction order, the absolute temperature T , the gas constant R , the Boltzmann constant k_B , the Planck's constant h and the Gibbs energy of activation ΔG^{\ddagger} . The equation was extended *via* the Gibbs-Helmholtz equation to the following form:

$$k = \frac{k_B \cdot T}{h} \cdot e^{\frac{\Delta S^{\ddagger}_{app.}}{R}} \cdot e^{-\frac{\Delta H^{\ddagger}_{app.}}{R \cdot T}}$$

with the apparent activation enthalpy $\Delta H_{\text{app}}^{\ddagger}$ and apparent activation entropy $\Delta S_{\text{app}}^{\circ\ddagger}$ the equation can be rearranged to its linear form:

$$\ln \frac{k}{T} = \frac{\Delta H^{\circ\ddagger}}{R} \cdot \frac{1}{T} + \ln \frac{k_B}{h} + \frac{\Delta S^{\circ\ddagger}}{R}$$

This form was used for the representation of the results in Eyring plots and the determination of apparent activation enthalpies and entropies as well as their standard deviations.

4.3.3 Characterization

The composition of the samples was determined by inductively coupled plasma - optical emission spectrometry (ICP-OES) on a *700 Series ICP-OES* by Agilent Technologies. The Ga/Al ratios set during the synthesis were archived with a deviation of $\pm 5\%$ (Table S1)

Concentration and strength of Lewis and Brønsted acid sites (LAS and BAS, respectively) were determined by infrared spectroscopy of adsorbed pyridine using a Bruker VERTEX 70 IR spectrometer. Self-supporting wafers of the samples were reduced (1h, 873 K, 15 K/min) in a stream of H₂ (20 mL/min) and outgassed (1h, 873 K, 10⁻⁶ mbar). The reduction conditions were identical with those before kinetic measurements in the plug flow reactor. Pyridine was adsorbed on the samples at an equilibrium pressure of 10⁻¹ mbar (0.5 h, 423 K). Concentrations of Lewis and Brønsted acid sites were determined via quantifications of the bands related to coordinatively adsorbed pyridine (1446 cm⁻¹ and 1455 cm⁻¹) and protonated pyridine (1545 cm⁻¹), respectively, using molar extinction coefficients of 3.26 and 4.32 $\mu\text{mol} \cdot \text{cm}^{-2}$. Deconvolution of the two bands of coordinatively adsorbed pyridine was done *via* two Gaussian functions centered at 1446 cm⁻¹ and 1455 cm⁻¹.

Magic-angle spinning nuclear magnetic resonance measurements of ²⁷Al were carried out on a Bruker Avance AMX-500 spectrometer. Samples were packed into ZrO₂ rotors after hydration (48 h) at 42 mbar H₂O. The spinning rate was 10 kHz. Al(NO₃)₃ · 9H₂O was used as a reference. Spectra of parent H-ZSM-5 and Ga modified H-ZSM-5 showed no signal of octahedrally coordinated Al (0 ppm) (Figure S1).

The X-ray absorption near-edge structure (XANES) at the Ga K edge (10368.3 eV) was measured at the Alba Light Source in Barcelona, Spain on beamline BL22 – CLAESS. Spectra were recorded in fluorescence mode at ambient temperature for

references and during in situ reduction, purging and reaction at intervals of ca. 8 min for the catalysts. The spectra were normalized to an edge step height of one and the energy calibrated using metallic Ga (10368.3 eV).¹⁷ Edge energies were determined at the inflection points of the Ga K edges. The samples were packed in capillary reactors with 1 mm outer diameter and 0.02 mm wall thickness. The catalysts were reduced (1h, 873 K, 15 K/min) in a stream of H₂ (5 mL/min) and purged with helium (5 mL/min) at 873 K for 0.5 h before the reaction was carried out at 873 K with 5 mL/min 5 vol% propane in He. Subsequently, the catalysts were cooled to ambient temperature in a stream of H₂ (5 mL/min). Metallic Ga, Ga³⁺ in the form of Ga₂O₃, GaCl₃ and Ga⁺ in the form of Ga(I)Ga(III)Cl₄ (commercially available as GaCl₂) were used as references. The contribution of Ga(I) was extracted from the spectra of Ga(I)Ga(III)Cl₄ by subtracting the spectra of isostructural K(I)Ga(III)Cl₄ from Ga(I)Ga(III)Cl₄. K(I)Ga(III)Cl₄ was synthesized by mixing stoichiometric amounts of KCl and GaCl₃, sealing it into a capillary inside a nitrogen atmosphere (Glovebox) and treating it at 573 K for 3h.

4.3.3.1 Stoichiometry analysis of temperature programmed reduction

Consumption of H₂ and formation of H₂O during reduction of the samples were quantified via a Pfeiffer Vacuum Prisma QME 200 mass spectrometer. A quartz reactor tube was packed with 600 mg or 7.2 mg (90 μmol) of Ga/H-ZSM-5. The samples were calcined (2h, 873 K) in a stream of 20 vol% O₂ in He (5 mL/min) and purged in a stream of He (5 mL/min, 1h, 873 K) in order to exclude water formation by reaction of H₂ with O₂ adsorbed on the catalyst. Subsequently, reduction was carried out via pulses of 0.69 mL (27.75 μmol) H₂ diluted in He (41 vol% H₂ in He) introduced into a constant stream of He (5 mL/min) at intervals of 0.25 h at 873 K. For each sample 40 pulses were recorded. Calibration of the H₂ signal was done via the known amount of H₂ per pulse and corresponding area of unreacted H₂ signal after the reduction. The reduction of CuO in H₂ was used for calibration of the H₂O signal.

4.3.3.2 Density functional theory calculations

Density functional theory calculations were carried out using the Vienna Ab-initio Simulation Package (VASP)¹⁸ using a periodic model of MFI with a triclinic unit cell having the experimentally determined dimensions of 20.02 Å × 19.90 Å × 13.38 Å. The

RPBE functional¹⁹ was used to describe exchange and correlation and the DFT-D2 method of Grimme et al.²⁰ was used to include semi-empirical dispersion interactions. The Kohn-Sham orbitals were constructed in a plane wave basis with an energy cutoff of 400 eV and were described in the core regions using the projector-augmented wave method.²¹ The Kohn-Sham orbitals were only calculated at the Γ -point and their occupancies were determined using the Gaussian smearing method with $\sigma = 0.02$ eV. Electronic structure minimization was performed using the RMM-DIIS algorithm until the change in total energy fell below 10^{-4} eV. Geometry optimization on local-minimum structures was carried out until the forces on all atoms were below 0.05 eV/Å.

Transition state structures were determined using the nudged elastic band method (NEB)²² with 8 or 16 images, depending on the complexity of the reaction trajectory, and a force convergence criterion of 0.3 eV/Å for each image. The maximum-energy structure was then interpolated along the NEB trajectory and used to generate the starting structure and reaction coordinate to refine the transition state with the dimer method²³ until the forces on all atoms fell below 0.05 eV/Å.

The harmonic vibrational frequencies were determined for each structure using a limited set of atoms in the unit cell that consists of all of the non-framework atoms and 9 framework atoms. It was confirmed that all of the local-minimum structures had real frequencies and the transition state structures had a single imaginary frequency. The frequencies were used to calculate the vibrational contribution to the free energy in the harmonic approximation for each structure at 783 K. For the gas phase species propane, propene, and H₂, the translational and rotational contributions to the free energy were also computed in the ideal gas approximation at 783 K and partial pressures of 10, 0.1, and 0.1 mbar, respectively. Apparent activation enthalpies and free energies were calculated using the enthalpies and free energies of the transition state structures relative to the initial state of the active site and gas phase propane.

4.4 Results and discussion

4.4.1 Influence of the Ga concentration on the reaction kinetics

Ga/H-ZSM-5 catalysts with Ga/Al ratios in the range of 1/9 to 3/2 were studied in order to investigate the influence of the Ga/Al ratio on the reaction kinetics in propane dehydrogenation. A strong influence of the reaction rate on the Ga/Al ratio was

observed, with a maximum in propane conversion at a Ga/Al ratio of 1/2 (Figure 1, Table S2). The maximum reaction rate on Ga/H-ZSM-5 (for Ga/Al = 0.5) was two orders of magnitude higher than for H-ZSM-5 (0.011 and $1.6 \cdot 10^{-6} \cdot \text{mol} \cdot (\text{g} \cdot \text{s})^{-1}$, 783 K), which is substantially higher than those reported previously.⁷ The higher rate enhancement observed is attributed to highly ordered structure in the present case compared to similar studies in the literature.

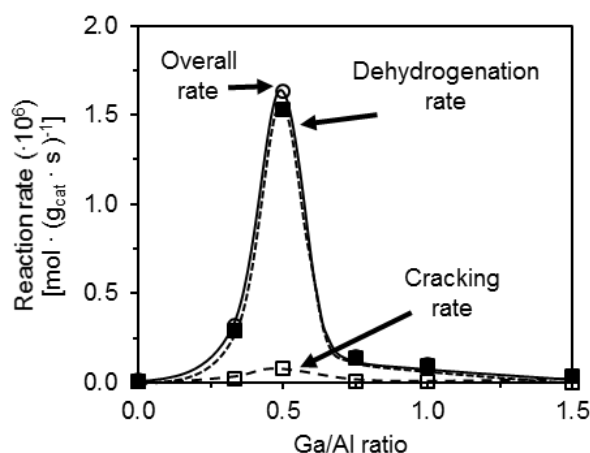


Figure 1. Overall, protolytic cracking and dehydrogenation rate as a function of Ga/Al ratio of the catalysts (Reaction temperature 783 K, propane partial pressure 8.75 mbar).

The contributions of protolytic cracking and dehydrogenation to the overall rate are shown in (Figure 1). The reaction rates of cracking and dehydrogenation on parent H-ZSM-5 match with the values reported in literature.^{2, 4, 6} The reaction rate of dehydrogenation follows the same trend as the total rate, with a maximum in reaction rate at a Ga/Al ratio of 0.5, increasing its selectivity from 22 % (H-ZSM-5) to 89% ($\frac{1}{2}$ Ga/Al Ga/H-ZSM-5) at conversions less than 3.2%. The dehydrogenation rate is increased by more than two orders of magnitude (350) with the best Ga modified H-ZSM-5 compared to the parent H-ZSM-5 (0.0044 and $1.5 \cdot 10^{-6} \cdot \text{mol} \cdot (\text{g} \cdot \text{s})^{-1}$, 783 K). Protolytic cracking followed a similar trend as dehydrogenation, reaching a maximum at Ga/Al ratio of 0.5, with very little or no protolytic cracking being observed for Ga/Al ≥ 1 , decreasing its selectivity from 35% (H-ZSM-5) to less than 3%. The decline in the protolytic cracking rate is in line with the decrease in the BAS concentration as the Ga/Al ratio decreased. The reaction rate ratio of dehydrogenation/cracking on H-ZSM-5 was 0.63 (783 K), while on $\frac{1}{2}$ Ga/Al the ratio was 19 (783 K), highlighting the increase

of the dehydrogenation over the cracking rate on Ga modified H-ZSM-5 compared to parent H-ZSM-5. To compare the marked contribution of the Ga species, a Ga₂O₃/SiO₂ catalyst was studied, which showed only activity for dehydrogenation ($0.13 \cdot 10^{-7} \cdot \text{mol} \cdot (\text{g} \cdot \text{s})^{-1}$, 783 K), while protolytic cracking was not observed.

Comparable differences in the rates were observed for the dehydrogenation of butane between the most active catalyst (Ga/Al ratio of 0.5 on parent H-ZSM-5) and the parent H-ZSM-5. The dehydrogenation rate at 783 K increased by a factor of 21 on $\frac{1}{2}$ Ga/Al compared to H-ZSM-5 for butane (0.38 and $0.018 \cdot 10^{-6} \cdot \text{mol} \cdot (\text{g} \cdot \text{s})^{-1}$, 783 K). Note that these rates of butane dehydrogenation on the parent H-ZSM-5 are in line with prior results in literature.^{5, 24}

Table 1. Reaction rates of propane dehydrogenation and cracking on Ga modified zeolitic and oxidic materials at 783 K (Rates $\times 10^7$ [$\text{mol} \cdot (\text{g} \cdot \text{s})^{-1}$]). The following abbreviations have been made: Overall (Over.), Dehydrogenation (Dehy.), Cracking (Crack.) and Dehydrogenation/Cracking (D/C).

Catalyst	Overall	Cracking	Dehydrogenation	D/C
H-ZSM-5	0.11	0.07	0.04	0.63
1/3 Ga/Al	3.18	0.23	2.95	12.0
1/2 Ga/Al	15.91	0.79	15.12	19.2
3/4 Ga/Al	1.46	0.08	1.38	17.2
1 Ga/Al	0.99	0.04	0.95	21.9
3/2 Ga/Al	0.38	0.01	0.37	27.7
Ga ₂ /SiO ₂	0.13	-	0.13	-

In order to study the influence of the Ga/Al ratio on the contribution of active sites to rate of dehydrogenation the reaction rate had to be separated into contributions of Ga sites and BAS catalyzed reactions, requiring the quantification of the proposed active sites as well as the determination of their atomistic structure.

Table 2. Reaction rates of alkane dehydrogenation and cracking on Brønsted acid and Lewis Brønsted acid pairs 783 K (Rates $\times 10^7$ [mol \cdot (g \cdot s) $^{-1}$]). The following abbreviations have been made: Overall (Over.), Dehydrogenation (Dehyd.), Cracking (Crack.) and Dehydrogenation/Cracking (D/C).

Alkane	H-ZSM-5				1/2 Ga/Al Ga/H-ZSM-5			
	Over.	Dehyd.	Crack.	D/C	Over.	Dehyd.	Crack.	D/C
Propane	0.11	0.044	0.070	0.63	15.9	15.1	0.79	19.2
n-Butane	0.82	0.175	0.65	0.27	4.76	3.67	1.09	3.41

4.4.2 Nature and concentration of active sites

The concentration of acid sites was determined by IR spectra of adsorbed pyridine after reduction in H₂. In situ reduction was critical, as a fast oxidation of cationic Ga species was observed upon contact with traces of water (e.g., in ambient air), reestablishing protons on BAS and Ga_xO_y clusters under formation of molecular H₂ (Figure S2). In line with these observations, the Brønsted acid site concentration decreased only to a small extent for Ga/H-ZSM-5 catalysts without in situ reduction; with 1/2 Ga/Al-ZSM-5 20% of the BAS were converted to LAS, for 3/2 Ga/Al the fraction increase to 25%.

The presence of three different types of acid sites was shown by IR spectroscopy of adsorbed pyridine. One type of Brønsted acid sites and two types of Lewis acid sites with bands at 1555 cm⁻¹ (protonated pyridinium ion, BAS) as well as 1457 cm⁻¹ and 1446 cm⁻¹ (coordinatively adsorbed pyridine, Ga⁺ and Ga_xO_y) respectively, were distinguished (Figure S3). It should be noted in passing that the 1455 cm⁻¹ band of coordinative adsorbed pyridine corresponds to strong LAS (such as highly accessible Al³⁺, Ga³⁺ or Ga⁺ sites), while the band at 1446 cm⁻¹ is characteristic of weak or sterically shielded LAS.

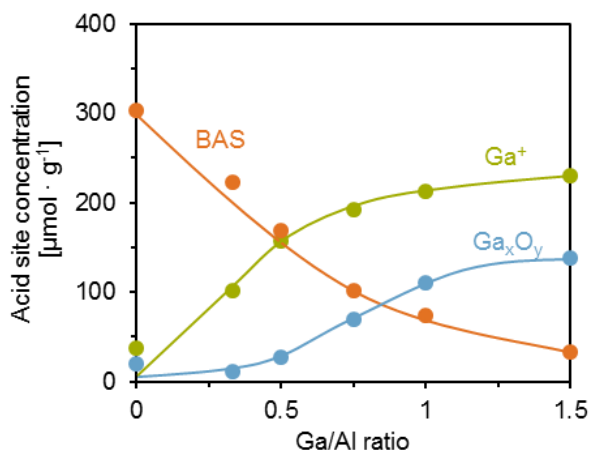


Figure 2. Concentrations of Lewis and Brønsted acid sites of catalysts as a function of the Ga/Al ratio.

The Brønsted acid site concentration after in situ reduction decreased linearly with increasing Ga concentration (Figure 2). The direct compensation of the decrease in the concentration of BAS by Ga sites (for catalysts with $\text{Ga/Al} \leq 1$) strongly suggests the exchange of the protons of the SiOHAl groups by a monovalent cationic Ga^+ species with a stoichiometry of $\text{Ga:H}^+ = 1:1$. The decrease in Brønsted acid site concentration, measured by adsorbed pyridine, agrees well with the decrease of the O-H stretching vibration of the Brønsted acid sites (3616 cm^{-1}). For Ga/Al ratios > 0.5 a second Ga species was observed, which does not substitute for protons of BAS. The lower wavenumber of this LAS (1446 cm^{-1}) points to a site that acts as considerably weaker LAS towards pyridine. As the total concentration of acid sites did not linearly increase with the Ga loading for samples with Ga/Al ratios > 0.5 , the formation of Ga_xO_y clusters in which not all Ga atoms are accessible for pyridine is hypothesized.

The oxidation state of the cationic Ga species was studied by X-ray absorption spectroscopy (Figure 3). During in situ reduction (temperature raised from 293 to 873K in H_2 flow) of unreduced $\frac{1}{2}\text{Ga/Al}$ the Ga K-edge shifted from 10374.3 eV to 10370.2 eV (Figure 3). To assign these shifts to the oxidation state, Ga(III)Cl_3 and Ga(I)Ga(III)Cl_4 were used as references for Ga^{+3} (10373.5 eV) and Ga^+ (10369.9 eV) species. Thus, these changes observed in the XANES during in situ reduction suggest a change in the oxidation state of Ga. However, a distinction between Ga^+ and specially coordinated Ga^{3+} such as $[\text{GaH}_2]^+$ needs to be taken into account, as charge donation of H_2 to Ga^{+3} would lead to an electronic structure similar to Ga^+ ¹⁴. Therefore, the XANES cannot discern unequivocally between Ga^+ and $[\text{GaH}_2]^{+1}$ ¹⁴ and further analysis

of this site is discussed below. For the Ga₂O₃/SiO₂ catalysts the edge did not change significantly during in situ reduction (Figure S4), indicating that the majority of Ga₂O₃ was not reduced on SiO₂. These findings agree well with the results from IR spectra of adsorbed pyridine, suggesting the existence of two Ga species. We hypothesize that the Ga giving rise to the white line peak at 10370.2 eV is related to a strong LAS, presumably Ga⁺ substituting the H⁺ of the bridging hydroxyl group. In consequence, the white line at 10374.3 eV is attributed to Ga³⁺ in a more aggregated environment as Ga_xO_y clusters.

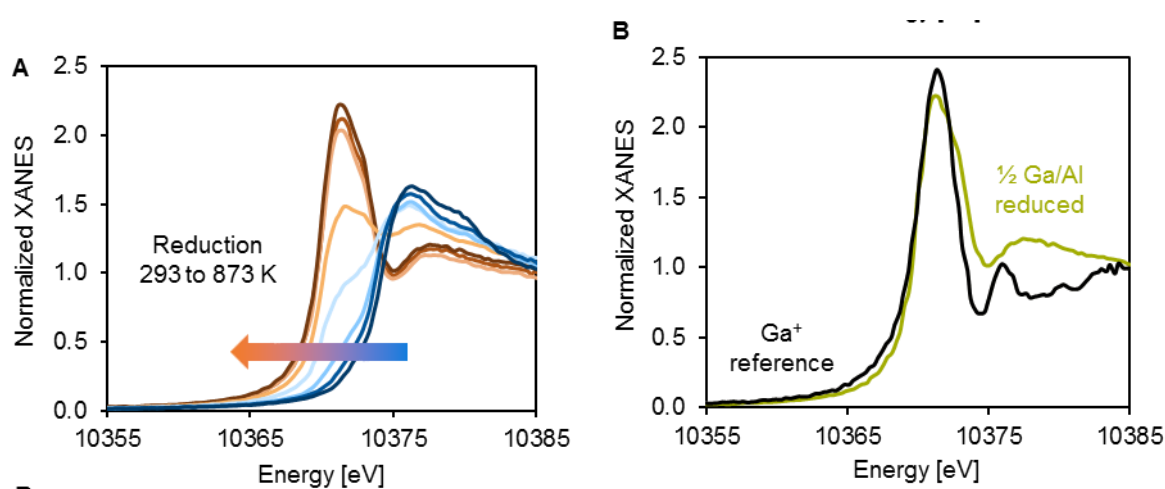


Figure 3. A. Change of edge energy of Ga species during reduction of $\frac{1}{2}$ Ga/Al Ga/H-ZSM-5 and B. comparison of edge energy of $\frac{1}{2}$ Ga/Al Ga/H-ZSM-5 during reaction with Ga⁺¹ reference.

To further differentiate between Ga⁺ and [GaH₂]⁺¹ the stoichiometry of H₂ consumption and H₂O formation during reduction of $\frac{1}{2}$ Ga/Al, containing only Ga species substituting for protons, was followed (Figure S5). The catalyst was initially calcined in order to assure that all Ga species are in non-hydroxylated Ga³⁺ state and subsequently reduced in H₂. The catalyst reduction resulted in a H₂ consumption of H_{2, consumed}/Ga₂O₃ = 2:1 and H₂O formation leading to a ratio of H_{2, consumed}/H₂O_{formed} = 2:3. The potential reactions of Ga₂O₃ with H₂ to form reduced Ga species are summarized below (Figure 4). Combining the specific consumption of H₂ and its ratio to the concentration of H₂O formed (Figure 5) allows us to conclude that after reduction at high temperatures Ga⁺ was selectively formed. Thus, we also conclude that the band of coordinatively adsorbed pyridine at 1457 cm⁻¹ and the white line at 10370.2 eV are characteristic of the existence of Ga⁺ in a homotopic site.

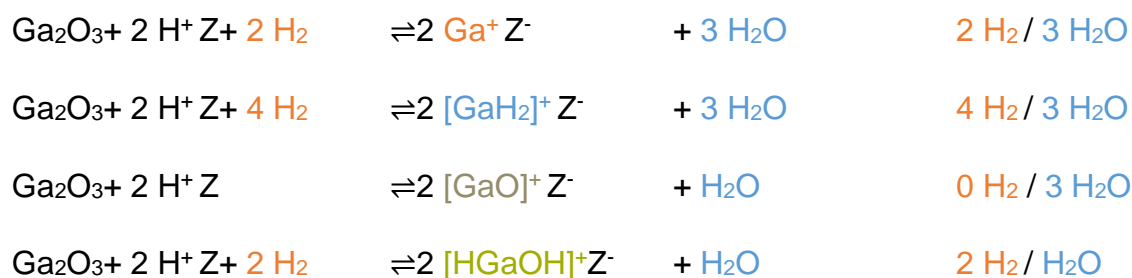


Figure 4. Plausible reactions of H₂ with Ga₂O₃.

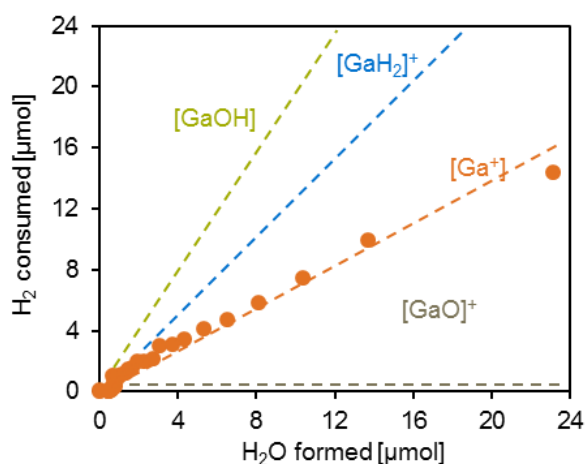


Figure 5. Consumption of H₂ as a function of H₂O formation during the pulsed TPR of the 1/2 Ga/Al Ga/H-ZSM-5 catalyst.

4.4.3 Mechanism of propane dehydrogenation on Lewis-Brønsted acid pairs

The maximum in dehydrogenation rate was observed at the catalyst with a Ga/Al ratio of 0.5, for which Ga⁺ and Brønsted acid sites are present in equal concentrations. The observed reaction rate was about 50 times higher than the reaction rate expected for additive contributions of Ga₂O₃ and Brønsted acid sites only, pointing to the synergy between Ga⁺ and Brønsted acid sites. Comparing turnover frequencies of these Lewis-Brønsted acid pairs (1/2 Ga/Al Ga/H-ZSM-5) to isolated Brønsted acid sites (H-ZSM-5) and to active sites on Ga₂O₃ (Ga₂O₃/SiO₂), shows that the Lewis-Brønsted acid pairs are by far the most active sites (Table 3).

Table 3: Turnover frequencies of propane dehydrogenation on Brønsted acid sites, Lewis-Brønsted acid pairs, isolated Ga⁺ and Ga₂O₃ 783 K (Rates x 10⁴ [mol_{propane} · (mol_{active site} · s)⁻¹]).

Active site	SiOHAl	SiO(Ga)Al-SiOHAl	Ga ₂ O ₃
Turnover frequency	0.14	93.76	1.40

Direct analysis of the mechanism is challenging. The synergistic site cannot be characterized by the specificity of the adsorption of alkanes, as they adsorb separately on both Ga⁺ and Brønsted acid sites. Neither allow H/D exchange experiments insight into the mechanism, as H/D exchange is equilibrated in presence of Brønsted acid sites at the temperatures of the reaction.⁶ The regioselectivity of the dehydrogenation, i.e., the presence of 1-butene, which would be formed if dehydrogenation would take place via hydride abstraction by Ga, cannot be used to distinguish between mechanisms proposed, as hydride shifts on Brønsted acid sites are also equilibrated at the studied reaction temperatures.³

Thus, in order to distinguish between a classic protolytic dehydrogenation over Brønsted acid sites facilitated by Ga⁺^{9, 16} and hydride abstraction from the alkane by Ga⁺,^{7, 15} the reaction order of the dehydrogenation was studied. The reaction order of dehydrogenation passing over a carbonium ion in the transition state (TS)²⁵ over H-ZSM-5 is one (Figure S6).⁵ Reaction rates are proportional to the alkane fugacities, while only a small fraction of Brønsted acid sites is occupied. The formation of the carbonium ion has been suggested to go through a late transition state, with H-H bonds being nearly formed.³ This involves the protonation of a C-H bond in C₃H₈ to form a C-H-H three-center two electron bond, which is less stable than the C-C-H analogues formed during cracking.²⁶

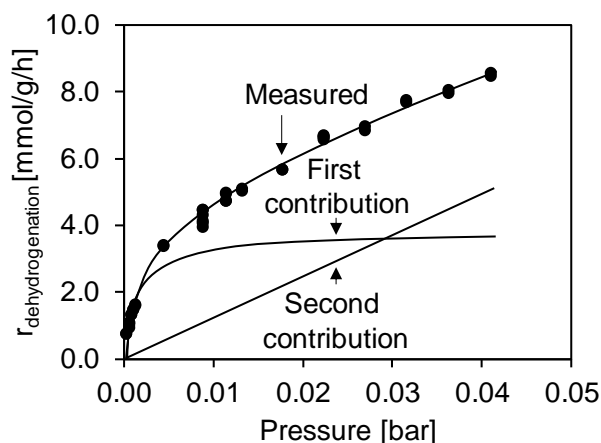


Figure 6: Representation of measured reaction rates and contributions of two additive mechanisms over $\frac{1}{2}$ Ga/Al Ga/H-ZSM-5 with propane partial pressures ranging from 0.25 – 45 mbar at 783 K.

Dependence of the reaction rate showed a significant slower rate at the upper end of the explored partial pressures from 0.25 to 45 mbar. While a reaction order of $\frac{1}{2}$ Ga/Al of 0.5 over a range of partial pressures (Figure SI 7) was determined, a closer inspection points to two additive mechanisms of first-order (Fig 6). The contributions for the two reactions were estimated by assuming that at low partial pressures the reaction was determined by catalysis from a site that binds propane rather strongly, but has a limited concentration on the catalyst. At high partial pressures the reaction is been hypothesized to be dominated by a first-order reaction catalyzed by sites with a rather weak interaction with propane, but being more abundant on the studied catalyst. Extrapolation of this second contribution allows to estimate the upper limit of the impact of the first pathway. We hypothesize at present that both pathways catalyze dehydrogenation and cracking of propane in a monomolecular mechanism.

We speculate at present that the first pathway is associated with a small number of defects on Ga-ZSM5, but we intend to systematically vary potential defect sites to corroborate the origin of these sites. The main active site catalyzes dehydrogenation via a mechanism involving both Ga^+ and Brønsted acid sites, as hypothesized by theoretical modeling below. Because the catalytically active sites form only at high temperatures, it is currently not possible to reliably quantify the concentration of the sites. If we estimate them to be equal to approximately half of the total concentration of BAS, the sites saturating in the low propane partial pressure region are an order in magnitude below to those in the high pressure region in concentration. These two sites could result from a heterogeneous Al distribution within the zeolite lattice, resulting in

different distances between the two Al of a pair, being one exchanged with Ga and the other withholding the BAS.

It should be noted that within this hypothesis, the measured apparent activation enthalpy is related to the contribution of the mechanism dominant at low pressures. The two sites involved in the heterolytic dissociation are proposed to have two (different) functions, stabilizing R^- and H^+ . In consequence, the highest rate is observed at equal concentrations of Ga^+ and BAS (Figure 1). When all BAS are replaced by Ga^+ , the heterolytic dissociation of the alkane may occur between Ga^+ and framework oxygen.²⁷ In absence of Ga^+ , H-ZSM-5, only one Brønsted acid site is also involved, however, passing through a carbonium ion in the transition state (TS).²⁵ To corroborate these models and to probe potential surface intermediates several of these reaction paths were explored via DFT calculations.

4.4.4 DFT calculations

Three mechanisms were examined for propane dehydrogenation on H-ZSM-5 and Ga/H-ZSM-5. The first is the Brønsted acid mechanism, which occurs by protonation of a C-H bond. The second is the Lewis acid mechanism, which occurs by heterolytic cleavage of a C-H bond, with the Ga^+ acting as a Lewis acid that stabilizes the resulting negatively charged alkyl fragment. The third mechanism, which we call the Lewis-Brønsted acid mechanism, occurs via bifunctional catalysis involving cooperativity between the BAS and LAS. While the Brønsted and Lewis acid mechanisms can also occur on isolated Brønsted and Lewis acid sites, respectively, the Lewis-Brønsted acid mechanism requires both BAS and LAS in close proximity.

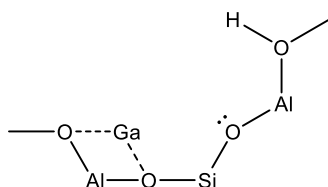


Figure 7. Structural representation of a Lewis-Brønsted acid site (LBAS) pair.

4.4.4.1 Brønsted acid site mechanism

It is well known that alkane dehydrogenation can occur over a BAS by protonation of a C-H bond.^{4, 6} We examined whether the presence of a nearby Ga^+ on the LBAS can

lower the activation barrier for this mechanism by polarization of the C-H bond, as mentioned by Hutchings¹⁶. The reaction initiates by protonation of the methylene C-H bond of propane, which dissociates in the process to form an i-propenium cation and H₂ (Figure). The i-propenium then transfers a methyl proton to a framework oxygen to form the propene product.

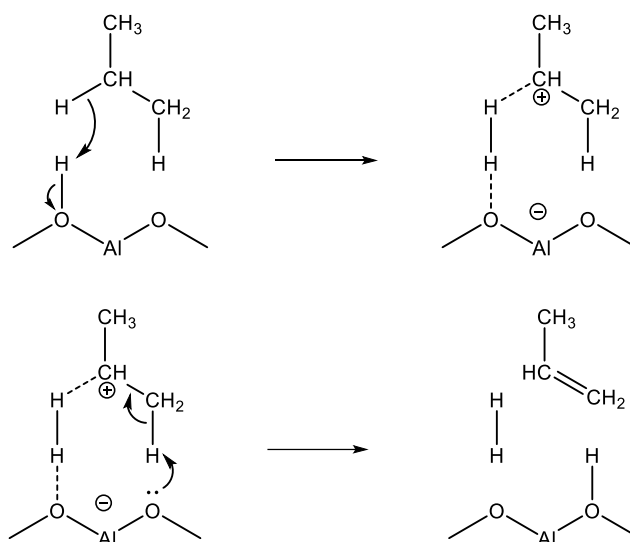


Figure 8: Brønsted acid mechanism for propane dehydrogenation on the LBAS pair (the other Al center and the Ga⁺ are not shown).

The transition state resembles an i-propenium cation coordinated to an H₂ molecule, with the H₂ also interacting with a basic framework oxygen. At no point along the reaction trajectory is the classical 5-center carbonium ion formed, as the proton interacts only with the hydride and not the carbon. This transition state structure is similar to one found in another DFT study of butane dehydrogenation on Ga-free H-ZSM-5.²⁸ It is consistent with the conclusion of Kotrel et al.²⁹ that transition state of alkane cracking and dehydrogenation reactions are distinctively different. The calculated apparent activation enthalpy for this reaction is 181 kJ/mol, expectedly higher than the apparent activation enthalpy we calculate for an isolated H⁺ site (155 kJ/mol). This indicates that the presence of Ga⁺ does not increase the activity of the Brønsted acid mechanism, so that a different mechanism must be responsible for the increased activity of the LBAS pair.

We would like to point out that the apparent activation enthalpy calculated for propane dehydrogenation on an isolated H⁺ site (155 kJ/mol) is much lower than the experimentally measured apparent activation enthalpy (199±7 kJ/mol). Considering the

heat of adsorption the value agrees well with the 190 kJ/mol reported in another DFT study.²⁸ Note that the lower value for intrinsic activation barriers by GGA DFT functionals is known for acid catalyzed reactions in zeolites and arises from excessive charge delocalization due to the electron self-interaction error in these functionals.³⁰ In the other mechanisms that we examine below that do not proceed through carbenium ion intermediates, the DFT barriers are expected to be significantly closer to the experimental values.

4.4.4.2 Lewis acid mechanism

The second mechanism for propane dehydrogenation in presence of Ga^+ , originally proposed by Pidko et al. and called the “alkyl” mechanism,²⁷ involves heterolytic dissociation of the C-H bond over Ga^+ and a basic framework oxygen, with the alkyl fragment binding to the former and the proton binding to the latter. Here, we examine this mechanism over the LBAS pair to determine, if it could be responsible for the enhanced activity of the Ga/H-ZSM-5. The initial step involves the heterolytic C-H bond dissociation to form an intermediate state (I, Figure 9). As Ga^+ is not a strong Lewis acid, this intermediate is very high in enthalpy, 176 kJ/mol relative to the initial state (A) with propane in the gas phase. The proton in the intermediate then transfers to Ga^+ , formally oxidizing it to Ga^{3+} (state B), with an intrinsic enthalpy of 53 kJ/mol and an apparent activation enthalpy of 240 kJ/mol.

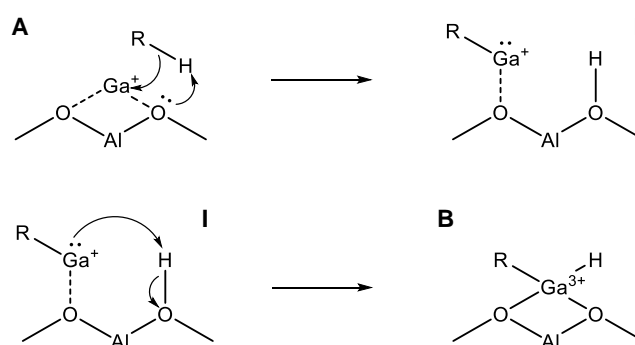


Figure 9. Alkane addition to Ga of the LBAS (the other Al and the BAS are not shown).

In a following step (Figure 10), the hydride bound to the Ga abstracts a proton from a terminal C-H bond of the i-propyl to simultaneously eliminate H_2 and propene, regenerating the initial state A of the active site.

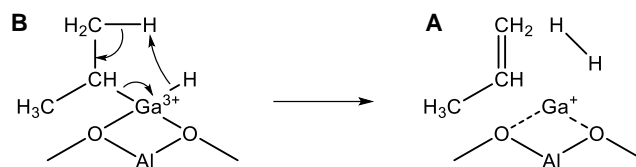


Figure 10. Concerted elimination of the alkene and H_2 from the Ga of the LBAS (the other Al and the BAS are not shown).

This step has a calculated apparent activation enthalpy of 202 kJ/mol, making the alkane addition step rate limiting. In contrast, Pidko et al.²⁷ found the elimination step to be rate limiting, although the barrier they calculate (233 kJ/mol) is similar to ours. As the apparent activation enthalpy of 240 kJ/mol is higher than for the Brønsted acid mechanism on the isolated BAS (181 kJ/mol), we conclude that Ga^+ by itself is not sufficient to lower the barrier for propene dehydrogenation.

4.4.4.3 Bifunctional Lewis-Brønsted acid mechanism

As neither the Brønsted acid nor Lewis acid mechanism could account for the increased propane dehydrogenation activity of the LBAS pair, we probe a third mechanism that is explicitly bifunctional in nature. This mechanism originates from the protonation of the Ga^+ by the adjacent BAS to form a $[GaH]^2+$. This species, in which the Ga is in the formal +3 oxidation state, is a much stronger Lewis acid than Ga^+ , as evidenced by an increase in the charge on the Ga from 0.55 to 1.01 (Löwdin charge, calculated using the quasiatomic orbital method³¹⁻³²). The transfer of the proton from the BAS to the Ga^+ occurs from the lowest free energy state of the LBAS (A) in two sequential steps, $A \rightarrow A'$ and $A' \rightarrow A''$, with A' and A'' being 35 kJ/mol and 75 kJ/mol higher in enthalpy than state A (Figure 11).

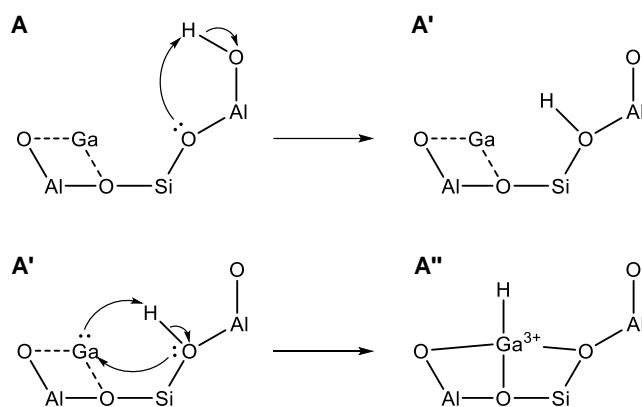


Figure 11. Two steps involved in the protonation of the Ga⁺ by the BAS to form the active [GaH]²⁺.

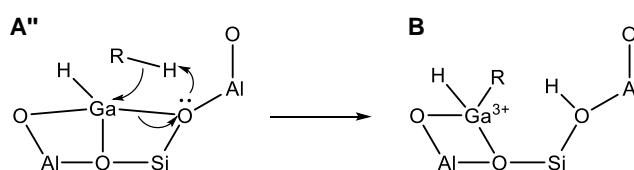
Although the [GaH]²⁺ species in state A'' is much higher in enthalpy, it is significantly more reactive for heterolytic C-H activation, owing to the higher Lewis acidity of Ga³⁺ compared to Ga⁺.

The by far most populated state at reaction conditions is the ground state of the Lewis-Brønsted acid pair (A), as evidenced by very low equilibrium constants of the other states (Table 4) calculated based on the DFT values of the standard Gibbs free energy (Figure 15). This is in line with the experimental results.

Table 4. Standard Gibbs free energies and equilibrium constants of calculated states in relation to the state comprising the Lewis-Brønsted acid pair ground state and propane in the gas phase (A).

State	$\Delta G^{\circ}_{783\text{ K}}$ [kJ · mol ⁻¹]	K
A''	92	$7.3 \cdot 10^{-7}$
A'' + R	246	$3.9 \cdot 10^{-17}$
TS-1	325	$2.1 \cdot 10^{-22}$
B	242	$7.2 \cdot 10^{-17}$
TS-2	322	$3.3 \cdot 10^{-22}$
C	82	$3.4 \cdot 10^{-6}$
TS-3	175	$2.1 \cdot 10^{-12}$
A + P	83	$2.9 \cdot 10^{-6}$

As with the alkane addition step of the Lewis acid mechanism, the negative alkyl fragment binds to the Ga³⁺ while the proton is transferred to a basic framework oxygen (state B, Figure 12). Either a methyl or methylene C–H bond can be cleaved in this step, with both pathways having the same calculated apparent activation enthalpy of 108 kJ/mol (relative to state A and gas phase propane, 55 kJ/mol relative to propane physisorbed on state A''), which is far below the barriers of the other two pathways.


Figure 12. Alkane addition to the LBAS.

In the next step (Figure 13), the proton on the BAS, formed from dissociation of the alkane C–H bond, combines with the hydride bound to the Ga to eliminate H₂, resulting in state C in which only the alkyl fragment is bound to the Ga.

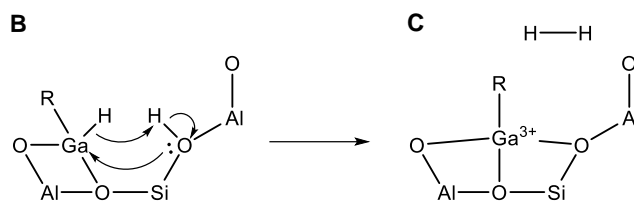


Figure 13. H_2 elimination from the LBAS.

This step also has a low calculated apparent activation enthalpy (103 kJ/mol for both the methyl and methylene pathways) that is very similar to that of the alkyl addition step. This is likely due to the similar mechanism involved – the reverse of this step is heterolytic H–H activation, which is analogous to heterolytic C–H activation occurring during the alkyl addition step. The much lower barrier compared to the concerted alkene/ H_2 elimination step of the Lewis acid mechanism is made possible by the bifunctionality of the LBAS, as the BAS which combines with the hydride is much more acidic than the C–H bond of the alkyl fragment which combines with the hydride in the latter mechanism.

Finally, the *i*-propyl (*n*-propyl for the methyl pathway) bound to the Ga desorbs as an *i*-proponium (*n*-proponium) cation, which is then deprotonated by a basic framework oxygen to eliminate propene (Figure 14).

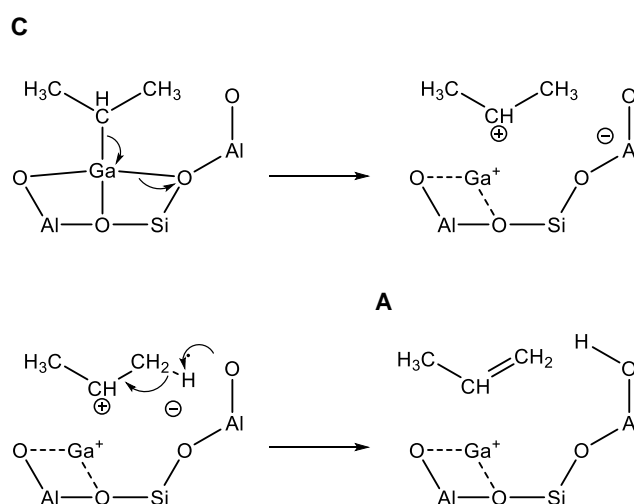


Figure 14. Alkene elimination from the LBAS.

As the *i*-proponium (*n*-proponium) desorbs, the two electrons in the C–Ga bond localize on the Ga^{3+} , formally reducing it to Ga^+ and returning the active site to the initial state

A. The calculated apparent activation enthalpy of this step is significantly lower for the methylene pathway (151 kJ/mol) than for the methyl pathway (179 kJ/mol), as the former occurs through a more stable secondary carbenium cation compared to the latter, which occurs through a primary carbenium ion. Even though the apparent activation enthalpy is higher than for the first two steps, the apparent activation free energy is much lower since a significant amount of entropy is released by H₂ elimination in the second step. Therefore, the propene elimination step is not rate limiting according to the calculated free energies.

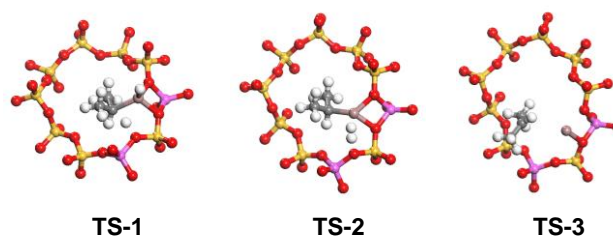


Figure 15. Transition state structures for alkane addition (TS-1), H₂ elimination (TS-2), and alkene elimination (TS-3) of the bifunctional mechanism.

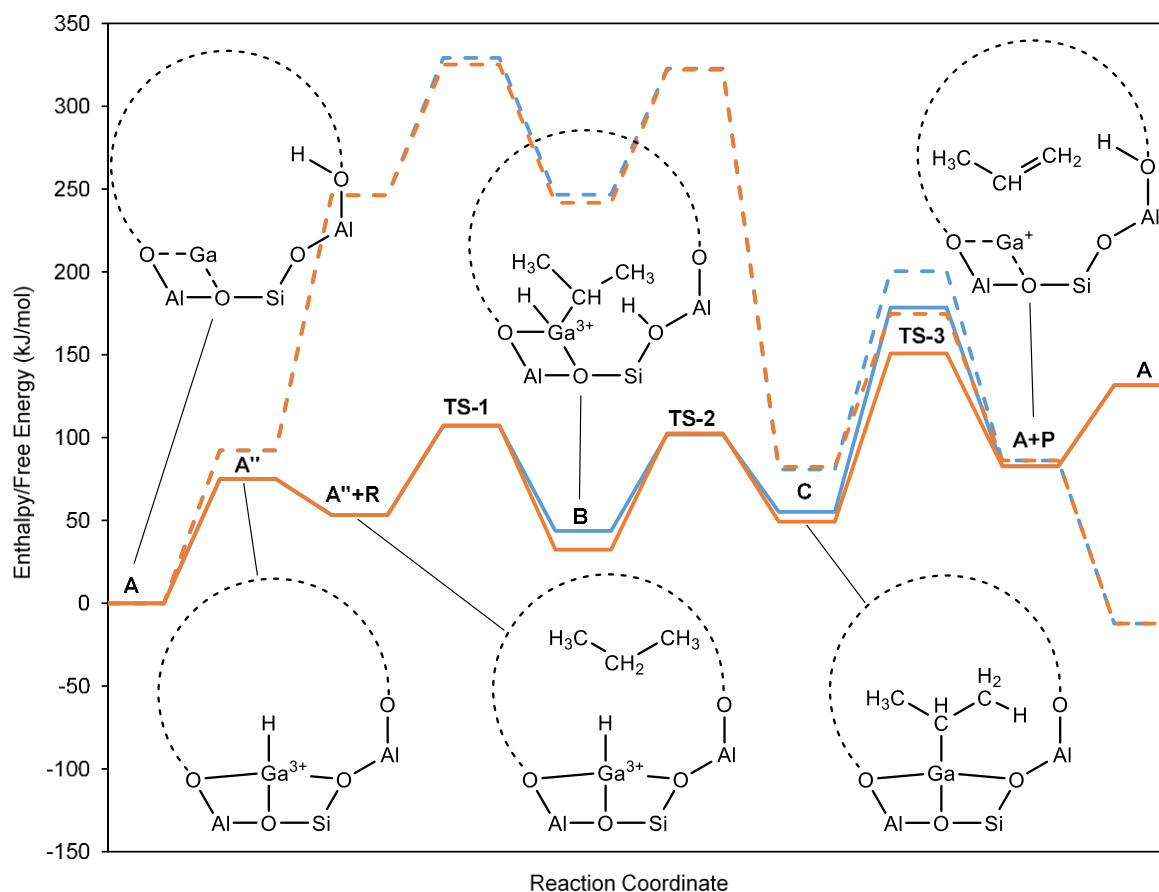


Figure 16. Enthalpy (solid lines) and free energy (dashed lines) profiles for the bifunctional Lewis/Brønsted acid mechanism, occurring by activation of a methyl (blue) or methylene (orange) C–H bond. Calculated at 783 K, 10 mbar propane, 0.1 mbar propene, 0.1 mbar H_2 . The labels for the intermediates (A, A'', B, C) and transition states (1, 2, 3) are indicated on the horizontal axis, with R representing physisorbed propane and P representing physisorbed propene.

The structures of the transition states for the three steps of the bifunctional mechanism are shown in Figure 15, while the overall energy and free energy profiles for this mechanism are summarized in Figure 16. We note that the transition states of the first and second steps (propane addition and H_2 elimination) have the highest free energies and are, thus, both kinetically relevant, while the propene elimination step is not. The apparent activation energy is, therefore, expected to be between those of the first and second steps (103 – 108 kJ/mol).

Alkane dehydrogenation by the $[GaH]^{2+}$ species was also examined in DFT studies by Joshi and Thomson³³ and Pidko et al.²⁷. In the first study, it was concluded that $[GaH]^{2+}$ associated with two nearby Al centers was the active species responsible for ethane dehydrogenation in Ga/H-ZSM-5, although they propose a “carbenium” mechanism whereby the C–H bond heterolytically dissociates with reverse polarization to form a

hydride bound to the Ga center and an ethenium cation bound to the framework oxygen. On the most favorable site for alkane activation, they calculate an activation energy of 150 kJ/mol with respect to $[\text{GaH}]^{2+}$ and gas phase ethane. However, they did not consider that having the Ga^+ on one Al center and the proton on the other (Ga^+/H^+ , analogous to state A in Figure 16) is lower in energy than $[\text{GaH}]^{2+}$. We calculated this energy difference on the same site that they use and find that Ga^+/H^+ is lower in energy by 41 kJ/mol, leading to an apparent activation energy of 191 kJ/mol.

Pidko et al. examined both the “carbenium” mechanism as well as the “alkyl” mechanism for ethane dehydrogenation and found that the latter has a significantly lower activation energy,²⁷ although still quite high (172 kJ/mol with respect to $[\text{GaH}]^{2+}$ and gas phase ethane). This activation energy was calculated for a structure in which the two Al centers were far apart (8.14 Å), so that the basic framework oxygens associated with the second Al center were too far away to accept the proton during C-H bond activation. Instead, the proton is transferred to a much less basic Si-O-Si oxygen, which is likely responsible for the high barrier. They also examined a second structure in which both Al centers were located within the same 5-membered ring; however, the geometry is such that the $[\text{GaH}]^{2+}$ strongly coordinates to four framework oxygens, making it unreactive for C-H bond activation. In the structure we examine, the two Al centers are located within a 10-membered ring so that the $[\text{GaH}]^{2+}$ is only coordinated to three framework oxygens and is therefore significantly more reactive.

For this latter pathway, the apparent activation enthalpies for propane and butane dehydrogenation over $\frac{1}{2}$ Ga/Al were significantly below the apparent activation enthalpy for H-ZSM-5 (Table 5). While the values for $\Delta H^{\ddagger}_{\text{App.}}$ and $\Delta S^{\ddagger}_{\text{App.}}$ for SiOHAl⁴, the values obtained in presence of Ga^+ must be caused by the different reaction path discussed above. In H-ZSM-5 the dehydrogenation occurs via the formation of a carbonium ion in the transition state, on Lewis-Brønsted acid pairs the reaction pathway involves the heterolytic activation of the alkane.

Table 5. Apparent activation entropy and enthalpy for active sites in the propane and *n*-butane dehydrogenation. Kinetics measured in the range of 783 – 823 K at a propane partial pressure of 8.75 mbar. The following abbreviations have been made: Alkane (Alk.), Propane (Pro.) and *n*-Butane (But.).

Alk.	SiOHAl		SiO(Ga)Al-SiOHAl	
	$\Delta H^{\ddagger}_{\text{App.}}$ [kJ·mol ⁻¹]	$\Delta S^{\ddagger}_{\text{App.}}$ [J·mol ⁻¹ ·K ⁻¹]	$\Delta H^{\ddagger}_{\text{App.}}$ [kJ·mol ⁻¹]	$\Delta S^{\ddagger}_{\text{App.}}$ [J·mol ⁻¹ ·K ⁻¹]
Exp.				
Pro.	199 ± 7.0	-52.0 ± 3.1	129 ± 6.6	-87.1 ± 6.5
But.	186 ± 4.4	-50.9 ± 2.0	134 ± 7.2	-86.2 ± 5.7
DFT				
Pro.	155	-168	106	-221
But.	-	-	92	-228

4.5 Conclusion

On Ga/H-ZSM-5 catalysts with varying Ga/Al ratio three different sites, namely Ga⁺, Brønsted acid sites and Ga_xO_y were found. The Ga⁺ and Brønsted acid site concentration changed inversely, as Ga⁺ was exchanged with Brønsted acid site protons. At high Ga/Al ratios (>0.5) additional Ga₂O₃ clusters were formed. The highest dehydrogenation rate (two orders of magnitude faster than the parent H-ZSM-5 and Ga₂O₃/SiO₂ with the same Ga₂O₃ loading) was observed for a Ga/Al ratio of 0.5, corresponding to a one to one ratio of Ga⁺ and Brønsted acid sites. This indicates a synergy between Ga⁺ and a Brønsted acid site, forming a Lewis-Brønsted acid pair in the dehydrogenation of alkanes. The well-defined catalyst ½ Ga/Al, containing mainly (kinetically dominating, but not exclusively) homotopic Lewis Brønsted acid pairs, allowed us to study the mechanism and the kinetics of the alkane dehydrogenation on these Lewis-Brønsted acid pairs experimentally and via DFT calculations. A 0.5 reaction order with respect of propane, implies the dissociative adsorption of propane on zeolite exchange sites, one compensated by H⁺ and the other by Ga⁺. The highest rates in propane dehydrogenation were, thus, found at equal concentrations of Brønsted acid and Lewis acid Ga⁺ sites. While a reasonably high concentration of such pairs are kinetically dominating (the rate increased by more than 300 times compared

to the two extreme cases of pure H-ZSM-5 and the fully exchanged Ga-ZSM-5) statistics of site distribution dictates that also some isolated Brønsted acid sites and Ga sites must exist.

The DFT calculations indicate that the Lewis-Brønsted acid site pair carries out alkane dehydrogenation through a bifunctional mechanism in which the Brønsted acid site protonates the Ga^+ to form a $[\text{GaH}]^{2+}$, which is a strong Lewis acid. The $[\text{GaH}]^{2+}$, together with a basic framework oxygen of the Brønsted the assessment of separately in two sequential steps. This Lewis-Brønsted acid pair is found to be much more active than an isolated Ga^+ due to the large increase in Lewis acidity upon protonation of Ga^+ by the Brønsted acid site, which facilitates heterolytic C-H bond activation. The Brønsted acid site also significantly reduces the activation barrier for H_2 elimination by recombination with a hydride compared to the isolated Ga^+ , on which the proton comes from an alkyl C-H bond to simultaneously eliminate propene.

These findings provide fundamental insight into the mechanism of alkane dehydrogenation over Lewis-Brønsted acid site pairs. The insight allows not only the systematic development of highly active dehydrogenation catalysts, but offers in general a new perspective on cooperative catalysis by Lewis and Brønsted acid sites in heterogeneous catalysis.

4.6 Acknowledgement

Financial support support for M. W. S. in the framework of the AlgenFlugKraft project (LaBay74) of the Bavarian Ministry of Economic Affairs and Media, Energy and Technology (Bayerisches Staatsministerium für Wirtschaft und Medien, Energie und Technologie) and of the Bavarian State Ministry of Education, Science and the Arts (Bayerisches Staatsministerium für Bildung und Kultus, Wissenschaft und Kunst) is appreciated. RBD acknowledges the Alexander von Humboldt foundation for financial support.

The authors thank Prof. Dr. Tom Nilges for ICP-OES measurements. Furthermore, we thank Martin Neukamm and Xaver Hecht for technical support and Andreas Ehrmaier, Takaaki Ikuno, Daniel Melzer and Matthias Steib for carrying out parts of the XANES

measurements. The XANES experiments were performed at CLAEISS beamline at ALBA Synchrotron with the collaboration of ALBA staff.

4.7 Literature

1. Sattler, J. J. H. B.; Ruiz-Martinez, J.; Santillan-Jimenez, E.; Weckhuysen, B. M., Catalytic Dehydrogenation of Light Alkanes on Metals and Metal Oxides. *Chemical Reviews* **2014**, *114* (20), 10613-10653.
2. Xu, B.; Sievers, C.; Hong, S. B.; Prins, R.; van Bokhoven, J. A., Catalytic activity of Brønsted acid sites in zeolites: Intrinsic activity, rate-limiting step, and influence of the local structure of the acid sites. *Journal of Catalysis* **2006**, *244* (2), 163-168.
3. Gounder, R.; Iglesia, E., Catalytic Consequences of Spatial Constraints and Acid Site Location for Monomolecular Alkane Activation on Zeolites. *Journal of the American Chemical Society* **2009**, *131* (5), 1958-1971.
4. Gounder, R.; Iglesia, E., Catalytic hydrogenation of alkenes on acidic zeolites: Mechanistic connections to monomolecular alkane dehydrogenation reactions. *Journal of Catalysis* **2011**, *277* (1), 36-45.
5. Narbeshuber, T. F.; Brait, A.; Seshan, K.; Lercher, J. A., Dehydrogenation of Light Alkanes over Zeolites. *Journal of Catalysis* **1997**, *172* (1), 127-136.
6. Narbeshuber, T. F.; Vinek, H.; Lercher, J. A., Monomolecular Conversion of Light Alkanes over H-ZSM-5. *Journal of Catalysis* **1995**, *157* (2), 388-395.
7. Kwak, B. S.; Sachtler, W. M. H., Effect of Ga/Proton Balance in Ga/HZSM-5 Catalysts on C3 Conversion to Aromatics. *Journal of Catalysis* **1994**, *145* (2), 456-463.
8. Schüßler, F.; Schallmoser, S.; Shi, H.; Haller, G. L.; Ember, E.; Lercher, J. A., Enhancement of Dehydrogenation and Hydride Transfer by La³⁺ Cations in Zeolites during Acid Catalyzed Alkane Reactions. *ACS Catalysis* **2014**, *4* (6), 1743-1752.
9. Biscardi, J. A.; Iglesia, E., Structure and function of metal cations in light alkane reactions catalyzed by modified H-ZSM5. *Catalysis Today* **1996**, *31* (3), 207-231.
10. Davies E.E.; A.J., K. 509285, 1979.
11. Price, G. L.; Kanazirev, V., Ga₂O₃/HZSM-5 propane aromatization catalysts: Formation of active centers via solid-state reaction. *Journal of Catalysis* **1990**, *126* (1), 267-278.
12. Meitzner, G. D.; Iglesia, E.; Baumgartner, J. E.; Huang, E. S., The Chemical State of Gallium in Working Alkane Dehydrocyclodimerization Catalysts. In situ Gallium K-Edge X-Ray Absorption Spectroscopy. *Journal of Catalysis* **1993**, *140* (1), 209-225.
13. Gonzales, N. O.; Chakraborty, A. K.; Bell, A. T., A density functional theory study of hydrogen recombination and hydrogen-deuterium exchange on Ga/H-ZSM-5. *Topics in Catalysis* **1999**, *9* (3), 207-213.
14. Getsoian, A.; Ujjal Das, U.; Camacho-Bunquin, J.; Zhang, G.; Gallagher, J. R.; Hu, B.; Cheah, S.; Schaidle, J. A.; Ruddy, D. A.; Hensley, J. E.; Krause, T. R.; Curtiss, L. A.; Miller, J. T.; Hock, A. S., Organometallic model complexes elucidate the active gallium species in alkane dehydrogenation catalysts based on ligand effects in Ga K-edge XANES. *Catalysis Science & Technology* **2016**, *6* (16), 6339-6353.
15. Meriaudeau, P.; Naccache, C., The role of Ga₂O₃ and proton acidity on the dehydrogenating activity of Ga₂O₃-HZSM-5 catalysts: evidence of a bifunctional mechanism. *Journal of Molecular Catalysis* **1990**, *59* (3), L31-L36.
16. Buckles, G.; Hutchings, G. J.; Williams, C. D., Aromatization of propane over Ga/H-ZSM-5: An explanation of the synergy observed between Ga³⁺ and H⁺. *Catalysis Letters* **1991**, *11* (1), 89-93.
17. Bearden, J. A., X-Ray Wavelengths. *Reviews of Modern Physics* **1967**, *39* (1), 78-124.
18. Kresse, G.; Furthmüller, J., Efficient iterative schemes for ab initio total-energy calculations using a plane-wave basis set. *Physical Review B* **1996**, *54* (16), 11169-11186.

19. Hammer, B.; Hansen, L. B.; Nørskov, J. K., Improved adsorption energetics within density-functional theory using revised Perdew-Burke-Ernzerhof functionals. *Physical Review B* **1999**, *59* (11), 7413-7421.
20. Grimme, S., Semiempirical GGA-type density functional constructed with a long-range dispersion correction. *Journal of Computational Chemistry* **2006**, *27* (15), 1787-1799.
21. Blöchl, P. E., Projector augmented-wave method. *Physical Review B* **1994**, *50* (24), 17953-17979.
22. Henkelman, G.; Jónsson, H., Improved tangent estimate in the nudged elastic band method for finding minimum energy paths and saddle points. *The Journal of Chemical Physics* **2000**, *113* (22), 9978-9985.
23. Henkelman, G.; Jónsson, H., A dimer method for finding saddle points on high dimensional potential surfaces using only first derivatives. *The Journal of Chemical Physics* **1999**, *111* (15), 7010-7022.
24. Guisnet, M.; Gnep, N. S.; Aittaleb, D.; Doyemet, Y. J., Conversion of light alkanes into aromatic hydrocarbons. *Applied Catalysis A: General* **1992**, *87* (2), 255-270.
25. Lercher, J. A.; van Santen, R. A.; Vinek, H., Carbonium ion formation in zeolite catalysis. *Catalysis Letters* **1994**, *27* (1), 91-96.
26. Esteves, P. M.; Alberto, G. G. P.; Ramírez-Solís, A.; Mota, C. J. A., Ab Initio Study of the Adamantonium Cations: the Protonated Adamantane. *The Journal of Physical Chemistry A* **2001**, *105* (17), 4308-4311.
27. Pidko, E. A.; Kazansky, V. B.; Hensen, E. J. M.; van Santen, R. A., A comprehensive density functional theory study of ethane dehydrogenation over reduced extra-framework gallium species in ZSM-5 zeolite. *Journal of Catalysis* **2006**, *240* (1), 73-84.
28. Mallikarjun Sharada, S.; Zimmerman, P. M.; Bell, A. T.; Head-Gordon, M., Insights into the Kinetics of Cracking and Dehydrogenation Reactions of Light Alkanes in H-MFI. *The Journal of Physical Chemistry C* **2013**, *117* (24), 12600-12611.
29. Kotrel, S.; Knözinger, H.; Gates, B. C., The Haag-Dessau mechanism of protolytic cracking of alkanes. *Microporous and Mesoporous Materials* **2000**, *35-36*, 11-20.
30. Svelle, S.; Tuma, C.; Rozanska, X.; Kerber, T.; Sauer, J., Quantum Chemical Modeling of Zeolite-Catalyzed Methylation Reactions: Toward Chemical Accuracy for Barriers. *Journal of the American Chemical Society* **2009**, *131* (2), 816-825.
31. Qian, X.; Li, J.; Qi, L.; Wang, C.-Z.; Chan, T.-L.; Yao, Y.-X.; Ho, K.-M.; Yip, S., Quasiatomic orbitals for ab initio tight-binding analysis. *Physical Review B* **2008**, *78* (24), 245112.
32. Plaisance, C. P.; van Santen, R. A.; Reuter, K., Constrained-Orbital Density Functional Theory. Computational Method and Applications to Surface Chemical Processes. *Journal of Chemical Theory and Computation* **2017**, *13* (8), 3561-3574.
33. Joshi, Y. V.; Thomson, K. T., The roles of gallium hydride and Brønsted acidity in light alkane dehydrogenation mechanisms using Ga-exchanged HZSM-5 catalysts: A DFT pathway analysis. *Catalysis Today* **2005**, *105* (1), 106-121.

4.8 Associated Content

4.8.1 Additional Information

See supporting information.

4.8.2 Notes and Author Contributions

Moritz W. Schreiber planned, performed and evaluated synthesis, characterization and kinetic experiments. Martin Baumgärtl performed and evaluated synthesis, characterization and kinetic experiments within a Master's Thesis. Results were discussed with Andreas Jentys Ricardo Bermejo-Deval and Johannes A. Lercher. DFT calculations were performed by Craig P. Plaisance and Karsten Reuter. Moritz W. Schreiber drafted the manuscript. The draft of the manuscript on the DFT calculations was drafted by Craig P. Plaisance. Moritz W. Schreiber, Craig P. Plaisance, Karsten Reuter, Andreas Jentys Ricardo Bermejo-Deval and Johannes A. Lercher revised the manuscript.

Conclusion

In the first part, the hydrodeoxygenation of triglycerides and related model fatty acid alkyl esters (tristearate, methyl stearate) over Ni supported on MFI type zeolites were studied. Triglycerides are too large to access zeolite micropores. Therefore, the question was addressed, if catalytic activity can be enhanced by using hierarchical supports (containing a micro- and mesopore system), overcoming potential access and diffusion restrictions (Chapter 2). Catalysts with hierarchical compared to conventional support structure indeed showed higher reaction rates by a factor of four in the deoxygenation of microalgae oil, tristearate and methyl stearate. The higher activity is related to a better dispersion of Ni on the hierarchical supports. However, rates normalized to accessible Ni (TOF) are comparable. TOF of methyl stearate and tristearate are independent of support morphology, indicating that the majority of Ni particles responsible for conversion are located on the outer surface of the zeolites. In a second step, the enhancement of intrinsic Ni activity by Brønsted acid sites for the C-O hydrogenolysis of key intermediates of triglyceride conversion was studied, aiming to understand the effect typically reported for noble metals in different reactions (Chapter 3). TOF of C-O hydrogenolysis of methyl stearate and stearic acid increase proportionally to concentration of Brønsted acid sites of MFI type supports up to a factor of eight for the studied range of Brønsted acid site concentrations. This is based on a decrease in apparent enthalpy of the transition state over Ni nearby Brønsted acid sites. In this context, activation enthalpies of methyl stearate ($n\text{-C}_{17}\text{H}_{35}\text{C}(\text{O})\text{O}-\text{CH}_3$) are lower than those of stearic acid ($n\text{-C}_{17}\text{H}_{35}\text{C}(\text{O})-\text{OH}$), reflecting the difference in the corresponding C-O bond energies. This results in an increase of TOF to a larger extent for methyl stearate than for stearic acid. As the conversion takes place on Ni particles outside the micropores of the support and the electronic density of the metal does not depend on the support, it is concluded that the C-O hydrogenolysis is accelerated on highly active metal sites at the interface with the support. The O of the carbonyl group can be protonated by a Brønsted acid site, decreasing the strength of the adjacent C-O bonds, facilitating the conversion over Ni and resulting in the observed higher rates. This understanding allows to better explain observed effects and to rationally design new catalysts exploiting the cooperation between base metals and Brønsted acid sites.

In the second part, the dehydrogenation of light alkanes over Ga modified H-ZSM-5, being the rate-determining step of light alkane aromatization over industrial catalysts,

was studied (Chapter 4). In literature, the nature of active sites and their concentrations as well as the reasons for an observed synergy between Ga species and Brønsted acid sites are still under debate. Therefore, Ga modified H-ZSM-5 with varying Ga/Al ratio were studied. Three different active sites were determined (Ga^+ , Brønsted acid sites and Ga_2O_3). Ga^+ and Brønsted acid site concentrations change inversely with increasing Ga/Al ratio, as Ga^+ is exchanged with Brønsted acid site protons. At high Ga/Al ratios, at which all protons are already exchanged with Ga^+ , Ga_xO_y clusters form. A maximum in dehydrogenation rate is observed for catalysts with a one to one ratio of Ga^+ and Brønsted acid sites ($\text{Ga/Al} = \frac{1}{2}$). The observed rate is two orders of magnitude faster as on isolated Brønsted acid sites and Ga^+ sites. The well-defined catalyst $\frac{1}{2}$ Ga/Al, containing mainly homotopic Lewis Brønsted acid pairs, allowed us to study the mechanism and the kinetics of the alkane dehydrogenation on these Lewis-Brønsted acid pairs experimentally and *via* DFT calculations. A 0.5 reaction order with respect of propane, implies the dissociative adsorption of propane on zeolite exchange sites, one compensated by H^+ and the other by Ga^+ . The DFT calculations indicate that the Lewis-Brønsted acid site pair carries out alkane dehydrogenation through a bifunctional mechanism in which the Brønsted acid site protonates the Ga^+ to form a $[\text{GaH}]^{2+}$, which is a strong Lewis acid. The $[\text{GaH}]^{2+}$, together with a basic framework oxygen of the Brønsted the assessment of separately in two sequential steps. This Lewis-Brønsted acid pair is found to be much more active than an isolated Ga^+ due to the large increase in Lewis acidity upon protonation of Ga^+ by the Brønsted acid site, which facilitates heterolytic C-H bond activation. The Brønsted acid site also significantly reduces the activation barrier for H_2 elimination by recombination with a hydride compared to the isolated Ga^+ , on which the proton comes from an alkyl C-H bond to simultaneously eliminate propene. These results give fundamental insight into the mechanism of alkane dehydrogenation over Lewis acid site pairs. This allows not only the systematic development of highly active dehydrogenation catalysts, but offers in general a new perspective on cooperative catalysis by Lewis and Brønsted acid sites in heterogeneous catalysis.

5 Supplementary information

5.1 Hydrodeoxygenation of fatty acid esters catalyzed by Ni on nano-sized MFI type zeolites

Table S1: Fatty acid composition in triglyceride mixture of microalgae oil

Fatty acid composition [wt%]												
C ₁₄ :	C ₁₆ :	C ₁₈ :	C ₁₈ :	C ₁₈ :	C ₂₀ :	C ₂₀ :	C ₂₂ :	C ₂₂ :	C ₂₂ :	C ₂₂ :	C ₂₄ :	Stero
0	0	2	1	0	4	0	6	4	1	0	0	1
0.04	4.41	56.2	32.2	4.41	0.07	0.43	0.13	0.19	0.97	0.44	0.36	0.12

Nomenclature in lipid numbers: C_x:y:x number of carbon atoms in fatty acid chain; y number of double bonds in fatty acid chain

Crude microalgae oil was obtained from Verfahrenstechnik Schwedt GmbH.

Table S2. Diameter, dispersion, and concentration of accessible Ni atoms on different materials as determined from XRD, TEM, and hydrogen chemisorption.

Catalyst	XRD		
	Diameter	Dispersion	Accessible Nickel atoms
	[nm]	[%]	[μ mol/g]
Ni/H-ZSM-5	10.5	9.6	157
Ni/Silicalite 1	10.0	10.1	174
Ni/n-H-ZSM-5	3.6	28.0	445
Ni/n-Silicalite 1	2.6	38.8	668
Catalyst	TEM		
	Diameter	Dispersion	Accessible Nickel atoms
	[nm]	[%]	[μ mol/g]
Ni/H-ZSM-5	8.8	11.5	187
Ni/Silicalite 1	8.0	12.6	218

Ni/n-H-ZSM-5	2.3	43.7	693
Ni/n-Silicalite 1	2.4	41.9	721
Hydrogen chemisorption			
Catalyst	Diameter	Dispersion	Accessible Nickel atoms
	[nm]	[%]	[$\mu\text{mol/g}$]
Ni/H-ZSM-5	12.9	7.9	128
Ni/Silicalite 1	8.4	12.0	207
Ni/n-H-ZSM-5	4.5	22.0	349
Ni/n-Silicalite 1	4.7	21.5	370

XRD: particle diameters were calculated based on deconvoluted XRD signals for the (111) plane reflection of Ni *via* the Scherrer equation¹, where τ is the particle size in Å, K is the shape factor (0.9 for spherical particles used), β is the line broadening at half the maximum intensity of the reflection $[2\theta]$ after subtraction of the instrumental line broadening (0.1 for used instrument), Λ is the X-Ray wavelength of the used cathode and θ is the Bragg angle of the signal.

$$\tau = \frac{K \lambda}{\beta \cos\theta} \quad (1)$$

TEM: Particle diameters were calculated based on at least 300 particles obtained from at least 5 different areas of the catalyst on the carbon grid. The dispersion D based on the mean particle size was calculated following formula², with v_{Ni} being the volume occupied by a Ni atom (10.95 \AA^3) and a_{Ni} is the surface area of Nickel atom (6.51 \AA^2) and d_{VA} is the mean particle size.

The concentration of accessible Ni atoms was calculated based on the amount of Ni on the catalyst per gram and the dispersion based on formula (3).

$$D = 6 \frac{(v_{\text{Ni}}/a_{\text{Ni}})}{d_{\text{VA}}} \quad (2)$$

$$c_{\text{accessible Ni atoms}} = D \frac{(m_{\text{Ni}}/M_{\text{Ni}})}{m_{\text{catalyst}}} \quad (3)$$

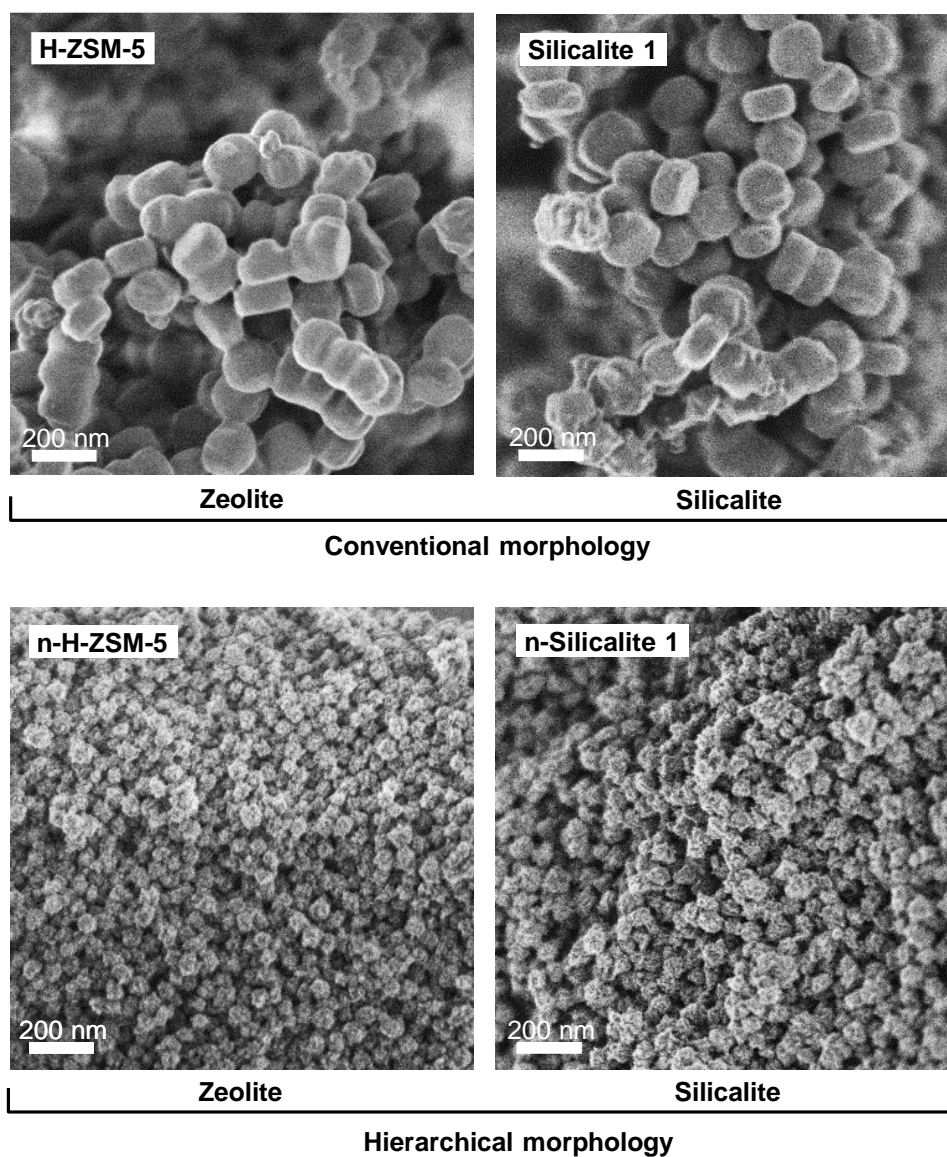


Figure S1. Representative micrographs of (n)-H-ZSM-5 and (n)-Silicalite 1 materials.

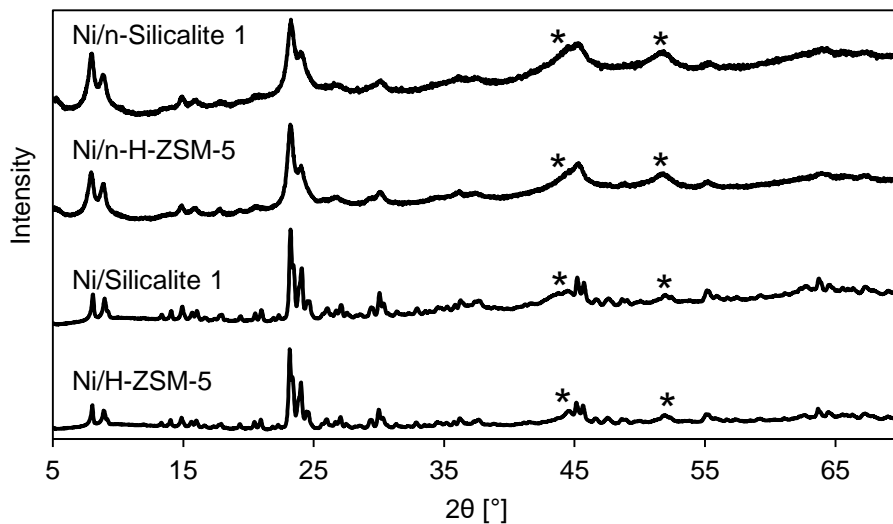


Figure S2. X-ray diffractograms of the catalysts based on (n)-H-ZSM-5 and (n)-Silicalite 1 materials. Nickel reflections are highlighted with a star (*).

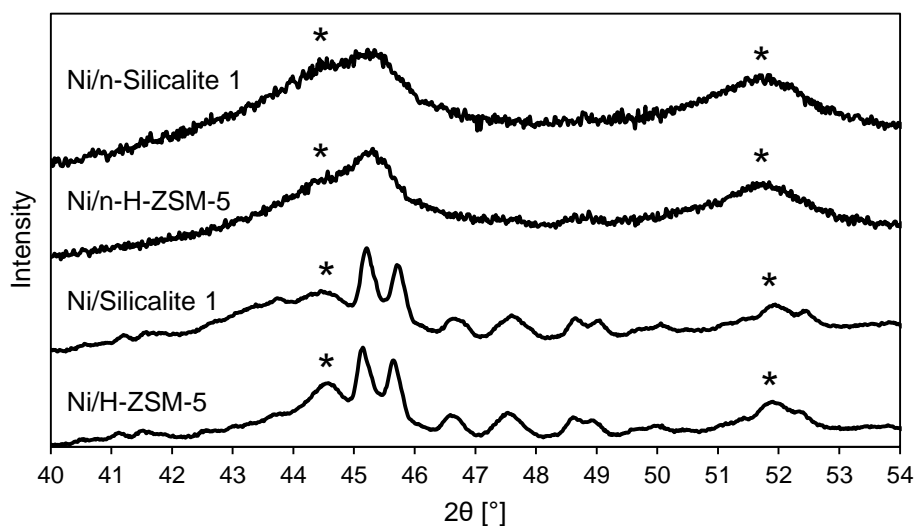


Figure S3. Detail of X-ray diffractograms in the region of Ni reflections of the catalysts based on (n)-H-ZSM-5 and (n)-Silicalite 1 materials. Nickel reflections are highlighted with a star (*).

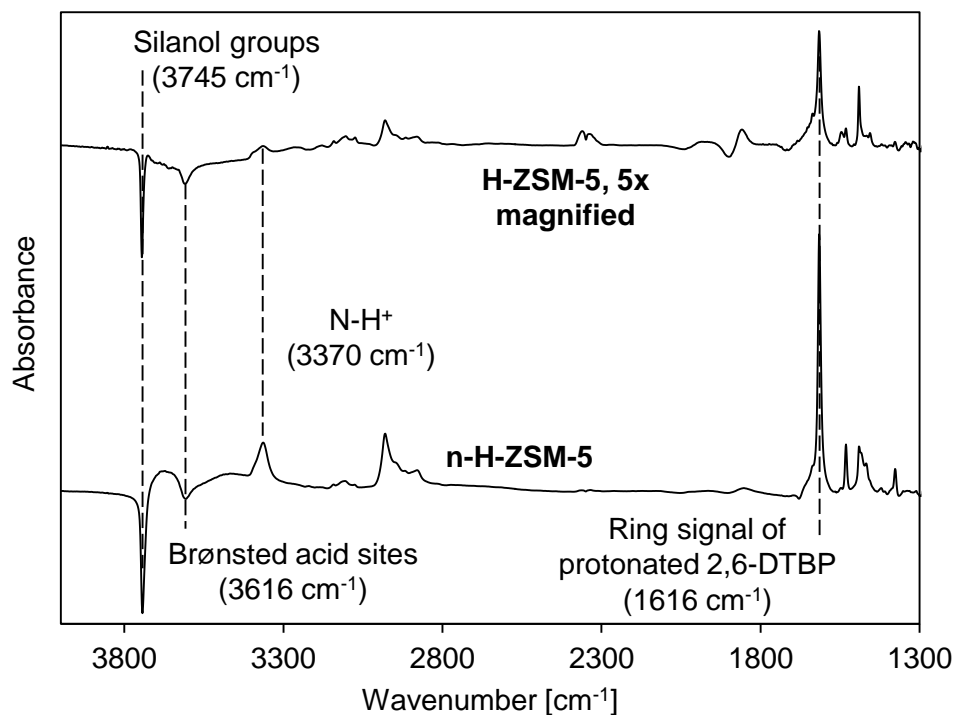


Figure S4. Changes in IR spectra after adsorption of 2,6-di-tert-butyl-pyridine (2,6-DTBP) at 423 K, 0.01 kPa and outgassing for 1 h in vacuum. The characteristic bands at 3370 cm⁻¹ (N-H⁺ vibration) and 1616 cm⁻¹ (C=C vibration) appear from 2,6-DTBP interaction with the zeolite.

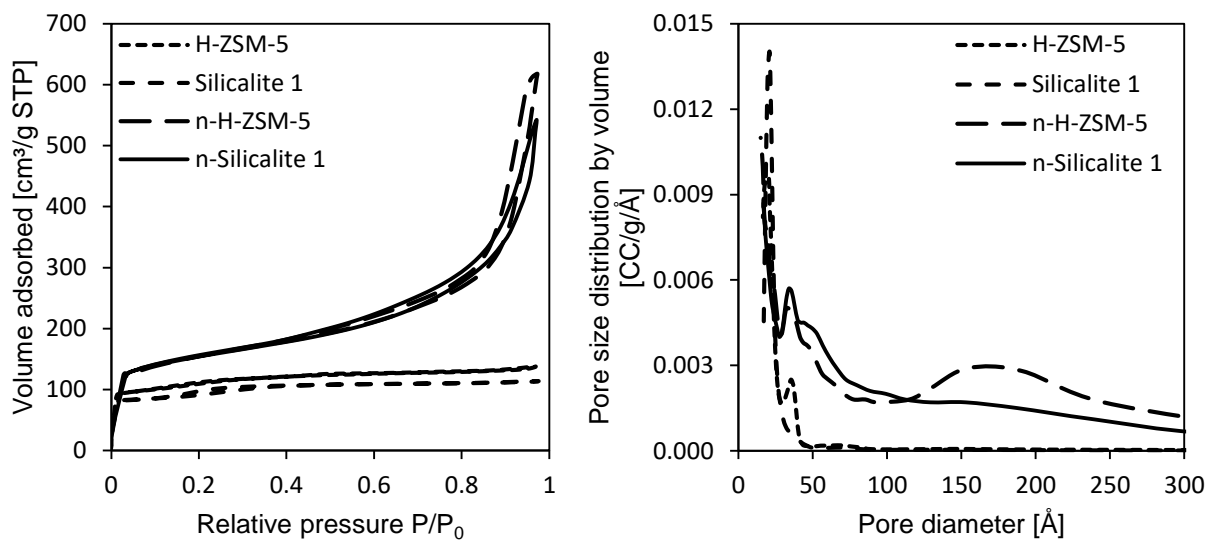


Figure S5. N₂-physorption isotherms and pore size distributions of unloaded parent materials.

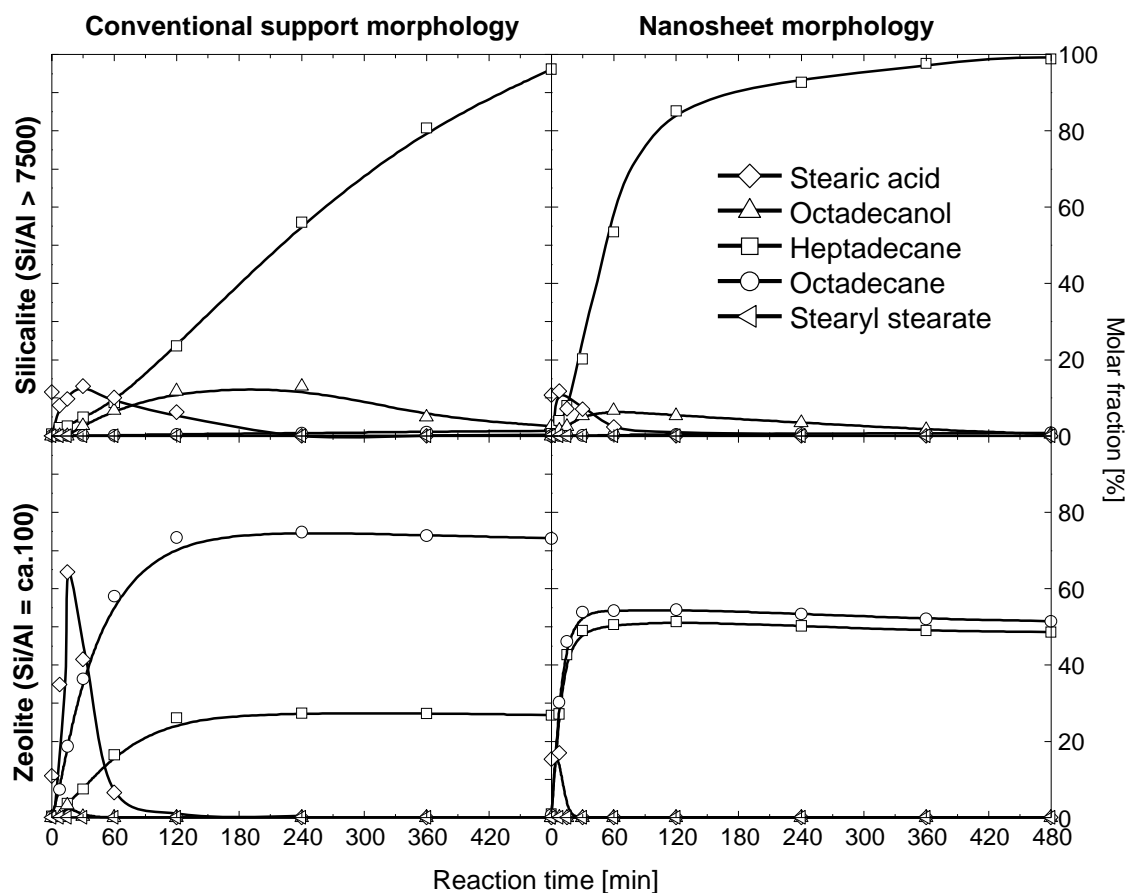


Figure S6. Evolution of the concentrations of reaction products of algae oil conversion over time.

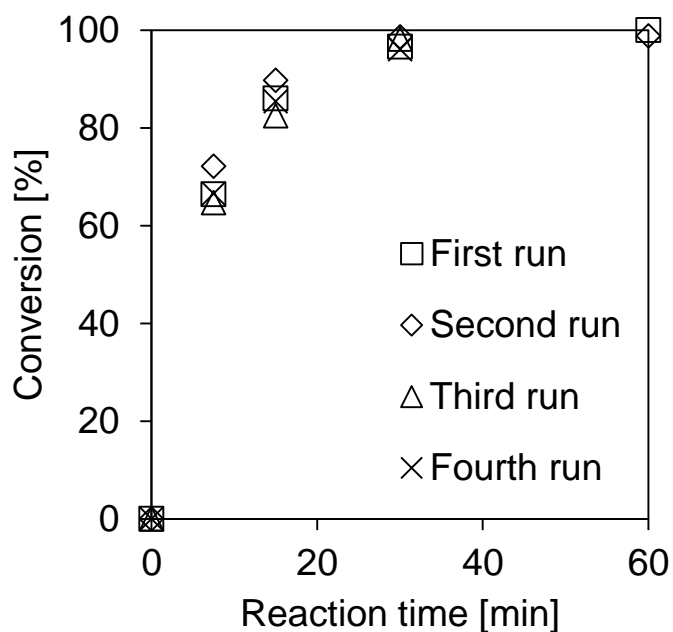


Figure S7. Evolution of algae oil conversion over time for four consecutive recycling experiments of Ni/n-H-ZSM-5.

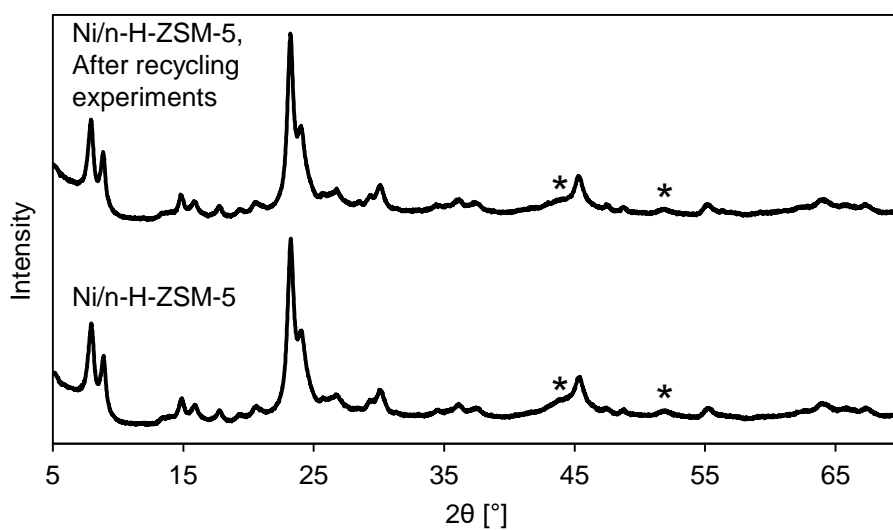


Figure S8. X-Ray diffractograms of Ni/n-H-ZSM-5 before and after four consecutive recycling experiments. Nickel reflections are highlighted with a star (*).

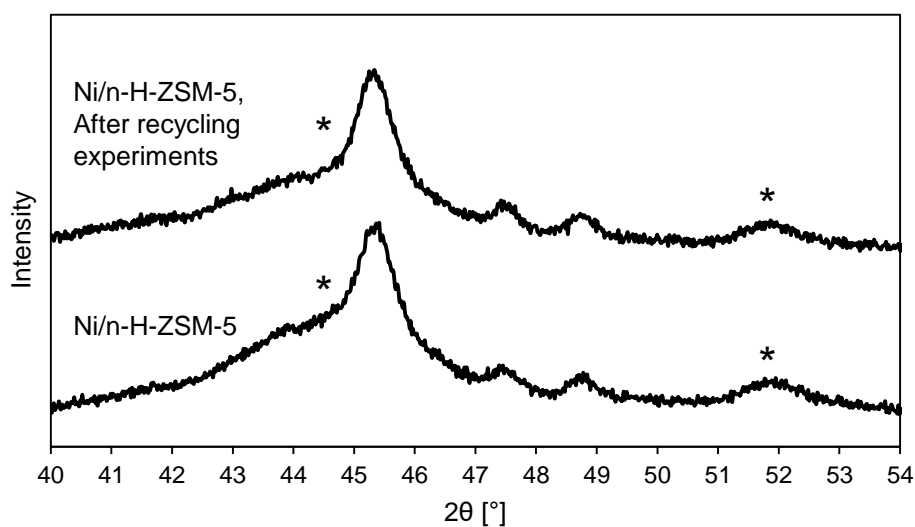


Figure S9. Detail of X-ray diffractograms in the region of Ni reflections of Ni/n-H-ZSM-5 before and after four consecutive recycling experiments. Nickel reflections are highlighted with a star (*).

References

1. Scherrer, P., *Nachr. Ges. Wiss.* **1918**, (2), 96 - 100.
2. G. Ertl, H. K., J. Weitkamp, *Handbook of Heterogeneous Catalysis*. Wiley VCH: Weinheim, 2008; Vol. 3.

5.2 Ni-catalyzed C-O hydrogenolysis enhanced by the Brønsted acid sites of Ni/H-ZSM-5

5.2.1 Characterization

The silicon to aluminum ratios of the parent materials, the AHFS treated supports and the Ni loaded catalysts are listed in **Fehler! Verweisquelle konnte nicht gefunden werden..** The Si/Al ratios of the parent materials were close to the ratios in the synthesis solutions (varied from 90 to 200). The AHFS treatment caused an increase of the Si/Al ratio of the materials. The lower the Al concentration of the materials, the more severe the dealumination was (0.7%, 4%, 7% increase of Si/Al ratio for H-ZSM-5 100, H-ZSM-5 180 and H-ZSM-5 250, respectively) as previously reported¹.

During the Ni loading, the Si/Al ratio increased further due to dealumination. This was already observed and intensively studied for Ni deposited on HBEA and high surface area SiO₂ support materials². The dissolution of some support materials was also evidenced by the N₂ physisorption isotherms (vide infra).

Table S1. Silicon to aluminum molar ratios of supports in parent support material, AHFS treated support materials and in Ni loaded and reduced catalyst.

Si/Al	Synthesis gel solution	Parent material	Ni loaded parent material	AHFS treated material	Ni loaded AHFS treated material
H-ZSM-5 100	90	90	95	91	102
H-ZSM-5 180	150	162	170	168	180
H-ZSM-5 250	200	193	206	207	250
Silicalite 1	No Al ^a	No Al ^a	No Al ^a	No Al ^a	No Al ^a

^aSi/Al > 7000.

Table S2: Textural properties of AHFS treated supports and the corresponding catalysts.

Sample	Total pore volume [cm ³ · g ⁻¹]	Mesopore volume [cm ³ · g ⁻¹]	Micropore volume [cm ³ · g ⁻¹]
H-ZSM-5 100	0.23	0.049	0.17
H-ZSM-5 180	0.23	0.029	0.17
H-ZSM-5 250	0.25	0.043	0.17
Silicalite 1	0.21	0.033	0.14
Ni/H-ZSM-5 100	0.28	0.11	0.16
Ni/H-ZSM-5 180	0.27	0.058	0.15
Ni/H-ZSM-5 250	0.29	0.085	0.13
Ni/Silicalite 1	0.22	0.062	0.12

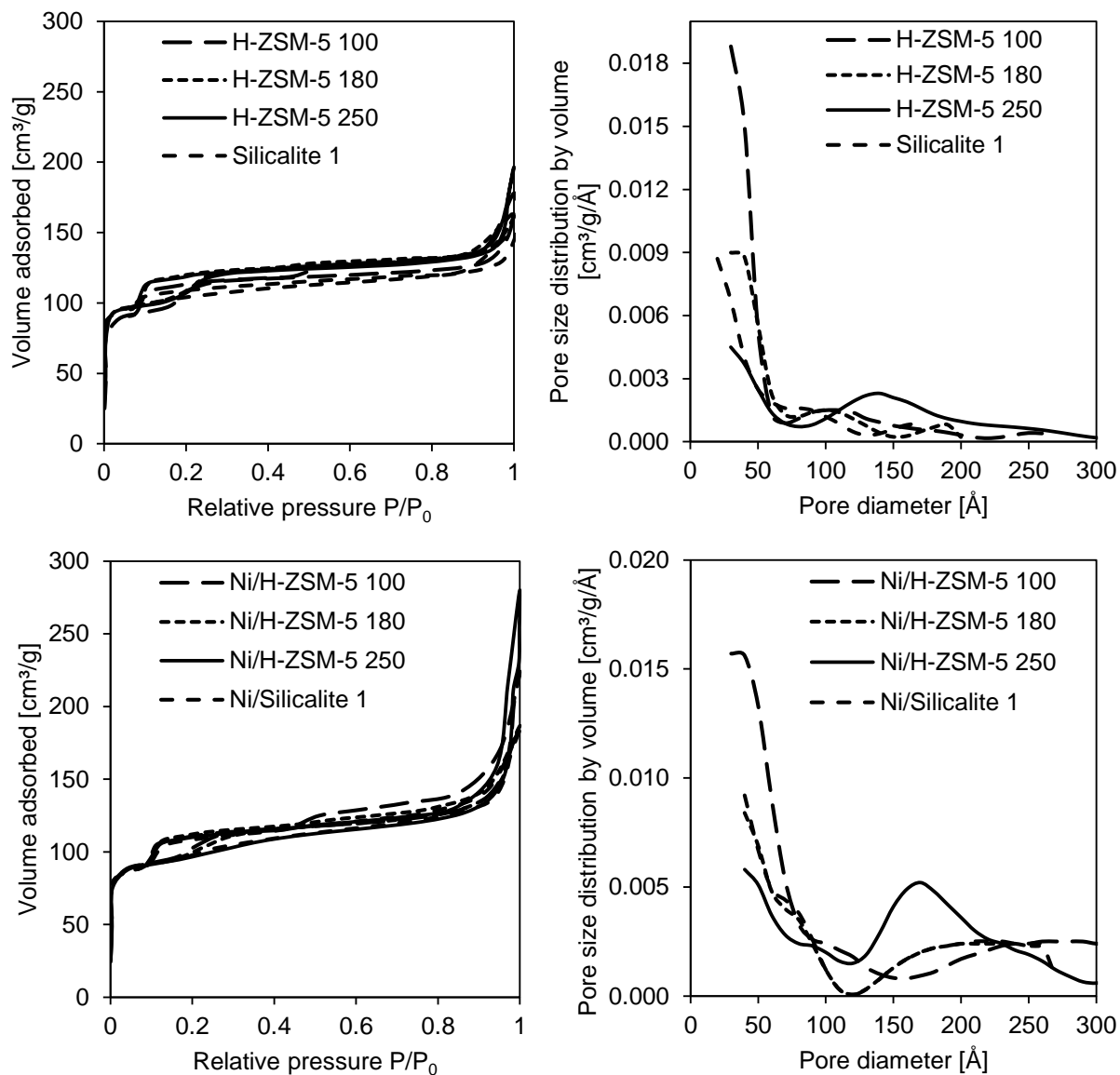


Figure S1. Adsorption-desorption isotherms and pore size distributions of the AHFS treated materials and the corresponding catalysts.

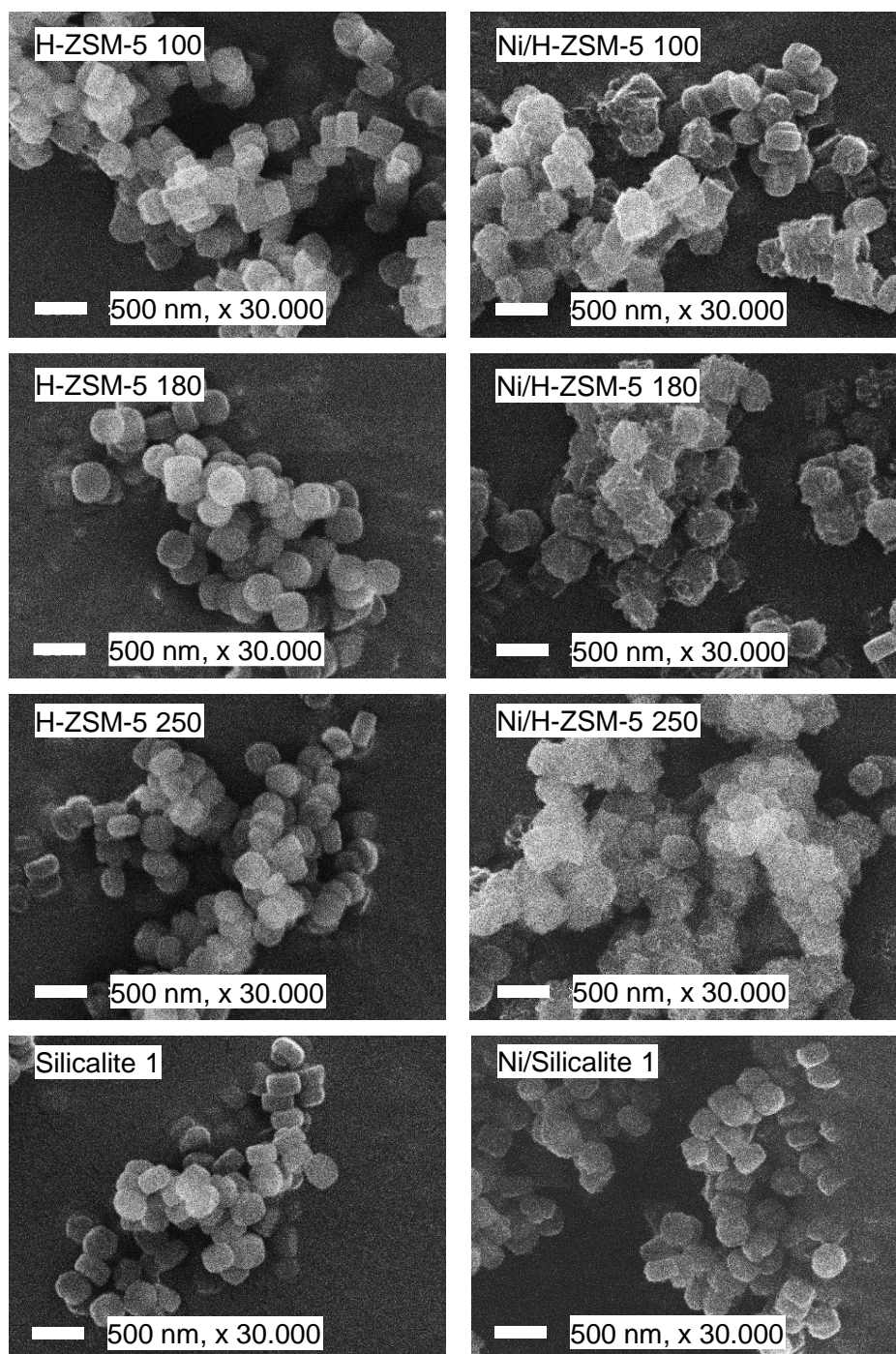


Figure S2: Representative SEM images of parent materials and catalysts with different silicon to aluminum ratios.

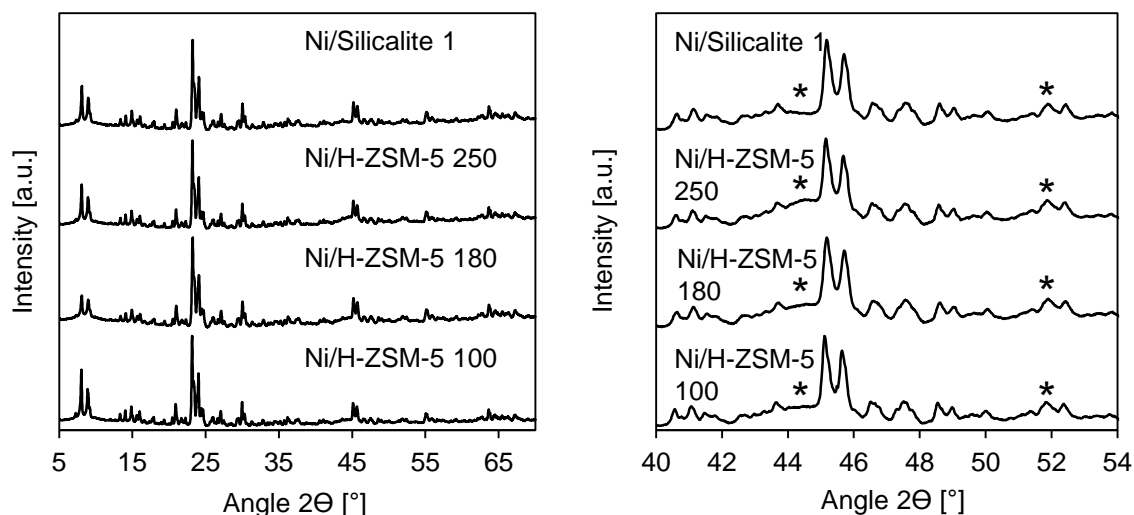


Figure S3. XRD patterns of Ni loaded catalysts supported on AHFS treated supports.

XRD measurement: crystal sizes were calculated based on deconvoluted XRD signals of the (111) plane reflection of Ni using the Scherrer equation³:

$$\tau = \frac{K \lambda}{\beta \cos \theta}$$

Where τ is the particle size in Å, K is the shape factor (0.9 for spherical particles), β is the line broadening at half the maximum intensity of the reflection [2θ] after subtraction of the instrumental line broadening (0.1 for the used instrument), λ is the X-Ray wavelength of the used cathode and θ is the Bragg angle of the signal.

TEM measurement: particle diameters were calculated based on at least 300 particles obtained from at least 5 different areas of the catalyst on the carbon grid. The dispersion D based on the mean particle size was calculated on the following formula⁴:

$$D = 6 \frac{(v_{Ni}/a_{Ni})}{d_{VA}}$$

Where v_{Ni} is the volume occupied by a Ni atom (10.95 Å³) and a_{Ni} is the surface area of Ni atom (6.51 Å²) and d_{VA} is the mean particle size.

The concentration of accessible Ni atoms was calculated based on the amount of Ni on the catalyst per gram and the dispersion based on the following formula:

$$c_{\text{accessible Ni atoms}} = D \frac{(m_{\text{Ni}}/M_{\text{Ni}})}{m_{\text{catalyst}}}$$

Ratio of accessible Ni atoms to Ni atoms at the perimeter of Ni particle and support:

The quantity of accessible Ni atoms on a half-sphere being the surface area of the half-sphere divided by the surface area a_{Ni} occupied by a Ni atom on a polycrystalline surface $(6.51 \text{ \AA}^2)^3$.

$$n_{\text{accessible Ni atoms halfsphere}} = \frac{\pi d_{\text{VA}}^2}{2 a_{\text{Ni}}}$$

The quantity of Ni atoms at the perimeter of a Ni particle and the support is:

$$n_{\text{accessible Ni atoms perimeter}} = \frac{\pi d_{\text{VA}}}{d_{\text{Ni}}}$$

with d_{Ni} being the diameter of a Ni atom (2.82 Å) and d_{VA} being the mean particle size. Therefore, the ratio of accessible Ni atoms to Ni atoms at the perimeter of Ni particle and support is:

$$\frac{n_{\text{accessible Ni atoms halfsphere}}}{n_{\text{accessible Ni atoms perimeter}}} = \frac{d_{\text{VA}} d_{\text{Ni}}}{2 a_{\text{Ni}}}$$

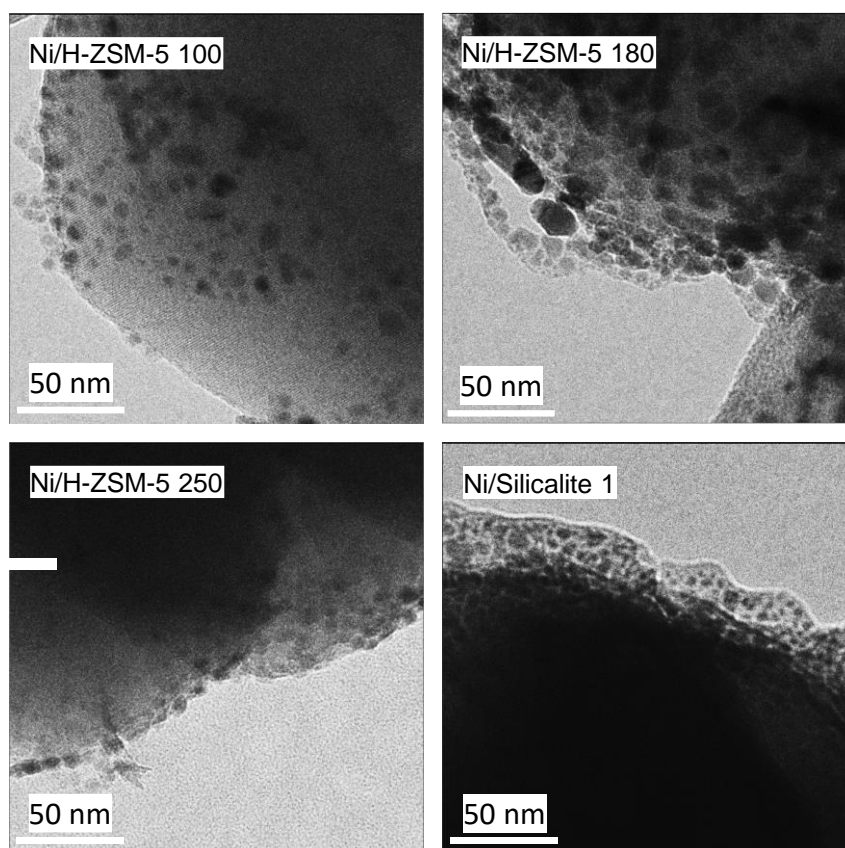


Figure S4. TEM images of catalysts.

Table S3. Ni content of catalysts and corresponding Ni crystal size/dispersion determined by H_2 chemisorption and TEM.

Sample	Ni [wt%]	H_2 chemisorption		TEM		XRD	
		d Ni [nm]	Dispersion [%]	d Ni [nm]	Dispersion [%]	d Ni [nm]	Dispersion [%]
Ni/H-ZSM-5 100	7.76	11.4	8.89	7.43 (± 2.66)	10.61	8.2	12.1
Ni/H-ZSM-5 180	7.83	12.7	7.95	10.0 (± 5.17)	6.34	8.3	12.0
Ni/H-ZSM-5 250	7.78	13.4	7.57	8.81 (± 3.47)	8.49	9.2	10.8
Ni/Silicalite 1	7.92	8.08	12.52	7.07 (± 2.42)	11.43	6.1	16.3

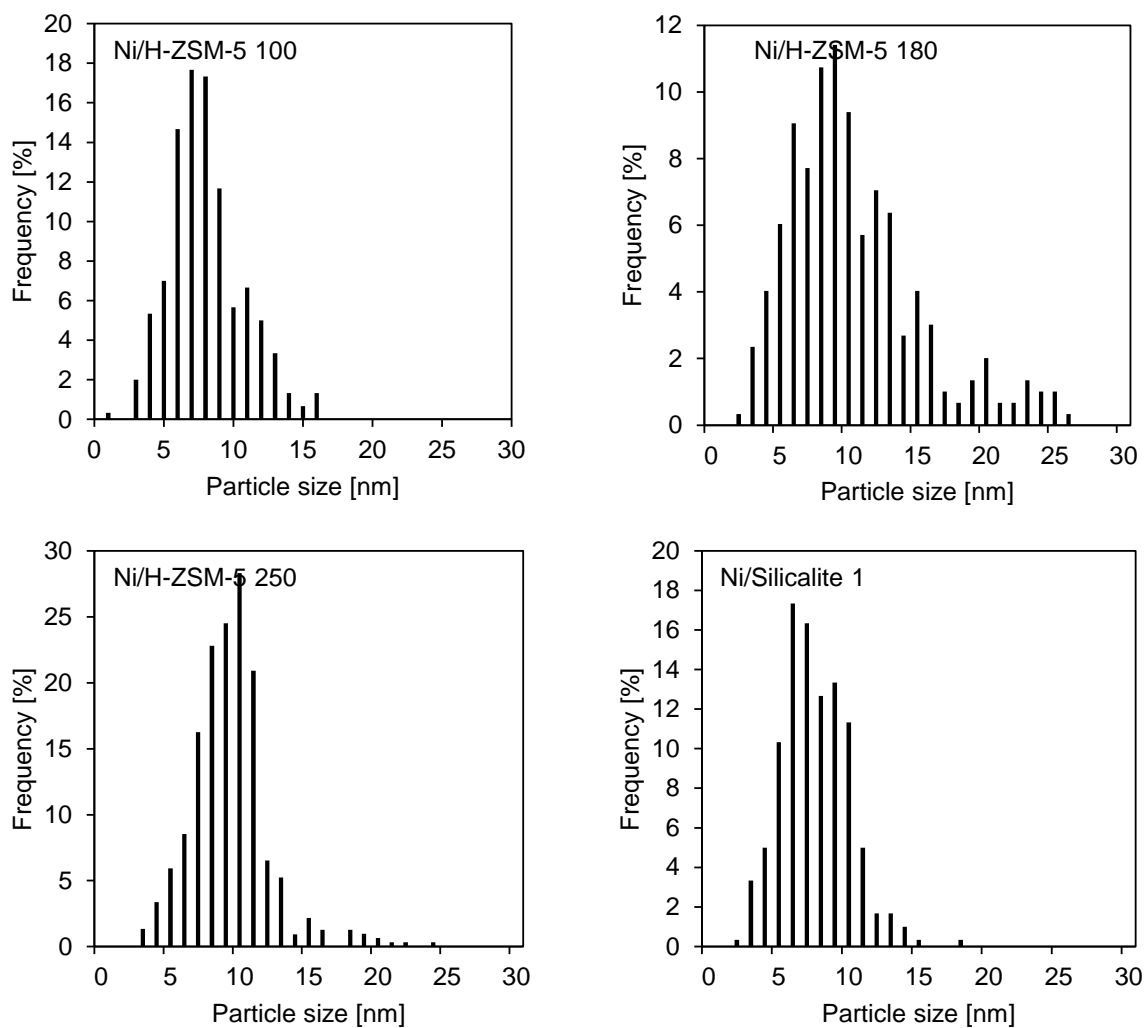


Figure S5. Ni particle size distribution based derived from TEM measurements of catalysts.

Table S4. Acid properties of support materials.

Sample	Si/Al	Total acid sites		Weak acid sites		Strong acid sites	
		LAS	BAS	WLAS	WBAS	SLAS	SBAS
H-ZSM-5 100	91	10	115	2	19	8	96
H-ZSM-5 180	168	6	72	2	8	4	64
H-ZSM-5 250	207	3	55	1	13	2	42
Silicalite-1	-	1	1	0	0	0	0

On unreduced Ni catalysts, a signal was detected at 3680 cm^{-1} , which was assigned to the O-H bridging vibration of NiOH (1). The NiOH is assumed to form on the reduced Ni particles due to contact to atmospheric oxygen or air moisture. On the in situ reduced catalysts however, this signal is not observed, showing that the in situ Ni is fully reduced.

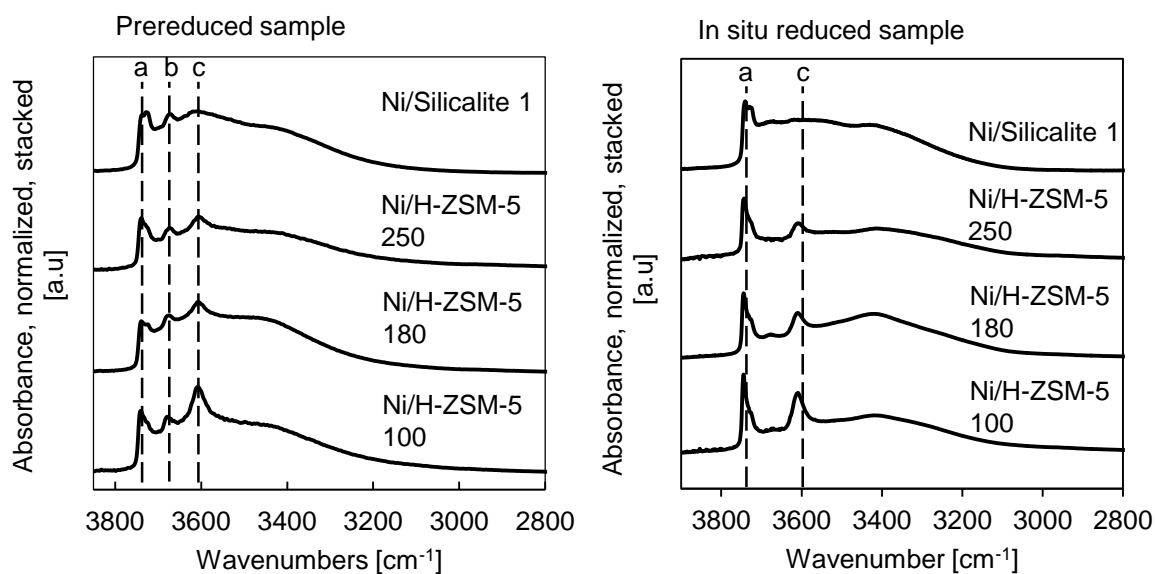


Figure S6. IR spectra of the different catalysts after activation (1h at 723 K under vacuum 10^{-6} mbar) normalized to the weight of the wafer. The signals of the bridging vibrations of the OH of Si-OH (a), NiOH (b) and AlOHSi (c) are marked with the dashed lines. The Ni/Silicalite catalyst does not exhibit a signal for bridging vibrations of the OH of AlOHSi.

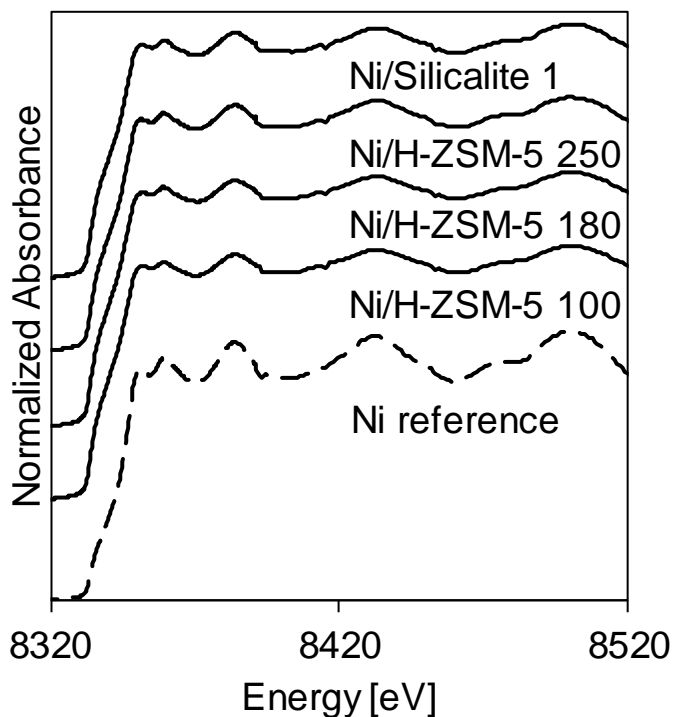


Figure S7. XANES spectra of different supported Ni catalysts and metallic Ni reference.

5.2.2 Reaction kinetics

Eyring Polanyi equation

Apparent activation enthalpies and entropies were calculated based on the Eyring Polanyi equation:

$$k = \frac{k_B \cdot T}{h} \cdot e^{-\frac{\Delta G^\ddagger}{R \cdot T}}$$

with the reaction rate constant k , the absolute temperature T , the gas constant R , the Boltzmann constant k_B , the Planck's constant h and the Gibbs energy of activation ΔG^\ddagger . The equation can be extended via the Gibbs-Helmholtz equation to the following form:

$$k = \frac{k_B \cdot T}{h} \cdot e^{\frac{\Delta S^\ddagger}{R}} \cdot e^{-\frac{\Delta H^\ddagger}{R \cdot T}}$$

The linear form of this equation is the following:

$$\ln \frac{k}{T} = \frac{\Delta H^\ddagger}{R} \cdot \frac{1}{T} + \ln \frac{k_B}{h} + \frac{\Delta S^\ddagger}{R}$$

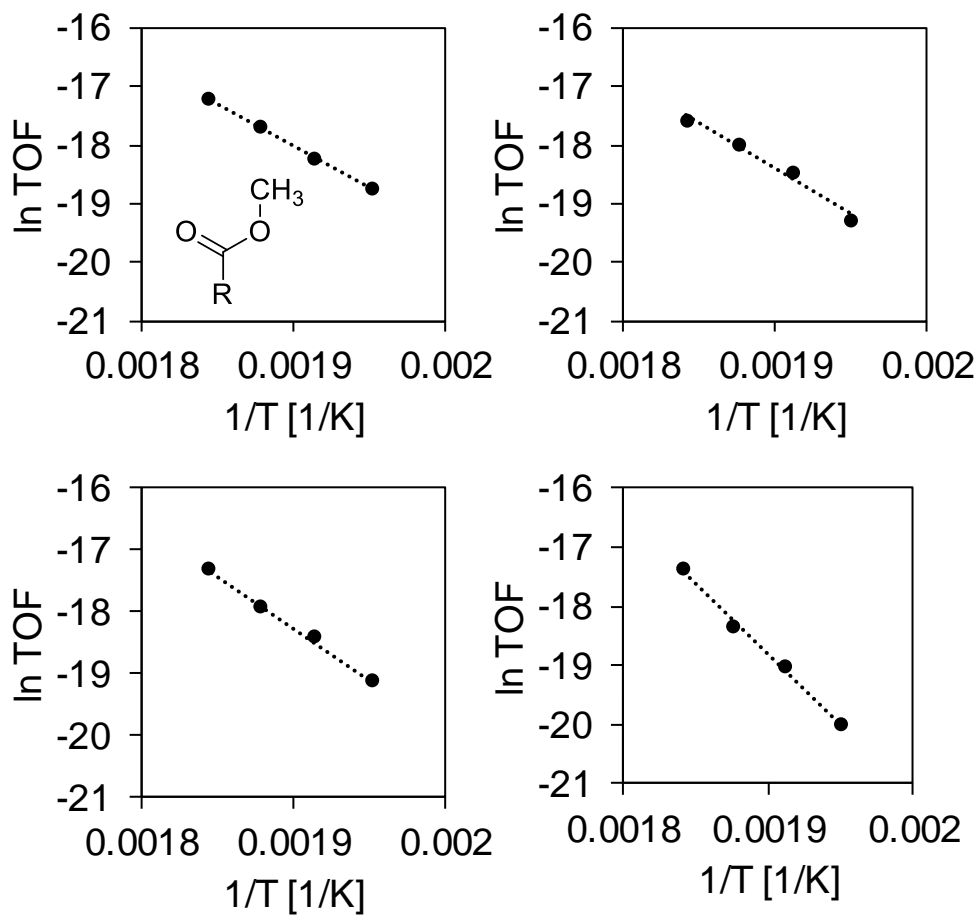


Figure S8. Eyring plots of the different catalysts for the conversion of methyl stearate in the range of 513 - 543 K.

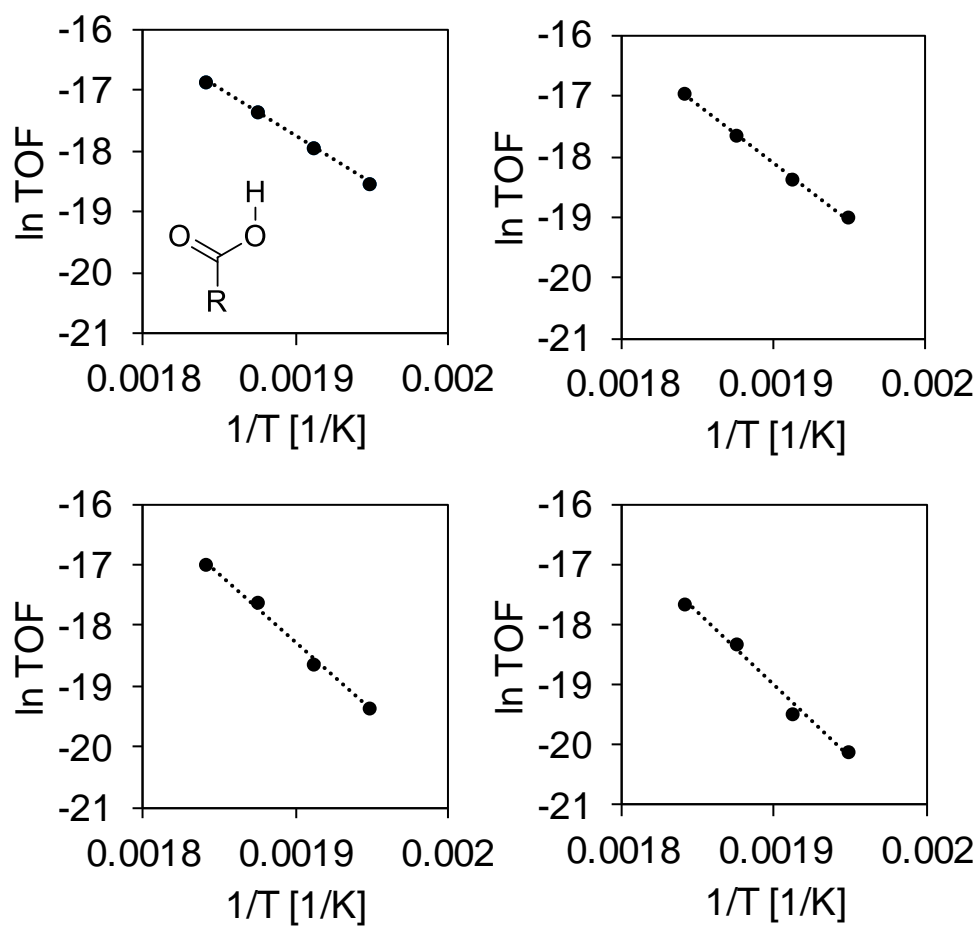


Figure S9. Eyring plots of the different catalysts for the conversion of stearic acid in the range of 513 - 543 K.

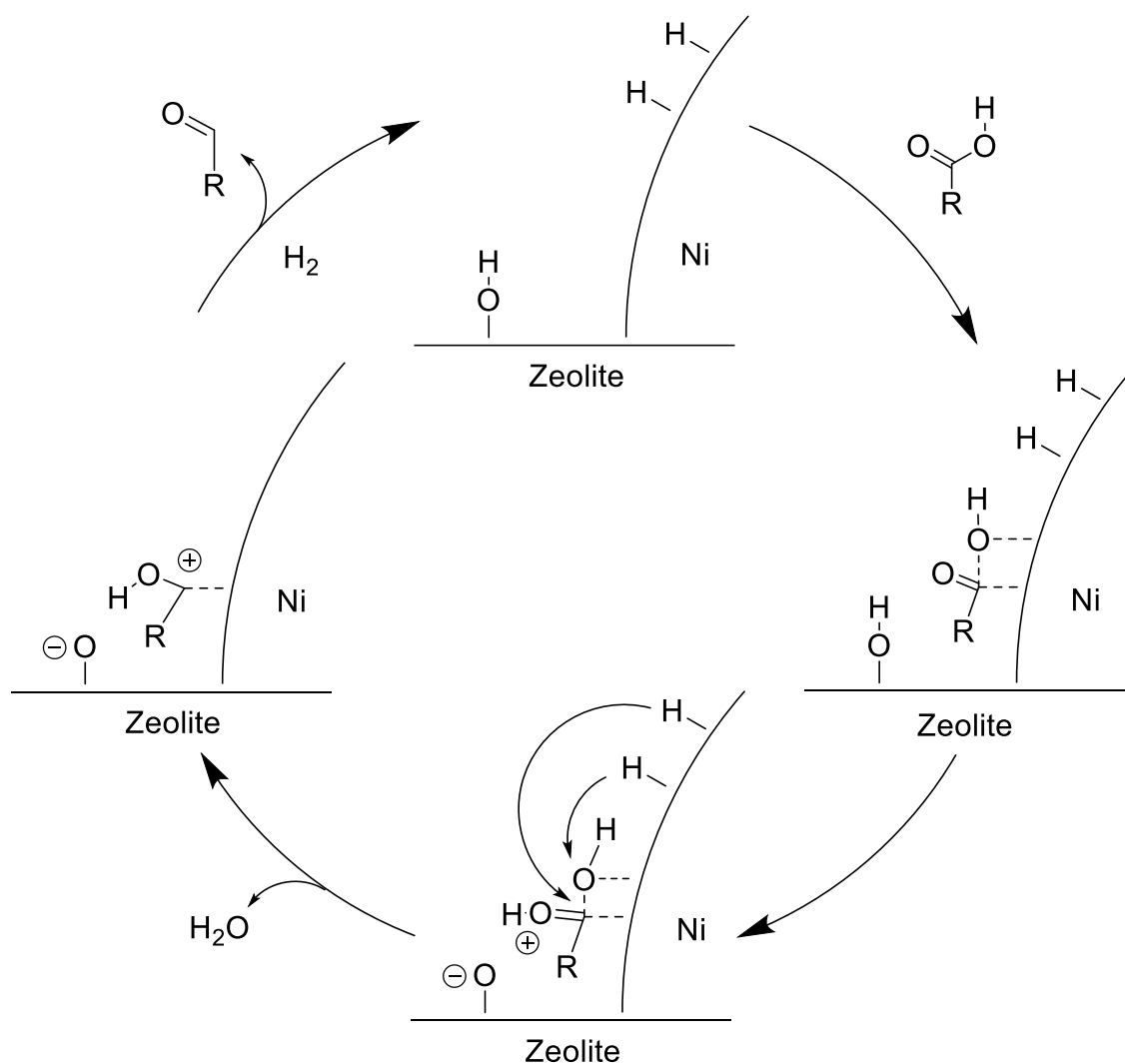


Figure S10. Proposed reaction mechanism for the C-O hydrogenolysis of methyl stearate over Ni facilitated by the protonation of the substrate by a Brønsted acid site.

1. Triantafillidis, C. S.; Vlessidis, A. G.; Nalbandian, L.; Evmiridis, N. P., *Microporous and Mesoporous Materials* 2001, 47 (2–3), 369–388.
2. Nares, R.; Ramírez, J.; Gutiérrez-Alejandre, A.; Louis, C.; Klimova, T., *J. Phys. Chem. B* 2002, 106 (51), 13287–13293.
3. Scherrer, P., *Nachr. Ges. Wiss.* **1918**, (2), 96 - 100.
4. G. Ertl, H. K., J. Weitkamp, *Handbook of Heterogeneous Catalysis*. Wiley VCH: Weinheim, 2008; Vol. 3.

5.3 Lewis Brønsted acid pairs in Ga/H-ZSM-5 for the dehydrogenation of light alkanes

5.3.1.1 Elemental analysis

Table S1: Ga/Al ratios and Ga concentrations on synthesized catalysts.

Catalyst	Target Ga/Al	Real Ga/Al	Target Ga [ppm]	Real Ga [ppm]	Deviation [%]
H-ZSM-5	-	-	0.00	0.00	-
1/3 Ga/Al Ga/H-ZSM-5	0.333	0.344	8	8.26	3.25
1/2 Ga/Al Ga/H-ZSM-5	0.5	0.498	12	11.95	4.18
3/4 Ga/Al Ga/H-ZSM-5	0.75	0.752	18	18,05	0.27
1 Ga/Al Ga/H-ZSM-5	1	1.05	24	25,13	4.50
3/2 Ga/Al Ga/H-ZSM-5	1.5	1.49	36	35.81	0.53
Ga ₂ O ₃ /SiO ₂	1.1 wt%Ga	1.11 wt% Ga	12	12.14	1.15

5.3.1.2 Analysis of coordination symmetry of Al

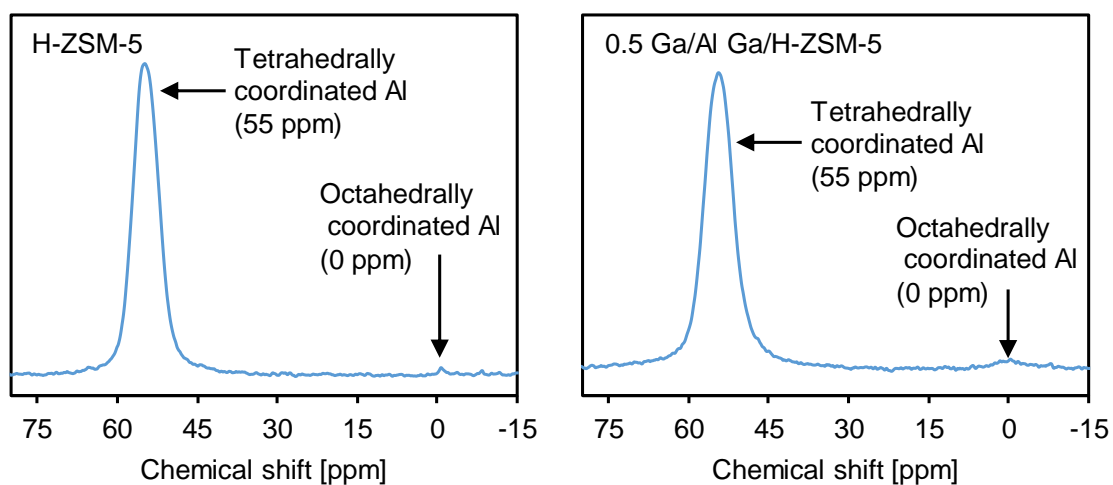


Figure S1: Determination of tetrahedrally coordinated Al (framework Al) and octahedrally coordinated Al (EFAI) via ^{27}Al MAS-NMR. Octahedrally coordinated Al (EFAI) represents 1% and 2% of all the Al in the H-ZSM-5 and the $\frac{1}{2}$ Ga/Al Ga/H-ZSM-5 sample, respectively.

5.3.1.3 Reduction and oxidation cycles on $\frac{1}{2}$ Ga/Al Ga/H-ZSM-5

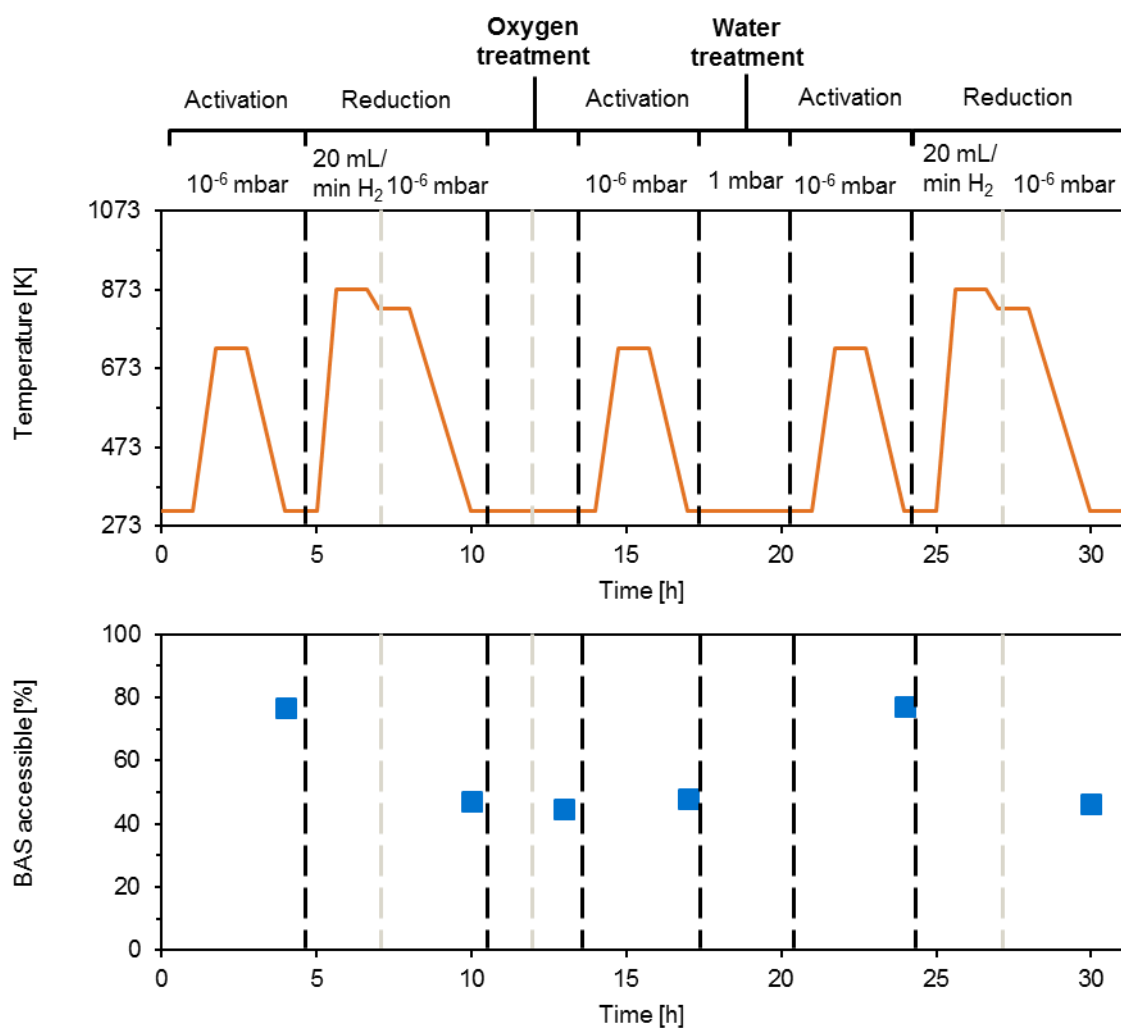


Figure S2: In-situ examination of Brønsted acid site coverage (via IR spectroscopy) for $\frac{1}{2}$ Ga/Al Ga/H-ZSM-5 catalyst. A) Treatment step and B) BAS coverage.

5.3.1.4 IR spectroscopy of pyridine adsorbed on Ga₂O₃/SiO₂

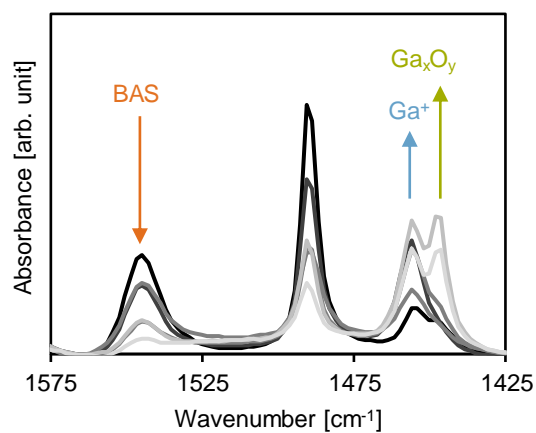


Figure S3. In situ IR spectra of adsorbed pyridine and its interaction with Lewis and Brønsted acid sites of catalysts with different Ga/Al ratios.

5.3.1.5 XANES of Ga modified catalysts

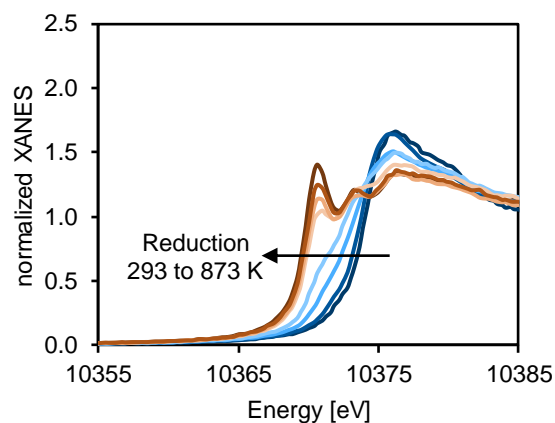


Figure S4: Change of edge energy of Ga species during reduction of Ga₂O₃/SiO₂.

5.3.1.6 Measuring the reduction stoichiometry over $\frac{1}{2}$ Ga/Al Ga/H-ZSM-5

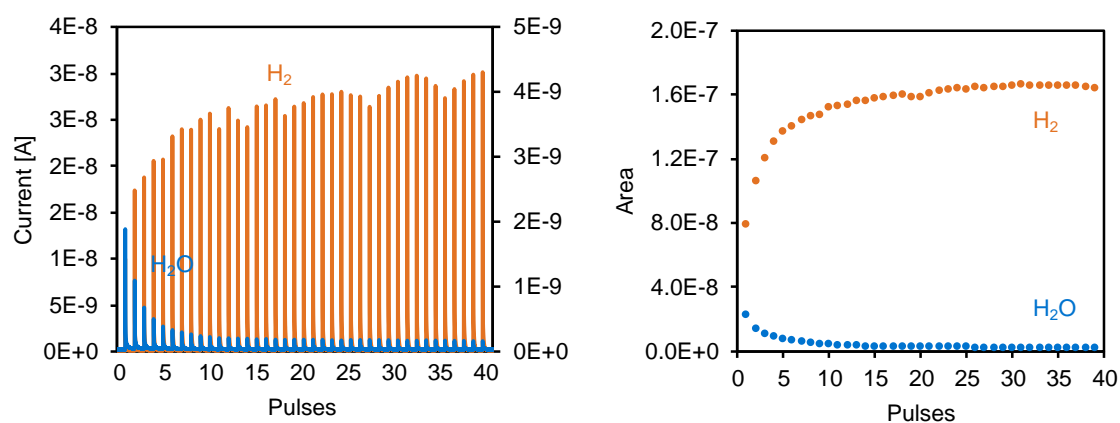


Figure S5: Following stoichiometry of stepwise reduction via MS of 0.5 Ga/Al Ga/H-ZSM-5.

5.3.1.7 Kinetics of dehydrogenation over Ga modified H-ZSM-5 -

Table S2: Overall reaction rate of propane conversion and corresponding selectivities to cracking and dehydrogenation products on Ga modified zeolitic and oxidic materials at 783 K

Catalyst	Overall reaction rate [$\times 10^7$ [mol \cdot (g \cdot s) $^{-1}$]	Selectivity cracking [%]	Selectivity dehydrogenation [%]
H-ZSM-5	0.11	63.6	36.4
$\frac{1}{3}$ Ga/Al	3.18	7.2	92.8
$\frac{1}{2}$ Ga/Al	16.3	4.9	95.1
$\frac{3}{4}$ Ga/Al	1.46	5.5	94.5
1 Ga/Al	0.99	4.0	96.0
$\frac{3}{2}$ Ga/Al	0.38	2.6	97.4
Ga ₂ /SiO ₂	0.13	-	100.0

5.3.1.8 Reaction order of propane dehydrogenation over H-ZSM-5 and $\frac{1}{2}$ Ga/Al Ga/H-ZSM-5

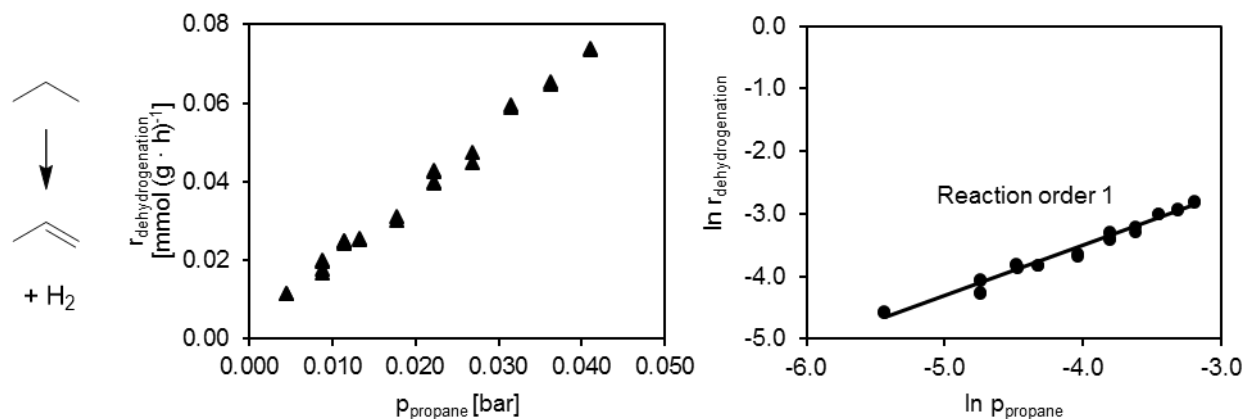


Figure S6: Determination of reaction order of propane dehydrogenation over H-ZSM-5 with propane partial pressures ranging from 0.25 – 45 mbar at 783 K.

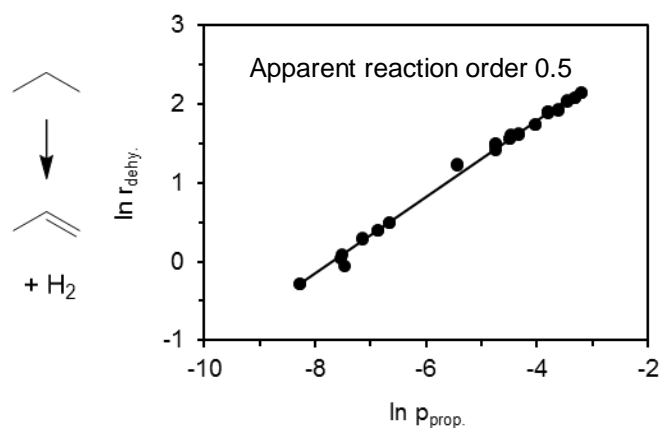


Figure S7: Determination of reaction order of propane dehydrogenation over Ga/H-ZSM-5 with propane partial pressures ranging from 0.25 – 45 mbar at 783 K.

5.3.1.9 Eyring plots of alkane dehydrogenation over H-ZSM-5, $\frac{1}{2}$ Ga/Al Ga/H-ZSM-5 and Ga₂O₃/SiO₂

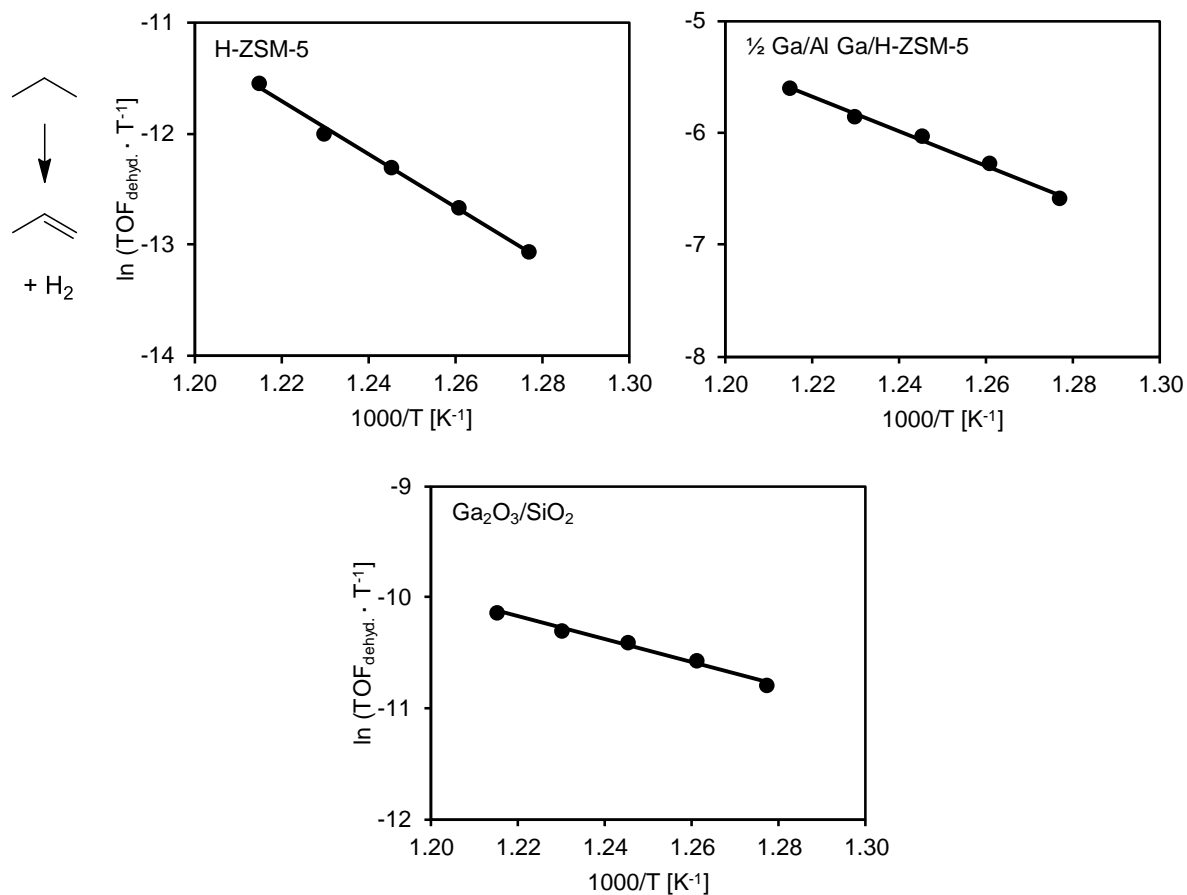


Figure S8: Eyring plots of propane dehydrogenation over H-ZSM-5, $\frac{1}{2}$ Ga/Al Ga/H-ZSM-5 and Ga₂O₃/SiO₂. TOF determined in a temperature range from 783 – 823 K.

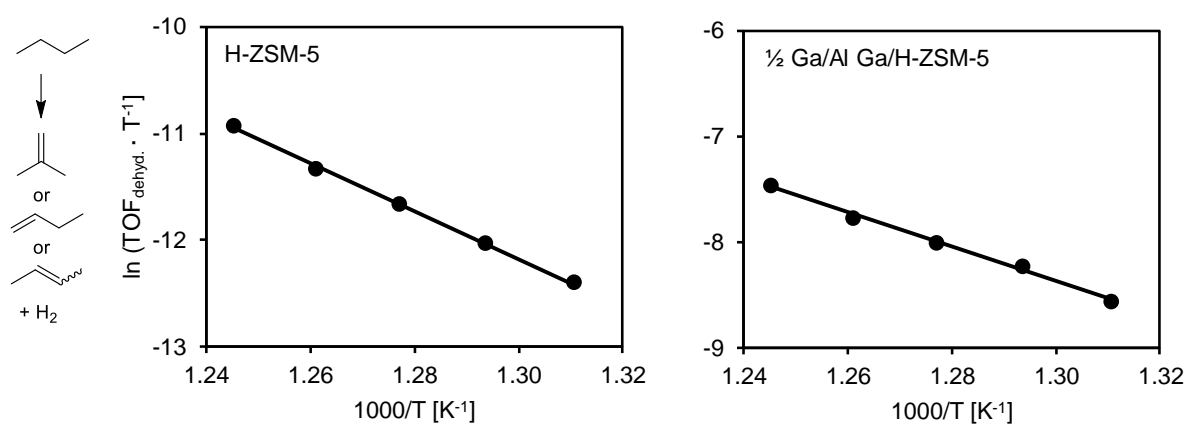


Figure S9: Eyring plots of butane dehydrogenation over H-ZSM-5, $\frac{1}{2}$ Ga/Al Ga/H-ZSM-5. TOF determined in a temperature range from 763 – 803 K.

6 List of publications

6.1 Publications in peer-reviewed journals

- Simultaneous hydrodenitrogenation and hydrodesulfurization on unsupported Ni-Mo-W sulfides
S. Albersberger, J. Hein, M. W. Schreiber, S. Guerra, J. Han, O. Y. Gutiérrez, J. A. Lercher, *Catal. Today*, 297, 344.
- Hydrodeoxygenation of fatty acid esters catalyzed by Ni on nano-sized MFI type zeolites
M. W. Schreiber, O. Y. Gutiérrez, J. A. Lercher, *Catal. Sci. Technol.*, 2016, 6, 7976.

6.2 Oral presentations

- Synergetic interaction of Ga species and Brønsted acid sites for propane dehydrogenation in Ga/HMFI catalysts
M. W. Schreiber, M. Baumgärtl, E. Baráth, A. Jentys, J. A. Lercher, 28. Deutsche Zeolith-Tagung, 2016, Gießen, Germany
- Activity trends in Ga/HMFI catalysts for propane dehydrogenation – Synergetic interactions of Ga species and acid sites
M. W. Schreiber, M. Baumgärtl, E. Baráth, A. Jentys, J. A. Lercher, French Conference on Catalysis, 2016, Frejus, France
- Brønsted-Lewis acid pairs in Ga/H-ZSM-5 for light alkane dehydrogenation
M. W. Schreiber, M. Baumgärtl, A. Jentys, R. Bermejo-Deval, J. A. Lercher
25th North American Catalysis Society Meeting (NAM), 2017, Denver, USA
- Brønsted and Ga Lewis acid synergy in ZSM-5 for alkane dehydrogenation
M.W. Schreiber, M. Baumgärtl, A. Jentys, R. Bermejo - Deval, J.A. Lercher
13th Europacat, 2017, Florence, Italy

6.3 Poster presentations

- Nature of active sites in Ga/HMFI catalysts for propane dehydrogenation
M. W. Schreiber, E. Baráth, O. Y. Gutiérrez, J. A. Lercher, 49. Jahrestreffen Deutscher Katalytiker, 2016, Weimar, Germany
- Influence of Brønsted acidity on metal activity for C-O hydrogenolysis in microalgae oil conversion over Ni/HMFI
M. W. Schreiber, E. Baráth, O. Y. Gutiérrez, J. A. Lercher, International Congress on Catalysis, 2016, Peking, China

